Forschungszentrum Karlsruhe
in der Helmholtz-Gemeinschaft

Wissenschaftliche Berichte
FZKA 7092

The Role of Chemistry and Transport on NOy Partitioning and Budget during Austral Spring 2002 as derived from MIPAS Measurements

G. Mengistu Tsidu

Institut f¨ur Meteorologie und Klimaforschung

Februar 2005

Forschungszentrum Karlsruhe

in der Helmholtz-Gemeinschaft

Wissenschaftliche Berichte

FZKA 7092

The Role of Chemistry and Transport on NOy Partitioning and Budget during Austral Spring 2002 as derived from MIPAS measurements

(Die Rolle von Chemie- und Transportprozessen bei der NO_y- Partitionierung und dem NO_y-Budget während des Antarktischen Frühlings 2002, abgeleitet aus MIPAS Messungen)*

Gizaw Mengistu Tsidu

Institut für Meteorologie und Klimaforschung

*Von der Fakultät für Physik der Universität Karlsruhe (TH)
genehmigte Dissertation

Forschungszentrum Karlsruhe GmbH, Karlsruhe

2005

Impressum der Print-Ausgabe:

Als Manuskript gedruckt

Forschungszentrum Karlsruhe GmbH
Postfach 3640, 76021 Karlsruhe

Mitglied der Hermann von Helmholtz-Gemeinschaft
Deutscher Forschungszentren (HGF)

ISSN 0947-8620

urn:nbn:de:0005-070921

The Role of Chemistry and Transport on NOy Partitioning and Budget during Austral Spring 2002 as derived from MIPAS measurements

(Die Rolle von Chemie- und Transportprozessen bei der NO_y-Partitionierung und dem NO_y-Budget während des Antarktischen Frühlings 2002, abgeleitet aus MIPAS Messungen)

Zur Erlangung des akademischen Grades eines

DOKTORS DER NATURWISSENSCHAFTEN

von der Fakultät für Physik der Universität Karlsruhe (TH)

genehmigte

DISSERTATION

von
Gizaw Mengistu Tsidu
aus Assassa Arsi (Ethiopia)

Tag der mündlichen Prüfung: 19 November, 2004
Referent: Prof. Dr. H. Fischer
Korreferent: P. D. Dr. T. von Clarmann

Abstract

In 2002, the first time a split of the Antarctic stratospheric polar vortex was observed. An accurate and well characterized data set of nitrogen species (HNO_3, $ClONO_2$, N_2O_5, NO, NO_2) and long-lived species (N_2O, CH_4, CFC-11), retrieved from limb emission spectra recorded by the Michelson Interferometer for Passive Atmospheric Sounding (MIPAS) aboard the European ENVIronmental SATellite (ENVISAT) is used to study the nitrogen chemistry in this episode. The retrieval algorithm used in this context to derive temperature and composition of the atmosphere from measured limb radiances was tested and cross-checked against the conceptually different Hessian method. A retrieval strategy is proposed to distinguish background continuum emission from continuum-like emission of the N_2O_5 signal. The diagnostics of the retrieved volume mixing ratios (VMR), using N_2O_5 as example of the most difficult components of NO_y to retrieve, are presented. NO_y and two of its components, namely HNO_3 and N_2O_5, are, as part of the validation activities, compared with measurements from other instruments. The N_2O_5 VMRs at high latitudes outside the polar vortex are investigated to assess the impact of the stratospheric major warming during September 2002. Moreover, the retrieved nitrogen species and source gases during the major stratospheric warming, are analysed to study the role of chemistry and dynamics on the stratospheric NO_y partitioning and budget during this event.

For purposes of cross-validation of the routinely used Gauss-Newton algorithm and the improved Hessian method, test retrievals were carried out on the basis of simulated limb emission spectra. These show that both algorithms generally produce nearly identical results and error covariance matrices. Small differences are attributed to the different treatment of nonlinearity in the Hessian approach and differences in the calculation of the derivative of the forward model with respect to VMR. The results of the comparison of the two methods confirm the appropriate level of accuarcy of the more efficient variant of the Gauss-Newton-based algorithm used to retrieve the constituent species.

The retrieval of N_2O_5 is difficult due to the continuum-like emission feature of this species. The N_2O_5 band covers a wide spectral region and is hardly distinguishable from background continuum emission. The method of constraining the background continuum in the spectral region used for N_2O_5 analysis to the value determined in an N_2O_5 free spectral region was found to be appropriate to solve this problem. Retrieved VMRs of N_2O_5 exhibit features consistent with the dynamics prevalent at the time in the Antarctic and known N_2O_5 chemistry governing diurnal variability. The observations of low N_2O_5 inside vortex airmass and N_2O_5 rich ex-vortex airmass are strongly consistent with the chemistry that governs the N_2O_5 fraction within the NO_y family.

The comparison of MIPAS/ENVISAT HNO_3 and N_2O_5 with measurements by MIPAS-B (a MIPAS instrument onboard a stratospheric balloon-platform) indicates good agreement in cases when when the coincidence in space and time of both measurements is very good. The comparison of MIPAS NO_y with measurements from the in-situ SIOUX instrument is affected by the difference in the vertical resolution, scarcity of measurements of good coincidence in space. However, the agreement is improved after degrading SIOUX NO_y vertical profiles by MIPAS averaging kernels. The MIPAS HNO_3 equivalent latitude averages lie within the scatter of the 8-year climatology of HNO_3 measured by the Microwave Limb Sounder (MLS) on Upper Atmospheric Research Satellite (UARS).

The enhanced nighttime high geographic latitude N_2O_5 VMR with a peak of 4.4 ppbv in the alti-

tude range of 32-37 km during the last week of September 2002 is consistent with airmass transport from lower to high latitudes and temperature sensitive N_2O_5 formation chemistry. N_2O_5 enhancement up to 6 ppbv was also observed by the Cryogenic Limb Array Etalon Spectrometer(CLAES) and Improved Stratospheric and Mesospheric Sounder (ISAMS) experiments on UARS during northern hemisphere January 1992 stratospheric warming which was a factor of 3 larger than any measurements of N_2O_5 prior to UARS. In contrast, a maximum of 4.4 ppbv N_2O_5 VMR observed by MIPAS at 32-37 km is only a factor of 2 larger than its prewarming values.

The comparison of [NO_y]:[N_2O] correlation curve determined from MIPAS July data with the correlation curve determined from measurements by the Atmospheric Trace Molecule Spectroscopy Experiment (ATMOS) and that constructed from combined data (ground-based millimeter-wave spectrometer (GBMS) at the South Pole, Halogen Occultation Experiment (HALOE) aboard UARS, Polar Ozone and Aerosol Measurement II instrument (POAM II) aboard French SPOT-3 polar orbiting satellite and model calculations) suggests that the MIPAS July [NO_y]:[N_2O] correlation curve represents the transition period (late winter) in the polar stratosphere, during which the [NO_y]:[N_2O] correlation evolves continuously from the formation of the vortex during the preceeding fall (as described by the correlation constructed from combined data) to its breakup in spring (as described by ATMOS correlation). The evolution of the MIPAS ex-vortex correlation curve from July to the September/October period is also in agreement with preceeding observations. At the linear end of the correlation curve due to high bias in N_2O in September, no conclusion can be drawn on the evolution of the correlation curve.

The chemical and transport processes determining the NO_y deficit and partitioning are investigated. Most of the available NO_y in the polar vortex was in the form of HNO_3 and NO_x in the lower stratosphere except for the period 22 - 27 September when NO_y was dominantly found in the form of HNO_3 and $ClONO_2$ between the 400 K and 475 K levels. The dominant process throughout the lower stratosphere was enhanced photolysis of HNO_3 resulting in a steady increase of NO_x during the split of vortex. The enhanced photolysis was initiated following the displacement of the vortex to low and mid-latitudes. This observation was confirmed by the buildup of HNO_3 after this period in mid-October following the vortex repositioning on the pole. N_2O_5 inside the vortex increased above 625 K level during the 22-27 September period following the enhancement of NO_x from HNO_3 photolysis. On the 475 K level, the NO_y volume mixing ratio (VMR) inside the vortex is lower than the reference value derived from its proxy early winter ex-vortex relation by $\approx$ 12.5 ppbv during the whole period. The artificial reference linear tracer method suggests that the NO_y deficit during the period accounted by descent followed by quasi-horizontal mixing and denitrification is approximately 25% and 75% respectively before the split of vortex and 40-45% and 55-60% respectively after the split of vortex. The quasi-isentropic mixing line approach overestimates mixing induced NO_y deficit due to indications for occurrences of several single mixing events and/or continuous mixing from the [CH_4]:[N_2O] vortex scatter plots and thus provides mixing values of 55-60% and 62% before and after the split of vortex respectively.

Zusammenfassung

Die Rolle von Chemie- und Transportprozessen bei der NO_y-Partitionierung und dem NO_y-Budget während des Antarktischen Frühlings 2002, abgeleitet aus MIPAS Messungen

Im Jahre 2002 wurde erstmals ein Aufspalten des Antarktischen Polarwirbels beobachtet. Zur Untersuchung der Stickstoffchemie während dieser Episode wurde ein genauer und gut charakterisierter Datensatz über Verbindungen aus der Stickstofffamilie (HNO_3, $ClONO_2$, N_2O_5, NO, NO_2) und langlebigen Gasen (N_2O, CH_4, CFC-11) herangezogen. Die Höhenprofile dieser Gase wurden aus Horizontsondierung-Emissionsspektren abgeleitet, die mit dem Michelson Interferometer für Passive Atmosphärische Sondierung (MIPAS) auf dem Europäischen Umweltforschungssatelliten ENVISAT gemessen wurden. Der hierzu verwendete Inversionsalgorithmus wurde anhand der konzeptuell unterschiedlichen Hesse-Methode kreuzvalidiert. Ein Ansatz zur Unterscheidung des spektralen N_2O_5-Signals von der Hintergrundkontinuumsstrahlung wurde entwickelt. Die Charakterisierung der abgeleiteten Höhenprofile wird anhand von N_2O_5, dem am schwierigsten abzuleitenden Gas aus der NO_y-Familie, diskutiert. NO_y und zwei seiner Komponenten, nämlich HNO_3 und N_2O_5 werden im Rahmen von Validierungsaktivitäten mit Messungen von anderen Instrumenten verglichen. Die N_2O_5-Mischungsverhältnisse in hohen Breiten außerhalb des Polarwirbels werden verwendet, um den Einfluss der Stratosphärenerwärmung im September 2002 abzuschätzen. Darüber hinaus wurden die abgeleiteten Höhenprofile der Stickstoffverbindungen und Quellgase verwendet, um die dynamischen und chemischen Prozesse, die die stratosphärische NO_y-Partitionierung und -Budget während dieser Episode regulieren, zu unterscheiden.

Zur Kreuzvalidierung des im Routinebetrieb verwendeten Gauss-Newton-Algorithmus und der verbesserten Hesse-Methode wurden Testrechnungen durchgeführt, bei denen simulierte Messungen invertiert wurden. Diese Testrechnungen liefern für beide Methoden im Allgemeinen beinahe identische Ergebnisse und Fehlerkovarianzmatrizen. Kleine Differenzen werden durch den unterschiedlichen Ansatz bezüglich der Nichtlinearität und verschiedenen Methoden der Approximation der Ableitung des Vorwärtsmodells bezüglich der Mischungsverhältnisse erklärt. Die Ergebnisse dieses Vergleichs bestätigen, dass die Verwendung des effektiveren Algorithmus auf Basis der Gauss-Newton-Methode in Hinblick auf die Genauigkeit der abgeleiteten Spurengasprofile gerechtfertigt ist.

Ein Problem bei der Auswertung von N_2O_5 ist die Unterscheidung seines wenig strukturierten Spektralsignals vom Hintergrundkontinuum. Das Festhalten des Hintergrundsignals bei einem Wert, der in einem Teil des Spektrums ermittelt wird, der kein Spektralsignal von N_2O_5 aufweist, löst dieses Problem hinlänglich. Die abgeleiteten Volumenmischungsverhältnisse von N_2O_5 zeigen die Charakteristik, wie man sie auf Grund der zur Zeit der Wirbelaufspaltung vorherrschenden dynamischen Verhältnisse und des bekannten Tagesgangs erwartet. Die niedrigen N_2O_5-Werte innerhalb der Vortex und N_2O_5-reiche Luftmassen außerhalb der Vortex sind in Einklang mit den chemischen Prozessen, die die NO_y-Fraktionierung bezüglich N_2O_5 bestimmen.

Der Vergleich von MIPAS/ENVISAT HNO_3 und N_2O_5 mit MIPAS-B (ein MIPAS Instrument auf einer Stratosphärenballongondel) Messungen zeigt gute Übereinstimmung in Fällen guter räumlicher und zeitlicher Übereinstimmung der Messungen. Der Vergleich des MIPAS NO_y mit in situ Messungen mit dem SIOUX-Instrument wird durch die unterschiedliche Höhenauflösung

beider Instrumente beeinflußt. Außerdem gab es wenige Messungen mit guter räumlicher Koinzidenz. Eine bessere Übereinstimmung wird jedoch erreicht, wenn man die SIOUX NO_y Vertikalprofile mit der für MIPAS charakteristischen Auflösungsmatrix verschmiert. Die über äquivalente Breiten gemittelten MIPAS HNO_3-Werte liegen im Streubereich der 8-Jahre-Klimatologie auf Basis der Messungen des Microwave Limb Sounder (MLS) auf dem Upper Atmospheric Research Satellite (UARS).

Erhöhte nächtliche N_2O_5-Mischungsverhältnisse in hohen Breiten mit Werten bis 4.4 ppbv im Höhenbereich 32-37 km in der letzten Septemberwoche 2002 sind in Einklang mit Transporten von niedrigen zu hohen Breiten und der Temperaturabhängigkeit der N_2O_5-Bildungsprozesse. Erhöhte Werte bis zu 6 ppbv – drei mal so viel als bis dahin jemals gemessen wurde – wurden auch schon mit dem Cryogenic Limb Array Etalon Spectrometer (CLAES) und dem Improved Stratospheric and Mesospheric Sounder (ISAMS) auf UARS während der nordhemisphärischen Stratosphärenerwärmung im Januar 1992 gemessen. Dagegen sind die von MIPAS im Höhenbereich 32-37 km gemessenen Werte von maximal 4.4 ppbv nur doppelt so groß im Vergleich zu den Mischungsverhältnissen vor der Stratosphärenerwärmung. Der Vergleich von $[NO_y]$:$[N_2O]$ Korrelationskurven aus MIPAS-Daten, die im Juli gemessen wurden, mit entsprechenden Daten vom Atmospheric Trace Molecule Spectroscopy Experiment (ATMOS) und solchen, die durch synergistische Verwendung weiterer Daten konstruiert wurden (dem bodengebundenen Millimeterwellen-Spektrometer (GBMS) am Südpol, dem Halogen Occultation Experiment (HALOE) auf UARS, dem Polar Ozone and Aerosol Measurement II Instrument (POAM II) auf dem französischen polar umlaufenden SPOT-3 Satelliten und Modellrechnungen) deuten darauf hin, dass die $[NO_y]$:$[N_2O]$-Korrelationskurve der im Juli gemessenen MIPAS-Daten eine spätwinterliche Übergangsphase charakterisiert, während der die $[NO_y]$:$[N_2O]$-Korrelation sich kontinuierlich von der Vortexbildungsphase in Richtung Vortexauflösung im Frühling (ATMOS) entwickelt hat. Außerdem stimmt die Entwicklung der Korrelationskurve der Werte, die von Juli bis September außerhalb der Vortex gemessen wurden, mit früheren Messungen überein. Im linearen Bereich der Korrelationskurve kann aufgrund eines systematischen Fehlers in den N_2O-Daten im September keine Schlussfolgerung auf die Entwicklung der Kurve gezogen werden.

Die das NO_y-Defizit und die NO_y-Partitionierung bestimmenden chemischen und Transportprozesse wurden untersucht. Der größte Anteil des im Polarwirbel verfügbaren NO_y lag in der unteren Stratosphäre als HNO_3 und NO_x vor, außer in der Zeit vom 22. bis - 27. September, als im Höhenbereich von 400 bis 475 Kelvin HNO_3 und $ClONO_2$ die Hauptbestandteile waren. Der dominierende Prozess in der gesamten unteren Stratosphäre war verstärkte Photolyse von HNO_3, die zu einer fortlaufenden NO_x-Zunahme während der Wirbelaufspaltung führte. Die verstärkte Photolyse kam durch die Verlagerung des Wirbels in Richtung niedrigeren Breiten zustande. Diese Beobachtung wurde durch die HNO_3-Bildung nach dieser Periode der Wirbelaufspaltung Mitte Oktober bestätigt, als sich der Wirbel wieder über dem Pol zentrierte. Infolge des aus der HNO_3-Photolyse stammenden erhöhten NO_x nahmen die N_2O_5-Mischungsverhältnisse innerhalb des Wirbels oberhalb 625 K vom 22. bis 27. September zu. Auf 475 K war das Volumenmischungsverhältnis von NO_y innerhalb des Wirbels während der gesamten Periode um etwa 12.5 ppbv niedriger als der Referenzwert, der aus der für Luftmassen außerhalb des Wirbels gebildeten Frühwinterkorrelation abgeschätzt wurde. Die Methode des künstlichen linearen Tracers deutet darauf hin, dass das NO_y-Defizit in diesem Zeitraum, das durch Absinken und anschließender quasi-horizontaler Mischung verursacht wurde, etwa 25% vor und 40-45% nach der Wirbelaufspaltung betrug, während Denitrifizierung mit 75 und 55-60% beitrug. Das Verfahren

der quasi-isentropischen Mischungslinie angewendet auf in der Vortex gemessene [CH_4]:[N_2O] Korrelationen überschätzt den durch Mischung verursachten Anteil des NO_y-Defizits aufgrund verschiedener einzelner Mischungsprozesse und/oder kontinuierlicher Mischung. Diese Methode erklärt 55-60% des NO_y-Defizits vor der Wirbelaufspaltung und 62% danach durch Mischungsprozesse.

Contents

1 Introduction **1**

1.1 Stratospheric chemistry 2

1.1.1 Observed ozone changes 2

1.1.2 Chemical Processes 2

1.1.3 Why is understanding of stratospheric NOy important? 4

1.2 Current Understanding of Evolution of Stratospheric NO_y 5

1.3 Motivation 7

2 Principles of Limb Sounding Instruments **9**

2.1 The Measurement Principles 10

2.2 The MIPAS Instrument 11

2.3 Forward radiative transfer model 11

2.4 The Inverse Model 13

2.4.1 The Retrieval Procedures 13

2.4.2 Error Estimation 14

3 Gauss-Newton method versus the Improved Hessian Method **15**

3.1 Inverse Model Description 15

3.2 Calculation of Hessian 16

3.2.1 Discrete calculation of the Hessian 16

3.2.2 Adaptive algorithm for calculation of Hessian 17

3.3 Application to Atmospheric Spectroscopy 19
3.3.1 Comparison method 19
3.3.2 Results and Discussion 21

4 Retrieval of N_2O_5, an important component of NO_y 31

4.1 Retrieval of N_2O_5 31
4.1.1 General Retrieval Sequence and Specific Strategy for Retrieval of N_2O_5 . 31
4.1.2 Elements of the state vector and regularization in N_2O_5 retrieval 32
4.2 Results and Diagnostics 35

5 Validation of MIPAS/ENVISAT NO_y, HNO_3 and N_2O_5 39

5.1 Brief Description of Instruments 39
5.1.1 MIPAS-B2 FTIR Spectrometer 39
5.1.2 MkIV Interferometer 39
5.1.3 SIOUX in situ chemical instrument 40
5.1.4 Microwave Limb Sounder (MLS) on UARS 40
5.2 Comparison 40
5.2.1 Comparison With MIPAS-B2 41
5.2.2 Comparison With MkIV 42
5.2.3 Comparison With SIOUX 43
5.2.4 Comparison of MIPAS HNO_3 with MLS HNO_3 climatology 44

6 NOy in the Austral Spring 2002 47

6.1 Data 47
6.1.1 MIPAS NO_y and Long-lived Species 47
6.1.2 Potential Vorticity and related Quantity derived from Meteorological Data 48
6.1.3 Error Estimation for NO_y 51
6.2 Vortex as observed from evolution of NO_y and N_2O 52
6.3 Stratospheric N_2O_5: Application to the major warming event 54

6.4 NO_y Budget and Partitioning 60

6.4.1 Inside-vortex region 61

6.4.2 Vortex edge and ex-vortex regions 65

6.5 Denitrification and mixing effects in NO_y deficit 65

7 Conclusion **73**

References **76**

Chapter 1

Introduction

The principles of remote sensing are used for a wide variety of purposes, from examining the structure of the nucleus of an atom to the structure of stars, from oil exploration to medical tomography. The early development of remote sensing as a scientific field is closely tied to developments in photography. The first photographs were reportedly taken by Daguerre and Niepce in 1839.

A number of progress have been made in the development of remote sensing since then. Beginning in the mid-1960's, a large number of studies of the application of color infrared and multispectral photography were undertaken under the sponsorship of NASA, leading to the launch of multispectral imagers on the Landsat satellites in the 1970's which were initiated due to two principal events. The first of these, during and after world war II, was the concerted military development of sensitive, fast-response detectors and compatible optical materials and later computers. The second, during late 1960's and early 1970's, was the emerging perception that manufactured chemicals in the atmosphere could affect the long-term stability of stratospheric ozone layer and the overall radiation balance of the planet. The concerns generated by this realization lead to development of instrumentation capable of first detecting, and then monitoring on a global scale, the concentrations of numerous source, sink, reactive and reservoir molecular species involved in these potential changes.

To this end, IR spectroscopy is of very great importance because the atmosphere absorbs and radiates strongly in this spectral region. While there are several measurement techniques for the IR spectroscopy, Fourier Transform Infrared Spectroscopy (FTIR) using Michelson Interformeter is the most suitable for measuring most trace gases in the atmosphere simultaneously. As a result, there are several ground networks that monitor the atmosphere on nearly regular basis using FTIR spectroscopy. In addition, there have been several Balloon and Aircraft borne FTIR measurement campaigns in the past with different scientific objectives. However, these are limited in its temporal or spatial coverage which in turn limit the scope of the scientific study conducted using such measurements. Thus, atmospheric structures with short time and small spatial scales can only be captured by near continuous monitoring which can be realized from space-borne measurements. In the mid 1980's the Atmospheric Trace Molecular Spectroscopy (ATMOS) instrument which use FTIR measurement techniques flew on space schuttle and made solar occulation measurements. The solar occulation measurement, despite its high vertical resolution and good accuracy, has a poor spatial coverage fewer than 15 sunrise and sunset profiles in a given latitude band. Michelson

Interferometer for passive atmospheric sounding (MIPAS) on Environmental Satellite (ENVISAT) [*Fischer and Oelhaf*, 1996; *Endemann and Fischer*, 1993; *European Space Agency*, 2000] is designed to overcome some of these limitations. The scientific objective of MIPAS/ENVISAT is primarily the understanding of stratospheric chemistry. Understanding of budget and partitioning of nitrogen reservior (NO_y) into its component species and its role in ozone chemistry are one of the key scientific issues to be addressed based on MIPAS measurements.

1.1 Stratospheric chemistry

1.1.1 Observed ozone changes

Ozone is one of the most important trace species in the atmosphere. It removes most of the biologically harmful ultraviolet light before the light reaches the surface, and it plays an essential role in setting up the temperature structure and therefore the radiative heating/cooling balance in the stratosphere. The observed seasonal changes in amount of ozone in the south polar region is different from that which had been observed in the north. The seasonal ozone changes are basically determined by stratospheric circulation. Interseasonal variability in ozone abundance is linked to the 11-year solar cycle in UV output and the amount of aerosols in the stratosphere.

In the Arctic, for example, the total ozone amount grew rapidly in the late winter and early spring to about 500 DU. In contrast, the Antarctic early springtime amounts remained near 300 DU. *Farman et al.* [1985] showed that the springtime ozone amounts over Halley Bay had declined from about 300 DU in the early 1960s to about 180 DU in shortly before and mid 1980s. These large ozone changes implied that losses must be taking place in the lower stratosphere. The 1996-97 Northern Hemisphere winter experienced a significant ozone depletion over the Arctic and subsequent ozone values achieved record low values in the spring. Chlorine radicals have been identified as the causes of ozone depletion now in both hemispheres. Changes in the profile of ozone with altitude was observed between tropopause and 24 km altitude in midlatitude. Negative ozone trend in the lower stratosphere is also indicated for the tropics.

1.1.2 Chemical Processes

The amount of ozone in the global stratosphere is determined by the magnitude of the production and loss processes and by the rate at which air is transported from the region of net production to those of net loss.

Production of ozone requires the breaking of an O_2 bond, which then attaches to another O_2 to form O_3. This happens mostly by photodissociation of O_2 by solar UV radiation. In the troposphere and lower stratosphere ozone is produced by photochemical smog-like reactions in which H or CH_3 or higher hydrocarbon radicals attach to an O_2 forming HO_2 or CH_3O_2 which then react with NO. This reaction breaks the O_2 bond by forming NO_2 which photolyzes to form O that reacts with O_2. The loss of ozone occurs when O atom reacts with O_3 to reform the O_2 molecule. This loss process is catalyzed by the oxides of hydrogen, nitrogen, chlorine and bromine chemical cycles shown in Fig. 1.1.

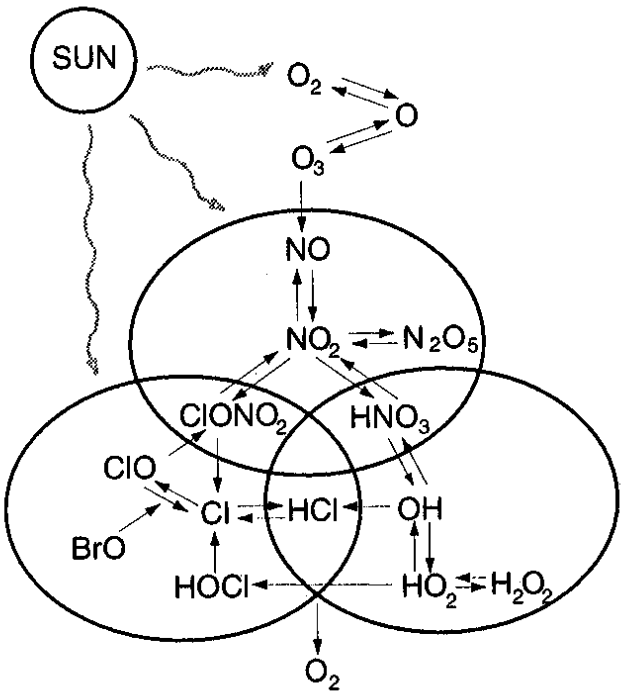

Figure 1.1: A simple scheme of the most gas phase reactions for the stratospheric chemistry. The ellipses include the nitrogen, chlorine and hydrogen families (taken from *Visconti* [2001]).

The sources of these radicals are source gases in the troposphere. Chlorine radicals are produced from the photodissociation of chlorofluorocarbons (CFC) but also from natural compounds. Nitrogen oxides are emitted directly in the atmosphere from combustion processes (in the upper troposphere by aircraft) or may be produced by oxide decomposition. The production of hydrogen radical is due mainly to the decomposition of water vapor through dissociative reaction with metastable oxygen (^1O). The sources of bromine are methyl bromide (CH_3Br) and the halons (CF_3Br and CH_2ClBr).

The catalytic efficiency of hydrogen, nitrogen, chlorine and bromine oxides is determined by a set of interlocking reactions which convert the active oxides to catalytically inactive temporary reservoirs, such as HNO_3, HCl, $ClONO_2$, H_2O, HOCl, HOBr, and $BrONO_2$ and vice versa. Part of this interlocking reactions is shown in Fig. 1.1, a simple scheme of the most important gas phase reaction. The photodissociation is the main mechanism through which the radicals are released from the reserviour species (HCl, N_2O_5, $ClONO_2$, HNO_3, HOCl).

In the lower stratosphere, the balance between catalytic oxides and reservoir is strongly affected by reactions on the surfaces of stratospheric aerosols. It is even more profoundly affected in the polar winter by reactions on PSC particles.

1.1.3 Why is understanding of stratospheric NOy important?

Understanding the mechanisms controlling the abundance of NO_y and its partitioning into component species is critical for understanding the chemistry of the ozone layer. The abundance of ozone in the stratosphere is controlled by odd hydrogen, odd nitrogen, and bromine and chlorine catalytic cycles and heterogeneous chemistry.

NO_y species are involved in the odd nitrogen catalytic cycle and heterogeneous chemistry (e.g *Brasseur and Solomon* [1986]; *Visconti* [2001]; *Jacobson* [1999] and references therein). Specifically, NO_x (NO_x=NO+NO_2) catalytically destroys ozone via reactions:

$$NO + O_3 \rightarrow NO_2 + O_2 \tag{1.1}$$

and

$$NO_2 + O \rightarrow NO + O_2. \tag{1.2}$$

The cycle is catalytic since NO_x is conserved (a simple interchange of NO and NO_2). (1.1) and (1.2) also represent catalytic ozone loss cycle by reactive hydrogen (HO_x), chlorine (ClO_x) and bromine (BrO_x) species if NO is replaced with OH, Cl, or Br respectively.

NO_x buffers the ozone loss by HO_x, ClO_x, and BrO_x by converting OH, ClO, and BrO into HNO_3, $ClONO_2$, and $BrONO_2$ which do not directly destroy ozone (and hence are called reservior NO_y species), via the following reactions:

$$NO_2 + OH + M \rightarrow HNO_3 + M \tag{1.3}$$
$$NO_2 + ClO + M \rightarrow ClONO_2 + M \tag{1.4}$$
$$NO_2 + BrO + M \rightarrow BrONO_2 + M. \tag{1.5}$$

The third body M represents the major atmospheric molecules N_2 and O_2. The relative importance of catalytic loss cycles by HO_x, ClO_x, and BrO_x is strongly dependent upon the NO_x abundance. NO_x buffers HO_x and ClO_x catalytic cycles also by the following interchange reactions:

$$NO + HO_2 \rightarrow NO_2 + OH \tag{1.6}$$
$$NO + ClO \rightarrow NO_2 + Cl \tag{1.7}$$

by decreasing the levels of HO_2 and ClO respectively. On the other hand, these reactions increase the NO_2/NO ratio, enhancing the ozone loss rate by the NO_x cycles (since reaction (1.2) is rate determing and hence the loss rate is proportional to [NO_2][O]).

The reactions that control N_2O_5 in the NO_y partitioning are

$$NO_2 + O_3 \rightarrow NO_3 + O_2 \tag{1.8}$$

$$NO_2 + NO_3 + M \rightarrow N_2O_5 + M \tag{1.9}$$

at night and collisional decomposition or photolysis in sunlight via

$$N_2O_5 + M \rightarrow NO_3 + NO_2 \tag{1.10}$$

$$N_2O_5 + h\nu \rightarrow NO_3 + NO_2 \tag{1.11}$$

at daytime. Therefore, the N_2O_5 concentration shows pronounced diurnal variations and reaches its maximum before sunrise and its minimum shortly after sunset. N_2O_5 is also lost due to heterogeneous reaction in the presence of aerosols via

$$N_2O_5(\text{gas}) + H_2O(\text{aerosol}) \rightarrow 2HNO_3(\text{gas}). \tag{1.12}$$

As a result N_2O_5 controls the level of NO_x directly through reactions (1.8-1.11) and indirectly through reaction (1.12). HNO_3 and $ClONO_2$ produce NO_x by photolysis and reactions with OH:

$$\begin{aligned} HNO_3 + OH &\rightarrow NO_3 + H_2O & (1.13)\\ HNO_3 + h\nu &\rightarrow OH + NO_2 & (1.14)\\ ClONO_2 + h\nu &\rightarrow Cl + NO_3 & (1.15)\\ ClONO_2 + h\nu &\rightarrow ClO + NO_2. & (1.16) \end{aligned}$$

Heterogeneous chemistry in which chemical reactions may happen between different phases, like gas and liquids or solids also affect ozone abundance. Some of the reactions develop on the surface of sulfate particles, a thin aerosol layer present in the lower stratosphere. The dynamic isolation of the polar region determines the low temperatures in the winter stratosphere that cause the condensation of nitric acid or even water vapor, which leads to the formation of polar stratospheric clouds (PSC). These clouds have fundamental role in the ozone destruction in the polar region.

1.2 Current Understanding of Evolution of Stratospheric NO_y

The volume mixing ratios of stratospheric trace species evolves according to continuity equation:

$$\begin{aligned} \frac{\partial q_i}{\partial t}(r,t) + \mathbf{v}\cdot\nabla\mathbf{q_i}(\mathbf{r},\mathbf{t}) &= C_i(r,t,q_1(r,t),...,q_i(r,t),...,q_n(r,t)) \\ &\quad + D_i(r,t,q_1(r,t),...,q_i(r,t),...,q_n(r,t)), \end{aligned} \tag{1.17}$$

where q is volume mixing ratio given by $q = \frac{\rho_i}{\rho}$ and, ρ_i is the number density or concentration of species i and ρ is the number density of air. C_i accounts for chemical sources and sinks for species i, and D_i accounts for second order diffusive contribution which may include mixing processes, Fickian diffusivity, or even breaking waves (*Jacobson* [1999] and references therein).

It is natural to assume that the potential relation between two (or possibly more) mixing ratios of two simultaneously transported reactive species will result from a combination of chemical and diffusive effects. Correlation equations thus formed involving volume mixing ratios of some long-lived species, referred to as tracer:tracer relations, are often used to distinugish contributions of transport from chemistry to the evolution of the tracers in the atmosphere without employing the full chemistry-transport models. We use such relations extensively later to make distinction between denitrification-induced (complete removal of nitrogen species after condensation in PSCs by sedimentation) NO_y deficit in the polar vortex from that induced by mixing with outside airmasses.

The changes in mid-stratospheric ozone abundance are largely controlled by the abundances of NO_x ($[NO_x]=[NO]+[NO_2]$) and NO_y ($[NO_y]=[HNO_3]+[ClONO_2]+[NO_x]+2[N_2O_5]$) and their partitioning (see Fig. 1.1 for an overview and reactions (1.1) to (1.16) for more details of the individual

reaction pathways). Nitric acid (HNO_3), which is a main reservoir for the reactive nitrogen oxides in the lower stratosphere for example, is important in the photochemistry of these regions of the atmosphere. HNO_3 is photochemically linked to NO_x (see reaction (1.14)) which is directly involved in processes that control ozone abundance. Moreover, inside the polar vortex during midwinter condensation of HNO_3 in PSC and subsequent permanent removal through sedimentation delays chlorine deactivation (via reaction (1.4)) and allows longer period for ozone destruction by ClO. Therefore, the modeling of the NO_y budget and its partitioning requires accurate characterization of the chemical and transport processes. In the past, several works have been done which contributed towards better understanding and improvement in accuracy of measurements of the NO_y components, and better characterization of the chemical and transport processes affecting NO_y budget and its partitioning.

N_2O_5 is one of the dominant nighttime reserviors for the active nitrogen species in the stratosphere. The catalytic destruction of ozone by NO and NO_2 is reduced by the formation of N_2O_5 (via reaction (1.9)). Therefore, it is a crucial part of the ozone chemical cycle in the stratosphere. However, knowlege on its variability and distribution is incomplete due to difficulty and scarcity of its measurements. As a result, dynamical-chemical models of the stratosphere were not adquately tested. The first N_2O_5 measurement was conducted by *King et al.* [1976] who deduced its existence in the stratosphere from solar absorption spectra. *Roscoe* [1982] identified N_2O_5 by measuring day-night difference in thermal emission near 1240 cm^{-1} compared to that at 1320 cm^{-1} from a balloon-borne limb scanning radiometer. This measurement was later confirmed by ATMOS experiment on Spacelab 3 [*Toon et al.*, 1986; *Toon*, 1987]. *Roscoe* [1991] has given the overview of available data and the difficulties of intercomparison due to the differences in measurement times and assumed spectroscopic parameters. Various earlier laboratory measurements of N_2O_5 cross-sections and its temperature dependence differed substantially. However, quite good agreement between later measurements, e.g. by *Cantrell et al.* [1988] and *Newnham et al.* [1993], suggest that current N_2O_5 cross-section data are rather consistent and do not show dependence on temperature between 233 K to 293 K.

The large uncertainities in the absolute strengths of all bands of HNO_3 is a dominant contributor to the uncertainity in HNO_3 VMR [*Goldman et. al*, 1998; *Perrin et al.*, 1998]. It has been reported that this large uncertainity in absolute band strengths contribute to most of the difference in HNO_3 VMR derived from different bands (e.g. *Jucks et al.* [1999] and references therein). Current progress in measurements of NO_2 and NO by spectroscopic remote sensing of the atmosphere are summarized (e.g. in *Funke et. al* [2004] and references therein).

The air inside the Antarctic polar vortex is fairly isolated during midwinter, but mixing with midlatitude air occurs as the vortex begins weakening until its breakup. The vortex erosion and the accompanying mixing of air inside and outside the vortex is extensively discussed in *Russell III et al.* [1993]; *Gao et al.* [1999]; *Chen et. al* [1994]; *Manney et al.* [1994]; *Tao and Tuck* [1994]; *Rosenlof et. al* [1997]; and *Bühler and Haynes* [1999].

The fact that some long-lived tracers in the stratosphere tend to exhibit compact, robust relationships have been used by several authors for the study of Arctic and Antarctic polar vortices (e.g. *Fahey et al.* [1990]; *Rinsland et al.* [1999]). The observed change in the relationship is attributed to chemical processes. However, it has been recognised that tracer relationship can also be altered due to mixing processes [*Michelsen et al.*, 1998; *Kondo et al.*, 1999].

An extensive study to distinguish between contributions of mixing and chemistry to the altered [NO_y]:[N_2O] relationship was made by *Rex et al.* [1999]. The amount of mixing is estimated from the observed deviation from the standard midlatitude relationship of [CH_4]:[N_2O] which is not affected by denitrification. A number of studies have been accomplished using this method e.g. recently by *Wetzel et al.* [2002] for quantifications of denitrification of NO_y inside the Arctic vortex and quasi-horizontal mixing of airmasses across the vortex edge. The method, however, is valid under conditions in which mixing lines in tracer:tracer relations are assembled over single or fairly narrow range of potential temperatures from points in the profiles. Data points in tracer:tracer plots of profiles over wide range of potential temperatures can easily form a straight line if there is continuous mixing into the polar vortex coupled with airmass descent. Recently, *Esler and Waugh* [2002] proposed constructing artificial 'reference tracer' to distinguish mixing-induced changes in a sufficiently general way. The basis of the artificial reference tracer is that if a tracer happened to have a linear canonical relationship with NO_y (i.e. [$\hat{NO}_y$] $\approx$ [x], where x is artificial reference tracer constructed from linear combination of tracers such as N_2O, CH_4 and CFC-11) at the beginning of the winter, then mixing can only move parcels along it in tracer space. The estimated $\hat{NO}_y$ can therefore be directly read from the canonical relationship, and denitrification is then determined by [$\hat{NO}_y$]-[NO_y].

1.3 Motivation

While there are still discrepancies in our understanding of stratospheric chemistry and transport processes related to NO_y and subsequent impacts on ozone chemistry in the polar vortex, particularily on the gap between model predictions and measurements with respect to the ratio of [NO_x/NO_y], the dynamics that lead to formation of the polar vortex and the wave activities that lead to its breakup are supposedly well understood. The Southern Hemisphere (Antarctic) polar vortex which forms in late autumn is different from the Northern Hemisphere (Arctic) polar vortex in its stability. This is due to the vigorous nature of the wave activity in the northern hemisphere which leads to a number of minor warmings of the polar vortex so that the vortex may break a few times and eventual exchange of air between polar and midlatitude regions can take place. In contrast, the southern hemisphere is well isolated until late spring. However, unusual major warming of southern hemisphere polar vortex in austral spring 2002 occurred following a number of stratospheric minor warmings in August and early September. This led to the split of the polar vortex, an event that has never before been observed in the Southern Hemisphere (SH). It has been proposed that a plausible cause for this event was the prevalence of very strong planetary waves, which led to the warming following the wave energy deposition in the stratosphere (*Varotsos* [2004] and references therein).

It is therefore of great interest to examine the impact of the sudden major warming of SH polar vortex on the NO_y constituent species which control the ozone abundances directly through odd nitrogen catalytic cycles and indirectly through the remaining catalytic cycles as mentioned in the previous sections. In this thesis, the NO_y budget, the partitioning among its constituents and the role of transport and chemistry on the NO_y budget and partitioning are investigated for this event using VMRs of NO_y and long-lived species N_2O, CH_4 and CFC-11 derived from limb radiance measurements made by MIPAS. Prior to the use of the data for the study, the accuarcy and consistency of retrieval algorithm used to produce the data are investigated by comparing with

conceptually different retrieval method in Chapter 3. This is an additional algorithm validation since it has already been intercompared with several others [*von Clarmann et al.*, 2003a]. Following algorithm testing, the diagnostics of the retrieved VMR from the limb radiance measurements is performed in Chapter 4. Since MIPAS on ENVISAT is a new instrument, its data products in the earlier step have to be compared with measurements from existing accurate instruments in Chapter 5 before the scientific exploitation of the data. Finally, the impact of the unusual major warming is examined whether it led to atypical NO_y budget and partitioning among its constituents in Chapter 6.

Chapter 2

Principles of Limb Sounding Instruments

Infrared limb sounding instruments obtain measurements of atmospheric variables by observing thermal emission at infrared wavelengths as the instrument field of view (FOV) is scanned across the atmosphere tangentially.

The signal detected by the sensor on the satellite contains implicit information of atmospheric variables. The extraction of the varibles is possible first by simulating the signal and down grading by the instrument function. This part requires the radiative transfer model which simulates the measurement based on initially guessed state parameters. The similated signal is compared with measurement and an update of the initial state parameters is performed and supplied to the forward model for improved estimate of the measured signal. This interface requires inverse modeling. In this chapter, we give an overview of measurement principle, MIPAS instrument, forward radiative transfer and inverse models.

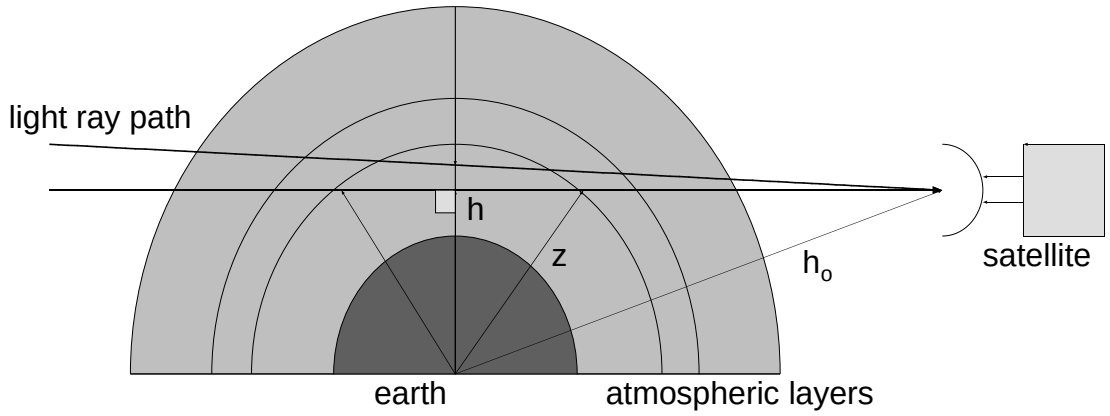

Figure 2.1: Limb viewing geometry.

2.1 The Measurement Principles

For a better understanding of remote sounding, certain basic concepts of electromagenetic (EM) theory is discussed. An EM wave propagating (say along z-axis) consists of two perpendicular fields, the electric and magnetic whose amplitudes oscillate periodically (characterized by speed of light c, wave length λ and frequency f satisfying relation: $f = c/\lambda$) in the xy-plane:

$$\begin{aligned} E_x &= E_{0x}\, cos(wt - kz - \phi_x) \\ E_y &= E_{0y}\, cos(wt - kz - \phi_y) \\ B_x &= \frac{B_{0x}}{c}\, cos(wt - kz - \phi_x) \\ B_y &= \frac{B_{0y}}{c}\, cos(wt - kz - \phi_y), \end{aligned} \tag{2.1}$$

where w is the angular velocity ($2\pi f$, k is the wavenumber ($\frac{2\pi}{\lambda}$), and E_0 is the amplitude of the electric field. Most natural occurring EM radiation is incoherent or randomly polarized, meaning that the phases $\phi_x - \phi_y$ are random. Scattered or artificially produced radiation may be completely or partly polarized i.e. $\phi_x - \phi_y$ is a constant. Different quantities of the EM radiation may be used for different remote sensing applications (e.g. amplitude, frequency for radiometers, spectrometer; phase for Interferometer).

The central component of the MIPAS experiment is a Michelson interferometer. Therefore it is a phase-based remote sensing application of EM radiation. In such instruments amplitude division is usually performed through the use of a partially reflecting/transmitting surface called a beam-splitter. This generates two in-phase wave trains travelling in different directions. A phase shift is introduced into one or both beams, and the two are recombined at another (or the same) partially reflecting surface.

Single atoms or molecules can only emit and absorb photons with energy corresponding to certain transitions between discrete internal energy levels. Transitions between different rotational states have the lowest energy corresponding to wavelengths in the microwave and far-infrared regions. Vibrational transitions correspond to wavelengths in the infrared regions. Vibrational transitions can also involve rotational transitions. Transitions between electronic states are highly energetic with wavelengths in the near-infrared, visible and UV. Electronic transitions can also involve vibration and rotational transitions. In a scattering process, the incoming photon is absorbed to a virtual level and re-emitted in some directions. The size of the particle/molecule and the wavelength of the radiation determines the scattering attenuation and the probability distribution of the directions of the scattered light, i.e. the phase function. The so-called Mie scattering theory is applied for particles/molecules of the same size as the wavelength of the scattered light, e.g. atmospheric aerosols. The Mie phase function is more complicated than Rayleigh phase function (which is applicable to e.g. scattering particles much smaller than the wavelength of the radiation) since it varies with the shape, chemical composition, polarization of the incoming radiation, size and concentration of the particles. Modelling of measured radiation subjected to the above processes require application of forward radiative transfer theory.

2.2 The MIPAS Instrument

MIPAS [*Fischer and Oelhaf*, 1996] is part of the core payload of the ENVISAT environmental research satellite of the European Space Agency (ESA). ENVISAT has been launched into its polar sun-synchronous orbit on 1 March 2002. MIPAS measures mid-IR limb radiation emitted by the atmosphere with a spectral resolution of 0.035 cm^{-1} (unapodized). The field of view is 30 km in the horizontal and 3 km in the vertical at the tangent points. ENVISAT is a sun-synchronous polar-orbiting satellite at an altitude of 800 km with 98.55^o inclination, having an orbital period of about 100 minutes. As a result, MIPAS observes the atmosphere with 14.3 orbits and 73 limb scans per day. The observation time is 10:00 local time at the descending equatorial overpath and 22:30 local time at the ascending equatorial overpath.

The spectral range of MIPAS is divided in five spectral bands: band A(685-970 cm^{-1}), band AB(1020-1170 cm^{-1}), band B(1215-1500 cm^{-1}), band C(1570-1750 cm^{-1}), and band D(1820-2410 cm^{-1}). The noise equivalent spectral radiance (NESR) decreases with increasing wavenumber.

The instrument is designed to allow the simultaneous measurement of several trace gases including the nearly complete NO_y family and temperature. Aerosol particle distribution, tropospheric cirrus clouds and polar stratospheric clouds are additional atmospheric parameters that can be derived from MIPAS observations.

The measurements are obtained with complete global coverage, all seasons, and under both day and night conditions, allowing indirect monitoring of diurnal variations of species such as N_2O_5. The instrument performs measurements in either of two pointing regimes, rearward within a 35^o wide viewing range in the anti-flight direction and sideways within a 30^o wide range on the anti-sun side. The measurements used for the current data set were obtained using the rearward viewing range, since it provides good Earth coverage including the polar regions. A complete description of the instrument concept is given by *Fischer and Oelhaf* [1996]; *Endemann and Fischer* [1993] and *European Space Agency* [2000].

2.3 Forward radiative transfer model

The forward radiative transfer equation to calculate the spectral radiances for viewing angle θ is

$$S_\theta(\nu, l_{obs}) = S_\theta(\nu, \infty)\tau(\nu, l_{obs}, \infty) + \int_{l_{obs}}^{\infty} J(\nu, l)\sigma_{a,tot}^{Vol}(\nu, l)\tau(\nu, l_{obs}, l)dl, \tag{2.2}$$

where J is source function, τ is transmission between observer position l_{obs} and l at wavenumber ν. dl is differential path element, σ is absorption coefficient including gases and aerosols, and $S_\theta(\nu, \infty)$ is background radiances.

The radiative transfer (2.2) is integrated along the line of sight of the instrument traced according to law of refraction of light in atmospheric media. The atmosphere is divided into thin layers each of which is characterized by constant representative state parameters. The angular deviation in the ray path $d\theta$ from its initial direction after traveling an infinitesimal distance dl through atmospheric

medium of refractive index n(l) is determined as

$$d\theta = dl \times \frac{e_s \cdot \nabla n}{n}$$

where e_s is a unit vector in the direction perpendicular to the initial direction. The refractive index n is calculated from the wavenumber dependent refractive index for dry air n_o at reference temperature and pressure $T_o = 288.16$ K and $p_o = 1013.25$ hpa as

$$n(l) = \sqrt{\frac{2kp(l) + T(l)}{T(l) - kp(l)}},$$

where $k = \frac{T_o(n_o^2-1)}{p_o(n_o^2+2)}$.

The dry air refractive index depends on wavenumber according to

$$(n_o - 1)10^{-6} = 83.4213 + \frac{24060.3}{130 - 10^8\nu^2} + \frac{159.97}{38.9 - 10^8\nu^2}$$

where ν is in cm^{-1}. The constant representative state parameters for a thin atmospheric layer j are given by

$$p_{ave.,g,j} = \frac{1}{m_{g,j}} \int p(l)\rho_g(l)dl$$

and

$$T_{ave.,g,j} = \frac{1}{m_{g,j}} \int T(l)\rho_g(l)dl,$$

where the path segment l, the slant path column amount and particle density of species g in layer j are calculated from $l_j = \int dl$, $m_{g,j} = \int_{l_1}^{l_2} \rho_g(l)dl$, and $\rho_g(l) = C_{V,g}\frac{N_{avo}}{R}\frac{p(l)}{T_{kin}(l)}$ respectively. N_{avo}, R, $C_{V,g}$ are Avogadro number, universal gas constant and volume mixing ratio of gas g while $T_{kin}(l)$ is kinetic temperature and p is presure at the position l.

The source function in (2.2) is the Planck function under local thermodynamic equilibrium (LTE). Its non-LTE version includes the ratio of populations r1 and r2 between the non-LTE and LTE for lower and upper states of transition respectively:

$$J^{NLTE}(\nu, l) = \frac{2hc^2\nu^3}{\frac{r1}{r2}exp(\frac{hc\nu}{k_B T_{kin}(l)} - 1)}.$$

This can be simplified to scaled form of Planck function (see *Stiller* [2000] for details).

The spectral atmospheric transmittance $\tau(\nu, l_1, l_2)$ between two points l_1 and l_2 along the line of sight is given by

$$\tau(\nu, l_1, l_2) = exp - [\int_{l_1}^{l_2} \sigma_{a,gas}^{Vol}(\nu, l)dl + \int_{l_1}^{l_2} \sigma_{e,aerosol}^{Vol}(\nu, l)dl]$$

where $\sigma_{e,aerosol}^{Vol}$ and $\sigma_{a,gas}^{Vol}$ are aerosol extinction coefficient calculated using Mie scattering theory and volume absorption coefficients of gases. The aerosol extinction coefficients include scattering as well while gas absorption coefficients include absorption coefficients due to molecular excitation, cross-section and gas continua. The absorption coefficients due to molecular transition can

be calculated under LTE and non-LTE conditions. We refer the reader to the original material (*López-Puertas and Taylor* [2001]; *Stiller* [2000] and references therein) for additional details on the calculation procedure and description of related quantities such as calculation of line intensities and different characterizations of line shape including line mixing.

The comparison of theoretical spectral radiances with measured ones is possible after convolution of the theoretical radiances with field of view (FOV) of the instrument as

$$S_{\theta_o}^{FOV}(\nu, l_{obs}) = \int_{-\theta_{max}}^{\theta_{max}} S_\theta(\nu, l_{obs}) W(\theta - \theta_o) d\theta$$

where $W(\theta - \theta_o)$ is the weighting function related to FOV and θ_{max} maximum angle covered by FOV. This has to be further convolved with the instrumental line shape to make accurate comparison of measurement and simulation.

2.4 The Inverse Model

2.4.1 The Retrieval Procedures

Remote sensing of the atmosphere is an indirect method. The instrument receives a spectrally resolved or integrated radiance signal which is described as

$$\mathbf{y} = \mathbf{F}(\mathbf{x}) + \varepsilon_y, \tag{2.3}$$

where $\mathbf{x}$ is the state vector related to the signal $\mathbf{y}$ through a forward radiative transfer model $\mathbf{F}$, and ε_y is the measurement error. The physics of the problem typically is such that (2.3) is not directly invertible to map the measurement vector $\mathbf{y}$ onto state vector $\mathbf{x}$. Instead, (2.3) is discretized leading to overdetermined state parameters in the case of more measurements than unknowns. However, the inverse problem is often ill-posed. Thus, the retrieval is formulated in the context of estimation theory and allows for the inclusion of a priori information.

The retrieval of atmospheric state vector is based on the standard optimal estimation approach (e.g.*Rodgers* [1976, 2000]). The state vector is typically vertical profiles of temperature, composition and instrumental parameters such as offset, ILS, gain, frquency shift and line of sight (LOS). The limb emission radiances are represented by vector $\mathbf{y}$. The retrieval algorithm selects values for state vector $\mathbf{x}$ at the i^{th} iteration which minimizes the quantity χ^2, defined by

$$\chi^2 = (\mathbf{y} - \mathbf{F}(x_i))^T \mathbf{S}_y^{-1} (\mathbf{y} - \mathbf{F}(x_i)), \tag{2.4}$$

where $\mathbf{S}_y$ is the error covariance matrix of the spectral radiance measurement vector $\mathbf{y}$ and $\mathbf{F}$ is the corresponding forward model. The Gauss-Newton solution to this minimzation is:

$$\mathbf{x}_{i+1} = \mathbf{x}_i + (\mathbf{K}_i^T \mathbf{S}_y^{-1} \mathbf{K}_i)^{-1} \mathbf{K}_i^T \mathbf{S}_y^{-1} [\mathbf{y} - \mathbf{F}(x_i)], \tag{2.5}$$

where $\mathbf{K}_i$ is the matrix of weighting functions or Jacobians.

Very often, the matrix to be inverted in (2.5) is singular. This indicates that there are aspects of the state vector about which the measurement has been unable to provide any information. This singularity can be avoided by including a constraining second term in (2.4):

$$\chi^2 = (\mathbf{y} - \mathbf{F}(\mathbf{x_i}))^{\mathbf{T}} \mathbf{S_y^{-1}} (\mathbf{y} - \mathbf{F}(\mathbf{x_i})) + (\mathbf{x_i} - \mathbf{x_a})^{\mathbf{T}} \mathbf{R} (\mathbf{x_i} - \mathbf{x_a}), \tag{2.6}$$

where $\mathbf{R}$ is the regularization matrix and $\mathbf{x}_a$ is the a priori profile.

The iterative solution now takes the form:

$$\hat{\mathbf{x}}_{i+1} = \hat{\mathbf{x}}_i + (\mathbf{K}_i^T \mathbf{S}_y^{-1} \mathbf{K}_i + \mathbf{R} + \lambda \mathbf{I})^{-1} (\mathbf{K}_i^T \mathbf{S}_y^{-1} [\mathbf{y} - \mathbf{F}(\hat{\mathbf{x}}_i)] - \mathbf{R}(\hat{\mathbf{x}}_i - \mathbf{x}_a)), \tag{2.7}$$

where $\lambda \mathbf{I}$ is a damping term according to *Levenberg* [1944] and *Marquardt* [1963] in order to achieve better convergence.

The matrix of averaging kernel $\mathbf{A}$ which is useful diagnostic tool for characterization of the retrieval is given by

$$\mathbf{A} = \frac{\partial \hat{\mathbf{x}}}{\partial \mathbf{x}_t} = \mathbf{GK}$$

and $\mathbf{G}$ is the gain matrix defined by

$$\mathbf{G} = \mathbf{S_x K^T S_y^{-1}},$$

where $\mathbf{x}_t$ is the true profile and $\mathbf{G}$ describes the sensitivity of the retrieval to changes in the measurement. The columns of $\mathbf{A}$ describe the response of the retrieval system to delta function perturbations of the state parameter profile under investigation. The rows of $\mathbf{A}$ indicate which parts of the atmosphere have contributed how much to each point of the retrieved profile. The widths of the peaks seen in the rows are a useful measure of the vertical resolution of the retrieved profiles. The covariance matrix $\mathbf{S}_x$, which characterizes the uncertainities of the retrieved state parameter $\mathbf{x}$ caused by the observation error ε_y and the smoothing error caused by the constraining second term in (2.6), is given by

$$\mathbf{S}_x = (\mathbf{K}^T \mathbf{S}_y^{-1} \mathbf{K} + \mathbf{R})^{-1}.$$

2.4.2 Error Estimation

The random retrieval noise error $\mathbf{S}_{random}$ and systematic errors $\Delta \mathbf{x}_j$ due to uncertain parameter j are determined according:

$$\mathbf{S}_{random} = (\mathbf{K}^T \mathbf{S}_y^{-1} \mathbf{K} + \mathbf{R})^{-1} \mathbf{K}^T \mathbf{S}_y^{-1} \mathbf{K} (\mathbf{K}^T \mathbf{S}_y^{-1} \mathbf{K} + \mathbf{R})^{-1}, \tag{2.8}$$

and

$$\Delta \mathbf{y}_j = \mathbf{G} \Delta \mathbf{x}_j, \tag{2.9}$$

where $\Delta \mathbf{y}_j$ is the difference between the reference spectrum calculated using the retrieved profile $\hat{\mathbf{x}}$ and a spectrum calculated with parameter j perturbed by assumed 1σ uncertainity.

The total systematic error includes the uncertainities from all gases which are not jointly retrieved with the target gas and uncertainities from temperature, disregarded horizontal temperature gradient, line of sight, instrumental line shape, spectral shift, gain, forward model and spectroscopy.

Chapter 3

Gauss-Newton method versus the Improved Hessian Method

Most retrieval schemes use a linear approximation of the radiative transfer function within each iteration as well as for error analysis. Like most standard methods, the Hessian approach relies on quadratic form of the cost function and linear approximation in the error analysis. However, there is no well established objective criterion on choice of step sizes in the discrete perturbative calculation of the error covariance matrix (inverse Hessian). The improved Hessian method overcomes this drawback using adaptive algorithm which uses small step sizes in steep and large step sizes in shallow directions of the cost function in the error analysis. This is believed to suppress problem related to numerical noise. The Gauss-Newton-type and the Hessian are conceptually different so that the results from the two methods can be used for consistency checkup of the retrieved profiles and the corresponding covariance matrices. In the following, the difference between Gauss-Newton error covariance matrix and the inverse Hessian is demonstrated, the theoretical basis for improved Hessian and the adaptive algorithm are introduced and results of $ClONO_2$ and H_2O retrievals form simulated limb emission radiances by the two methods are compared.

3.1 Inverse Model Description

Suppose that we are seeking the minimum of the cost function at $\mathbf{x}_{i+1} = \mathbf{x}_i + \delta\mathbf{x}$, and the current estimate of the solution is $\mathbf{x}_i$. Then by Taylor expansion, the gradient of of the cost function in the x-space is

$$\bigtriangledown_x \chi^2(\mathbf{x}_{i+1}) = \bigtriangledown_x \chi^2(\mathbf{x}_i) + \bigtriangledown^2{}_x \chi^2(\mathbf{x}_i)(\mathbf{x}_{i+1} - \mathbf{x}_i). \tag{3.1}$$

Minimizing (3.1) by setting its gradient to zero gives

$$\bigtriangledown^2{}_x(\chi^2(\mathbf{x}_i))(\mathbf{x}_{i+1} - \mathbf{x}_i) = -\bigtriangledown \chi^2(\mathbf{x}_i). \tag{3.2}$$

The gradient $\bigtriangledown_x \chi^2(x_i)$ is calculated from (2.6) as

$$\bigtriangledown_x \chi^2(\mathbf{x}_i) = -2(\mathbf{K}_i{}^T \mathbf{S}_y{}^{-1}(\mathbf{y} - \mathbf{F}(\mathbf{x}_i)) + \mathbf{R}(\mathbf{x}_i - \mathbf{x}_a)), \tag{3.3}$$

and the Hessian matrix $\mathbf{H}$, i.e. $\bigtriangledown^2{}_x\chi^2(\mathbf{x}_i) = \frac{\partial^2\chi^2}{\partial\mathbf{x}_m\partial\mathbf{x}_n}|\mathbf{x}_o$, is calculated as

$$\mathbf{H} = \bigtriangledown^2{}_x(\chi^2(\mathbf{x}_i)) = 2(\mathbf{K}_i{}^T\mathbf{S}_y{}^{-1}\mathbf{K}_i - \bigtriangledown_x\mathbf{K}_i{}^T\mathbf{S}_y{}^{-1}(\mathbf{y}-\mathbf{F}(\mathbf{x}_i)) + \mathbf{R}). \tag{3.4}$$

Now, using (3.3) and (3.4) in (3.2) and rearranging lead to an iterative solution for the optimum state vector:

$$\begin{aligned}\mathbf{x}_{i+1} &= \mathbf{x}_i - (\frac{1}{2}\mathbf{H})^{-1}\bigtriangledown_x\chi^2(\mathbf{x}_i)\\ &= \mathbf{x}_i + (\mathbf{K}_i{}^T\mathbf{S}_y{}^{-1}\mathbf{K}_i - \bigtriangledown_x\mathbf{K}_i{}^T\mathbf{S}_y{}^{-1}(\mathbf{y}-\mathbf{F}(\mathbf{x}_i)) + \mathbf{R})^{-1}\\ &\times\ (\mathbf{K}_i{}^T\mathbf{S}_y{}^{-1}(\mathbf{y}-\mathbf{F}(\mathbf{x}_i)) + \mathbf{R}(\mathbf{x}_i-\mathbf{x}_a)).\end{aligned} \tag{3.5}$$

Assuming $\mathbf{F}(\mathbf{x})$ is moderately nonlinear allows to set $\bigtriangledown_x\mathbf{K}_i{}^T$ to zero, which gives the widely used iterative retrieval equation

$$\mathbf{x}_{i+1} = \mathbf{x}_i + (\mathbf{R}+\mathbf{K}_i{}^T\mathbf{S}_y^{-1}\mathbf{K}_i)^{-1}[\mathbf{K}_i{}^T\mathbf{S}_y^{-1}(\mathbf{y}-\mathbf{F}(\mathbf{x})) - \mathbf{R}(\mathbf{x}_i-\mathbf{x}_a)], \tag{3.6}$$

which is often used as a solution to a small residual moderately nonlinear problem. It is worthnoting that the covariance matrix $\mathbf{S}_x$ is related to the Hessian via $\mathbf{S}_x{}^{-1} \approx \frac{1}{2}\mathbf{H}$. As pinpointed by *Rodgers* [2000], both nonlinearity and noise contribute to the size of the ignored term, $\mathbf{K}_i{}^T\mathbf{S}_y{}^{-1}(\mathbf{y}-\mathbf{F}(\mathbf{x}_i))$. However, the small residual assumption may not always be satisfied. Large residuals may correspond to parameter changes beyond the linear domain of the solution, which may lead to an inaccurate error estimate. Inclusion of higher order terms in the Gauss-Newton iteration is computationally costly. Indeed, it is common to find retrieval algorithms which approximate even the forward model derivative with respect to VMR by its analytic form to reduce computational burden due to a repeated call to forward model. This is true for the variant of Gauss-Newton iterative formulation used here. On the other hand, the discrete evaluation of the Hessian directly from the cost function may be inaccurate because of significantly different scale of sensitivitiy of the cost function along different directions in the parameter space. The use of large step size along steep direction or a small step size along shallow directions leads to numerical noise and may enhance contributions from higher order terms. This suggests that when the range of eigenvalues of the inverse error matrix or alternately that of Hessian is large, efficient calculation of the uncertainities can be achieved by using an adaptive algorithm, which uses small step sizes in steep directions and large step sizes in flat directions of the cost function.

3.2 Calculation of Hessian

3.2.1 Discrete calculation of the Hessian

In this section we describe how the Hessian is calculated and how related numeric problems are solved. The dependence of χ^2 on the retrieval state vector, $\mathbf{x}_i$, near its minimum provides information on their uncertainities, i.e. the variations of χ^2 as a function of $\mathbf{x}_i$ is used to estimate the Hessian and the error matrix. These are usually characterized by the error matrix and the Hessian matrix $\mathbf{H}$. The equation describing the variation of the cost function near the minimum can be obtained from second order Taylor series expansion:

$$\chi^2(\mathbf{x}) = \chi^2(\mathbf{x}_0) + \frac{1}{2}(\mathbf{x}-\mathbf{x}_0)^T\bigtriangledown_x^2(\chi^2(\mathbf{x}_0))(\mathbf{x}-\mathbf{x}_0), \tag{3.7}$$

where $\mathbf{x}_0$ is the solution vector and $\mathbf{x}$ is a vector perturbed by small displacement from the solution. The first order term vanishes since the gradient is zero at $\mathbf{x}_0$ which is the minimum point in the parameter space. This is rewritten component-wise

$$\chi^2(\mathbf{x}) = \chi^2(\mathbf{x}_o) + \frac{1}{2}\sum_{m,n}\mathbf{H}_{m,n}(\mathbf{x}_m - \mathbf{x}_{0m})(\mathbf{x}_n - \mathbf{x}_{0n}), \tag{3.8}$$

from which the components $\mathbf{H}_{m,n}$ of the Hessian can easily be extracted by discrete perturbation without differentiating the forward model explicitly. However, the accuracy of Hessian from such perturbative calculation heavily depends on the right step size used, since the uncertainties are usually disparate for different directions in the n-dimensional parameter space, i.e. the eigenvalues of $\mathbf{H}$ span many orders of magnitude. Too large step sizes cause errors due to higher order terms while too small step size cause numerical noise. In order to estimate the Hessian with sufficient accuracy, the choice of appropriate step sizes for perturbative calculations is made by an adaptive algorithm.

3.2.2 Adaptive algorithm for calculation of Hessian

We impliment an iterative procedure which adapts the step sizes used in the numerical calculation of the Hessian to the uncertainities in each eigenvector direction as implimented by *Pumplin et al.* [2001] where this approach is used in different context. The Hessian defined in terms of its component, $\mathbf{H}_{m,n} = \frac{\partial^2\chi^2}{\partial\mathbf{x}_m\partial\mathbf{x}_n}$, and its eigenvector representations are extensively used in this paper.

The Hessian is a symmetric matrix by definition and satifies the eigenvalue equation:

$$\mathbf{HV} = \Lambda\mathbf{V}, \tag{3.9}$$

where Λ is a diagonal square matrix consisting of eigenvalues:

$$\Lambda_{mn} = \varepsilon_m\delta_{mn}.$$

The eigenvectors satisfy orthonormality conditions:

$$\sum_m \mathbf{V}_{mn}\mathbf{V}_{mk} = \delta_{nk}.$$

When the cost function has a quadratic form given in 3.7, an ellipsoid in parameter space is traced by a given value of χ^2. When the directions of the major axis of the ellipsoid coincide with the directions of the parameter coordinate system, the Hessian matrix is diagonal and the parameters are said to be uncorrelated. If this is not the case, the Hessian can be made diagonal by a coordinate transformation to the major axes. The eigenvectors provide a natural basis to express arbitrary variations around the minimum by making a rotation in parameter space around the centre of the ellipsoid, given by vector equation:

$$\mathbf{x} - \mathbf{x}_0 = \mathbf{VEz}, \tag{3.10}$$

where $\mathbf{E}$ is square matrix given by

$$\mathbf{E}_{i,j} = \frac{1}{\sqrt{\varepsilon_i}}\delta_{ij}$$

and $\mathbf{z}$ is a vector consisting of displacement of each parameter from minimum in natural coordinate and $\mathbf{x} - \mathbf{x}_0$ is displacement vector in the parameter coordinate.

Under this transformation, (3.8) becomes

$$\chi^2(\mathbf{x}) - \chi^2(\mathbf{x}_o) = \frac{1}{2}(\mathbf{x} - \mathbf{x}_0)^T \mathbf{H}(\mathbf{x} - \mathbf{x}_0) = \sum_i \mathbf{z}_i^2, \tag{3.11}$$

and Hessian and its inverse are given by:

$$\mathbf{H} = \mathbf{V}\Lambda\mathbf{V}^T, \tag{3.12}$$

and

$$\mathbf{H}^{-1} = \mathbf{V}\Lambda^{-1}\mathbf{V}^T. \tag{3.13}$$

The parameters $\mathbf{z}_i$ are the natural choice for accurately estimating the Hessian by sampling the values of χ^2 in the parameter space. However, they are not available in advance. Therefore, we employ an iterative procedure as described in *Pumplin et al.* [2001]. This approach tries to seek the right step size in calculating the Hessian by iteratively determining the natural coordinate. It chooses the optimum step size which balances the errors from higher order terms for too large increment and numerical noise from too small increment.

The algorithm for the adaptive procedure is:

1. Define a new set of coordinates ζ_j by

$$\mathbf{x}_i - \mathbf{x}_0 = \sum_j \mathbf{U}_{ij}\mathbf{t}_j\zeta_j$$

where $\mathbf{U}_{ij}$ is orthogonal matrix and $\mathbf{t}_i$ are scale factors. As the iteration proceeds, $\mathbf{U}_{ij}$,$\mathbf{t}_i$ and ζ_i converge to $\mathbf{V}_{ij}$,$\sqrt{(2/\varepsilon_i)}$, and $\mathbf{z}_i$ respectively.

2. Compute pseduo Hessian in ζ_i

$$\tilde{\mathbf{H}} = \frac{\partial^2\chi^2}{\partial\zeta_i\partial\zeta_j}$$

and transform (3.8):

$$\chi^2(\zeta) = \chi^2(\zeta_o) + \frac{1}{2}\sum_{m,n}\tilde{\mathbf{H}}_{m,n}(\zeta_m - \zeta_{om})(\zeta_n - \zeta_{on}). \tag{3.14}$$

The step size $(\zeta_m - \zeta_{om})$ is selected such that the change of χ^2 due to the diagonal element $\frac{1}{2}\frac{\partial^2\chi^2}{\partial{\zeta_j}^2}{\zeta_j}^2$ is approximately equal to one. This is an appropriate choice for a χ^2 function obeying ideal statistical requirements. However, the results are not sensitive to that choice.

3. Compute the Hessian by coordinate transformation

$$\mathbf{H}_{ij} = \sum_{i,j}\frac{\tilde{\mathbf{H}}_{mn}\mathbf{U}_{im}\mathbf{U}_{jn}}{\mathbf{t}_m\mathbf{t}_n}$$

4. Find the normalized eigenvectors of the Hessian according to (3.12) and (3.13).

5. Replace $\mathbf{U}_{ij}$ by $\mathbf{V}_{ij}$, $\mathbf{t}_j$ by $\sqrt{(2/\varepsilon_j)}$ and then go to step 1 until pseudo Hessian converges to δ_{ij}.

The gradient of the cost function, $\bigtriangledown_x\chi^2(\mathbf{x}_i)$, is also calculated during each iteration with the same step size used to calculated the Hessian matrix for updating the retrieval vector.

Using $\mathbf{S}_x^{-1} = \frac{1}{2}\mathbf{H}$, the errors of retrieval state vector $\mathbf{x}_m$ can be calculated as:

$$(\delta x_m)^2 = 2(\chi^2(\mathbf{x}) - \chi^2(\mathbf{x_o}))\sum_{\mathbf{n}} \frac{\mathbf{V_{mn}}^2}{\varepsilon_\mathbf{n}}. \tag{3.15}$$

This equation can be used to see if each element of state vector is appropriately well determined. The eigenvectors $\mathbf{V}_{mn}$ dominating the retrieval error can be easily identified.

3.3 Application to Atmospheric Spectroscopy

For this case study we have generated synthetic measurements in the $ClONO_2$ ν_4 Q-branch region at 780.2 cm^{-1} and H_2O over selected spectral microwindows from 760.625 cm^{-1} to 1657.35 cm^{-1} for tangent heights from 12 to 50 km at 3 km vertical spacing with the KOPRA radiative transfer algorithm [*Stiller*, 2000]. Spectral noise of 50 nW/(cm^2 sr cm^{-1}) has been superimposed to the spectra. These synthetic measurements have been used for a H_2O and $ClONO_2$ profiles retrieval study using the retrieval processor which is employed at IMK to infer atmospheric state parameters from MIPAS measurements [*von Clarmann et al.*, 2003b]. This retrieval algorithm uses the conventional Gauss-Newton approach in a sense that the curvature (residual) term in the retrieval equation is ignored. Starting from these results the Hessian method is then used for both refinement of results and to achieve a more accurate error estimate.

3.3.1 Comparison method

The comparison of two retrieval algorithms should include the averaging kernels, to characterize the altitude resolution, the retrieval noise covariance matrix, to characterize the accuarcy and precision of the retrieval and the degree of freedom of retrieval by direct analogy of intercomparison of two observing systems [*Rodgers and Connor*, 2003]. Following the approach of *Rodgers* [1990, 2000]; *Rodgers and Connor* [2003], the retrieved profile $\mathbf{x}$ is related to the true profile $\mathbf{x}_t$ and a priori information used in its retrieval by

$$\mathbf{x} - \mathbf{x}_a = \mathbf{A}(\mathbf{x}_t - \mathbf{x}_a) + \sigma_{random}, \tag{3.16}$$

where σ_{random} is the square root of the diagonal elements of random noise covariance $\mathbf{S}_{random}$ and $\mathbf{A}$ is the averaging kernel. However, comparison of two retrieval algorithms is far less complicated than intercomparison of two observing systems in many ways. The random noise errors from the two retrieval algorithms, which are due to errors (noise plus systematic) in the measured signal and the forward model, differ only in the forward model approximation such as, e.g. approximate equivalence of the Hessian and inverse error matrix. Moreover, in the case of simulated measurement the true state is known and the a priori used can be made the same for both retrievals. The difference between profile calculated according to (3.16) and the actual retrieved profile should be

within the bound of the smoothing error which is not included in the former for a linear forward model. The departure from this limit highlights the extent of how far the solution is from linear region.

The difference between profiles calculated from (3.16) should come from difference in the averaging kernel and the random noise error as shown below:

$$\mathbf{x}_{GN} - \mathbf{x}_H = (\mathbf{A}_{GN} - \mathbf{A}_H)(\mathbf{x}_t - \mathbf{x}_a) + \sigma_{random,GN} - \sigma_{random,H}, \tag{3.17}$$

where subscript *GN* and *H* refer to corresponding quantities as determined by Gauss-Newton and Hessian algorithms respectively.

The averaging kernel **A** is given by

$$\mathbf{A}_{GN} = \frac{\partial \mathbf{x}}{\partial \mathbf{x}_t} = (\mathbf{K}^T \mathbf{S}_y^{-1} \mathbf{K} + \mathbf{R})^{-1} \times \mathbf{K}^T \mathbf{S}_y^{-1} \mathbf{K},$$

for Gauss-Newton algorithm which translates to

$$\mathbf{A}_H = (\frac{1}{2}\mathbf{H})^{-1}(\frac{1}{2}\mathbf{H} - R),$$

for Hessian retrieval algorithm. The averaging kernel is a useful diagnostic tool apart from quantifying the contribution of measurement and a priori information to the retrieved profile. It provides the degree of freedom of the retrieval as a sum of its diagonal elements and the vertical resolution of the retrieval as full width at half maximum (FWHM) of its columns.

The random retrieval noise covariance matrix $\mathbf{S}_{random,GN}$, from which $\sigma_{random,GN}$ is extracted, is given by

$$\mathbf{S}_{random,GN} = (\mathbf{K}^T \mathbf{S}_y^{-1} \mathbf{K} + \mathbf{R})^{-1} \mathbf{K}^T \mathbf{S}_y^{-1} \mathbf{K} (\mathbf{K}^T \mathbf{S}_y^{-1} \mathbf{K} + \mathbf{R})^{-1}. \tag{3.18}$$

The corresponding equation for $\mathbf{S}_{random,H}$ by the same analogy is given by

$$\mathbf{S}_{random,H} = (\frac{1}{2}\mathbf{H})^{-\mathbf{1}}(\frac{\mathbf{1}}{\mathbf{2}}\mathbf{H} - \mathbf{R})(\frac{\mathbf{1}}{\mathbf{2}}\mathbf{H})^{-\mathbf{1}}.$$

The extent of forward model nonlinearity can be appreciated by comparing the maximum and minimum curvature radii $r_{max} = \sqrt{\frac{1}{1-\lambda_{max}}}$ and $r_{min} = \sqrt{\frac{1}{1-\lambda_{min}}}$ with unity. λ_{max} and λ_{min} are the maximum and minimum eigenvalues of the **B** matrix, related to the Hessian by

$$\mathbf{B} = \mathbf{I} - \frac{1}{2}\mathbf{C}^{-1}\mathbf{H}(\mathbf{C}^{-1})^T, \tag{3.19}$$

where $\mathbf{C}^T\mathbf{C}$ is the Cholesky decomposition of $\mathbf{K}^T\mathbf{S}_y^{-1}\mathbf{K} + \mathbf{R}$. The closer they are to unity the smaller is the curvature (i.e. second derivative of the forward model) [*Bates and Watts*, 1980].

The measurement error can be characterized by diagonal elements of the error covariance matrix which are the traditional variance of the retrieval at each level. However, because of the correlations between levels, this is underestimate of the knowledge of the retrieved profile [*Rodgers*, 1990]. Therefore, a more general approach to understanding of correlated errors is to work in a coordinate system orthogonally transformed from the original state space. In such coordinate system, e.g. the natural coordinate formed by inverse transformation of (3.10), the quantity $\mathbf{z}_i$ are

independent with unit variances. This is indeed the coordinate system used to calculate the inverse error matrix in the Hessian approach. Therefore, the χ^2 in this coordinate system as a function of distance from the minimum should obey ideal χ^2 quadratic behavior for a perfect retrieval as given in (3.11).

3.3.2 Results and Discussion

Water vapour (H_2O)

The retrieved profiles and their estimates from (3.16) under moderately non-linear assumption are shown in Fig. 3.1 for Hessian and Gauss-Newton algorithms in top left and bottom left quadrats respectively. The corresponding difference between retrievals and their linear estimates are shown in the top right and bottom left quadrats of the same Figure. The differences are as high as 117 ppmv and 157 ppmv at lowest retrieval grid for retrieved H_2O by Hessian and Gauss-Newton methods respectively. The departures from linear estimates diminish with altitude up to 10 km and 11 km for the Hessian and Gauss-Newton method respectively. Above the respective altitudes, the linear approximations seem to be very sufficient as indicated by quite good agreement between retrieved profiles and their linear approximations. The deviations at lower altitudes are also beyond the range covered by smoothing error, e.g about 80 ppmv and 77 ppmv at lowest altitudes as compared to 117 ppmv and 157 ppmv in this order. Therefore, the linear approximations at lower altitudes are not representative of the retrieved profiles, being worse in Gauss-Newton than the Hessian.

The random noise retrieval errors for Hessian and Gauss-Newton retrievals are shown in the left panel of Fig. 3.2. The random noise error from Gauss-Newton retrieval is larger than that estimated from error covariance matrix of the Hessian retrieval method at altitudes below 10 km with maximum of 1.3 ppmv at 5 km level. The random noise error from Hessian method is larger than corresponding estimate from Gauss-Newton above 48 km by about 0.1 ppmv. The large values at lower levels are probably due to the positive contribution of the curvature term to the Hessian matrix which has the inverse effect in the inverse Hessian (error matrix). This point will be further investigated by assessing the extent of forward model nonlinearity as described in the preceeding section. The random noise retrieval errors estimated from the two methods within altitude range of 10-48 km are in quite good agreement.

The extent of forward model nonlinearity can be assessed based on the minimum and maximum curvature radii calculated from minimum and maximum eigenvalues of **B** matrix given in (3.19). The minimum curvature radius is about 0.89 while the maximum is about 1.06 which differ from unity by 0.11 and 0.06 in this order. At first glance, the departures from unity seem to be insignificant, however, this can only be appreciated by comparing with other species which exhibit weaker nonlinearity as compared to water vapour. These values, for instance, are significantly larger than deviations in curvature radii from unity calculated for $ClONO_2$ in the next section.

The eigenvalues of the inverse error matrix (Hessian) spans a range of 0.36e-04 to 96.496300 i.e. several order of magnitude difference between the flattest and steepest directions as shown in Fig. 3.3 (left panel). The contour plot in Fig. 3.3 (right panel) shows the contributions of each eigenvector directions to uncertainities of elements of state vector (i.e. elements of the quantity

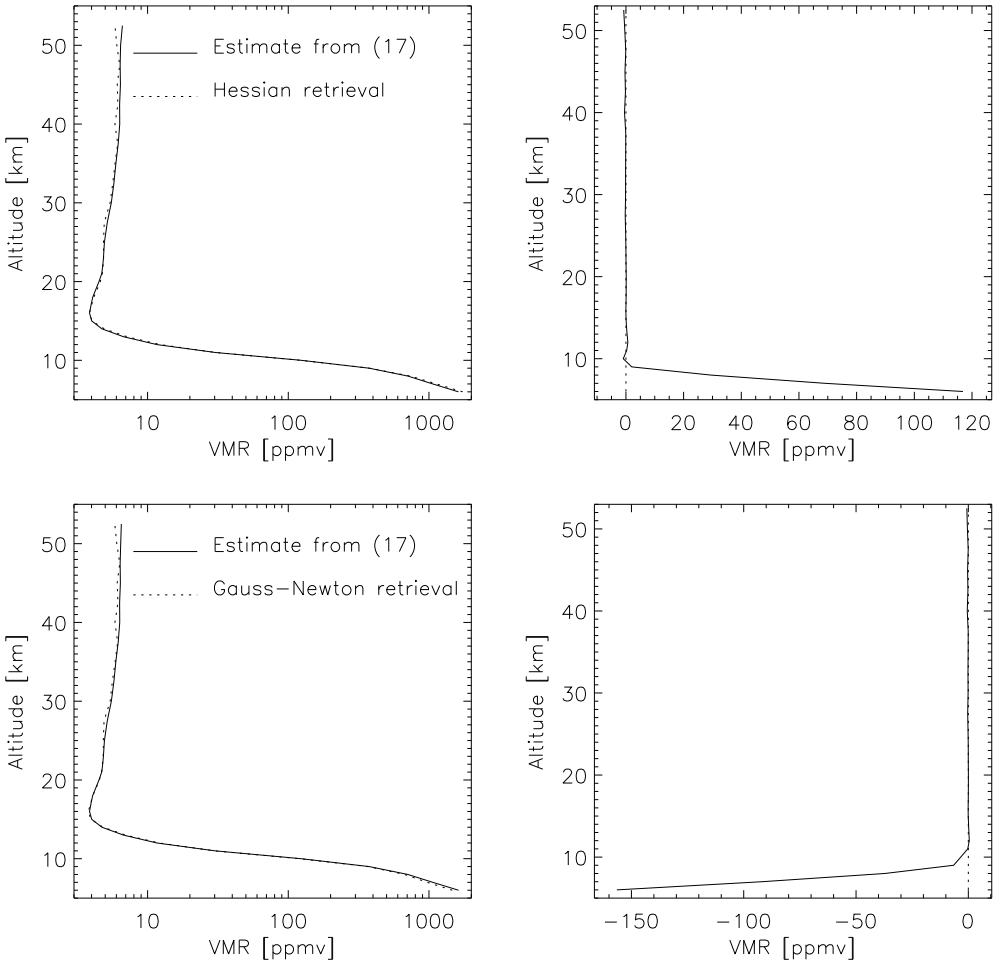

Figure 3.1: Retrieved profiles and their linear estimates for H_2O according to Hessian (top left) and Gauss-Newton methods (bottom left). The top right and bottom right panels represent the difference between the retrieval and linear estimate for the respective methods.

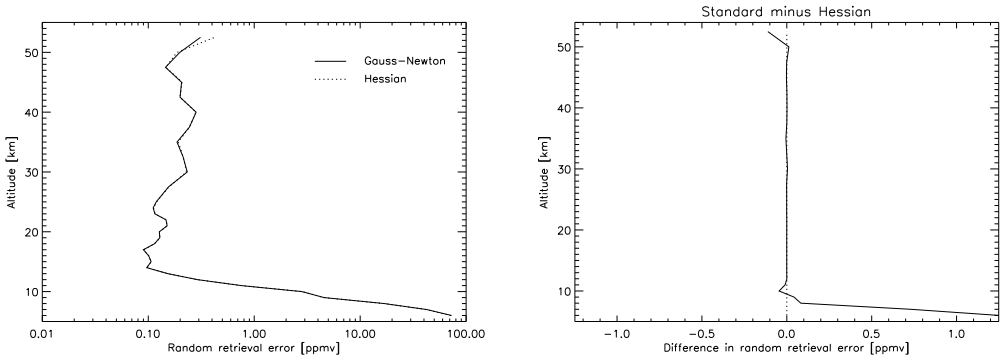

Figure 3.2: The bottom left and right panels represent the random errors estimated using the two algorithms and their difference respectively.

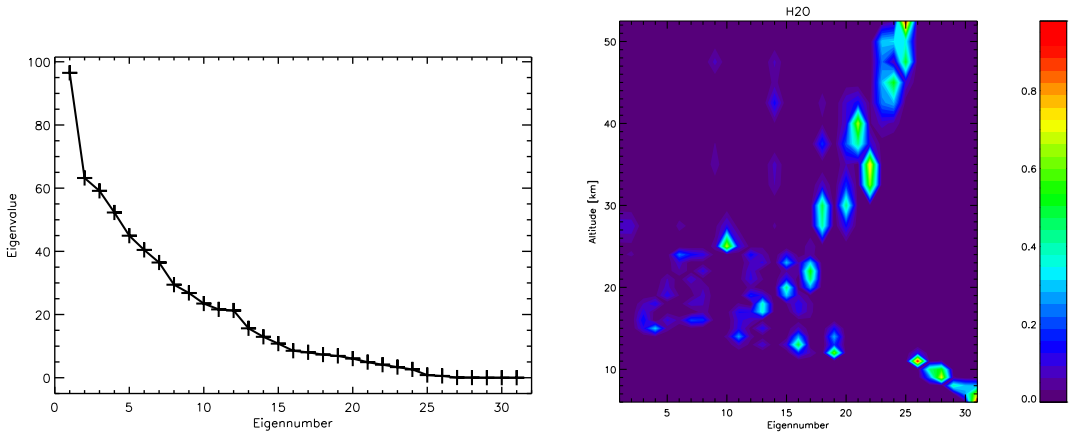

Figure 3.3: Left: Eigenvalue of the inverse error matrix for H_2O. Right: The contributions of each eigenvector direction (along the horizontal axis) for a unit change in χ^2 along each state parameter $\mathbf{z_i}$ (at altitudes *i* along the vertical axis) for H_2O retrievals.

z, the natural coordinate system orthogonally transformed) at the given altitudes. The wide range of the eigenvalues makes the smaller eigenvalues and their eigenvectors more sensitive to fine details of the Hessian matrix. This problem has been tamed by computing the eigenvalues and eigenvectors by succesive approximations as described in Section 3.2 in the improved Hessian approach that converge even in the presence of numerical noise and non-quadratic contribution to χ^2. The uncertainities in the quantiy **z** at and below altitude of 10 km are governed mostly by flattest eigenvector directions which contribute to more than 80% of the variance as indicated in the color coding. These eigenvector directions are highly sensitive to fine details of the inverse covariance matrix. The uncertainities of **z** in the altitude range of approximately 11-28 km spread over a wide range of eigenvector directions from 1 to 19. The uncertainities in **z** in the altitude range of 29-48 come from eigenvector directions from 18 to 24 with significant proportion coming from increasing eigenvector directions with altitude. The cause of the difference can not be numerical calculations since the Gauss-Newton method uses analytic Jacobians with respect to VMR. However, the implimentation of the analytic Jacobian is realized after ignoring terms involving the derivative of the source function and the absorption coefficient through the dependence of the Curtis-Godson temperature value on VMR which are likely contributing factors. The comparison of the analytic Jacobian with numerically calculated Jacobian has already indicated differences which can be minimized by reducing the thickness of atmospheric layers and can also be ignored as a trade-off between accuracy and computational time [*Stiller*, 2000]. But the numerical approach in that study is different from the improved Hessian method which optimally balances numerical noise and higher order contributions.

We further explored the behaviour of χ^2 in this new coordinate system as function of $\mathbf{z}_i$ at selected altitudes *i*. Figs. 3.4-3.5 show the functional response of χ^2 with displacement from minimum for altitudes of 6, 11, 27.5 and 52.5 kms for both retrieval results. The dominating contribution of observed uncertainities at lower altitudes from flattest directions makes difficult to accuartely estimate the variance in $\mathbf{z}_i$ at these altitudes. This is highlighted by the significant departure of χ^2 from quadratic as a function of $\mathbf{z}_i$ at 6 km for Gauss-Newton algorithm and slightly improving at 11 km following significant reduction in the contribution of the most flattest eigenvector directions to the uncertainity (see left panel of Fig. 3.3). The χ^2 as function of $\mathbf{z}_i$ based on Hessian retrieval

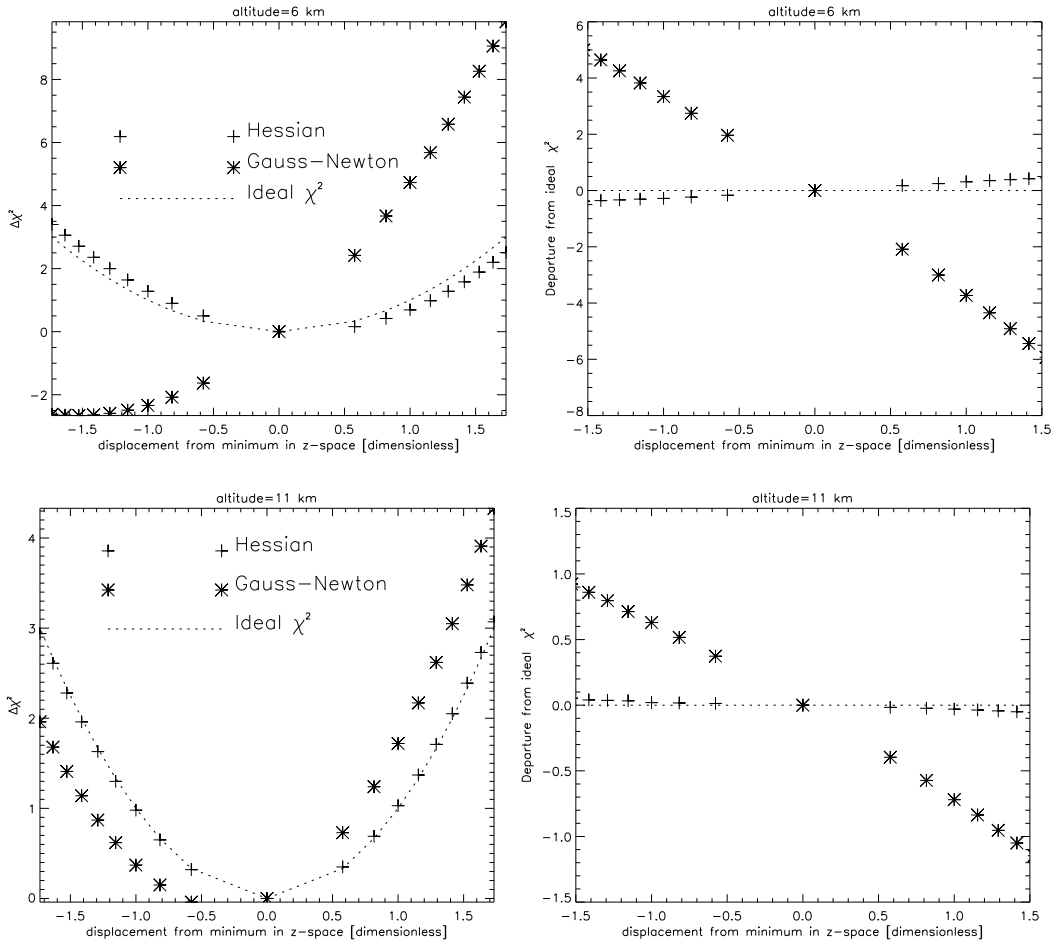

Figure 3.4: Left: The distribution of $\Delta\chi^2$ as a function of a departure of profile from minimum in **z**-space for H_2O for altitudes of 6 and 11 kms. Right: The departure of χ^2 from ideal quadratic form indicated by the same symbols in the left panel for Hessian and Gauss-Newton.

is fairly quadratic though not perfect. The Hessian method overcomes the problem related with flattest and highly sensitive eigenvector directions by successive approximations described above. The accuracy improves for both Hessian and Gauss-Newton methods for higher altitudes which are governed by steepest to moderately steep eigenvector directions, e.g. as shown for 27.5 and 52.5 kms in Fig. 3.5.

Another way to compare the two methods is to look at whether there is additional information content due to the implicit inclusion of the curvature term in the Hessian method and/or improved accuracy in calculation of the Hessian matrix. The degree of freedom calculated from the corresponding averaging kernel is increased from 10.93 to 10.99, though it could be considered the same in practical terms. The vertical resolution improved by about 0.5 km near altitude of 10 km, slightly deteriorating by a small fraction of a kilometer near 30 km and again improving around 35 km (see Fig. 3.6). The most dramatic improvement in the vertical resolution of Hessian retrieval is above 48 km which is better than the vertical resolution of Gauss-Newton retrieval by 4 km.

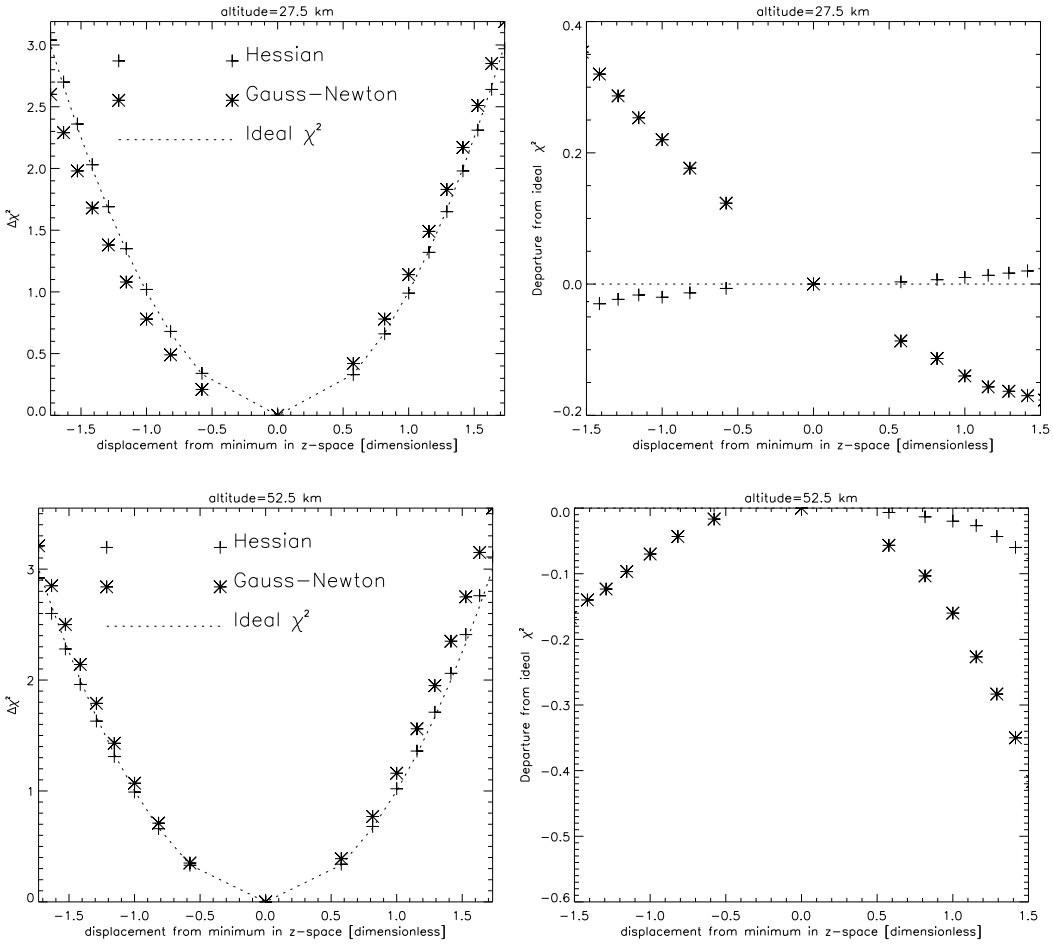

Figure 3.5: Left: The distribution of $\Delta\chi^2$ as a function of a departure of profile from minimum in natural coordinate for H_2O for altitudes of 27.5 and 52.5 kms. Right: The departure of χ^2 from ideal quadratic form indicated by the same symbols in the left panel for Hessian and Gauss-Newton.

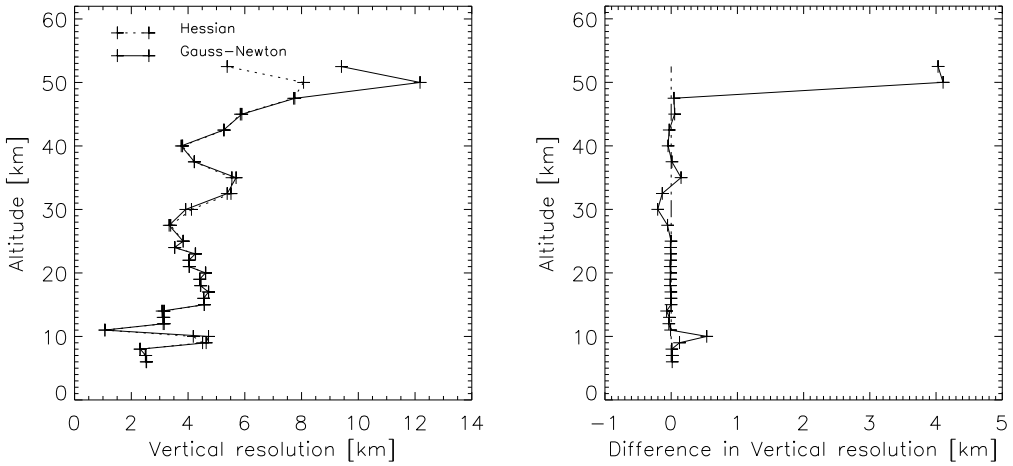

Figure 3.6: The vertical resolutions of H_2O retrievals form the two methods as noted in the legend and their differences.

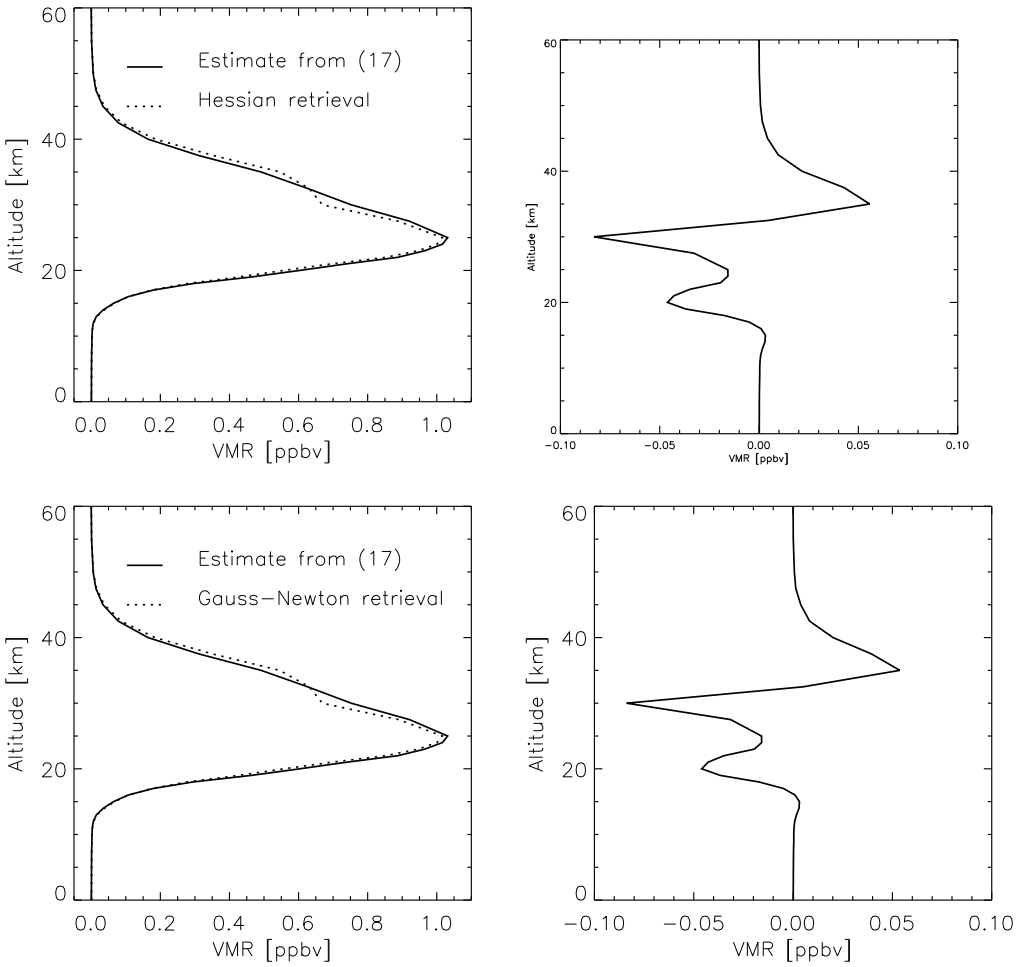

Figure 3.7: As in Fig. 3.1 but for $ClONO_2$ profiles and their departure from linear estimates.

Chlorine nitrate ($ClONO_2$)

Retrieved $ClONO_2$ profiles and their linear approximations are given in Fig. 3.7 for Hessian in top left quadrat and Gauss-Newton in bottom left quadrat. The differences between retrieved values and linear approximations near 35 km are about 8% which lie within the smoothing error bound of approximately 8% for both retrievals. However, the departures of about 0.85 ppbv at 30 km are beyond the limit allowed by the smoothing error.

The random noise retrieval errors for Hessian and Gauss-Newton retrievals are shown in the left panel of Fig. 3.8. The random noise error from Gauss-Newton retrieval is larger than that estimated from error covariance matrix of the Hessian retrieval method at altitudes above 30 km with maximum of 0.14 pptv at 35 km level. Between 15-30 km, the random noise error from Hessian method is larger than corresponding estimate from Gauss-Newton by about at most 0.13 pptv. The altitude of maximum differences is located in the range of 27-37 km.

The nonlinearity does not seem to contribute much to the observed discrepancies since the minimum and maximum curvature radii for $ClONO_2$ are about 0.99 and 1.01 respectively in contrast

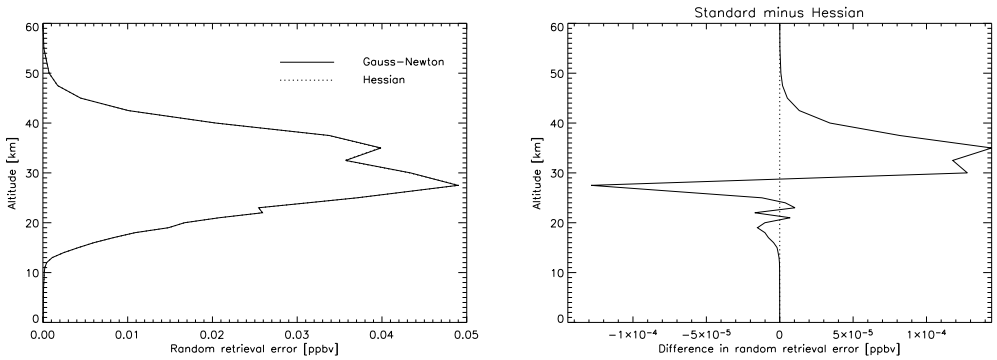

Figure 3.8: As in Fig. 3.2 but for $ClONO_2$ random noise error and difference in these values from the two methods.

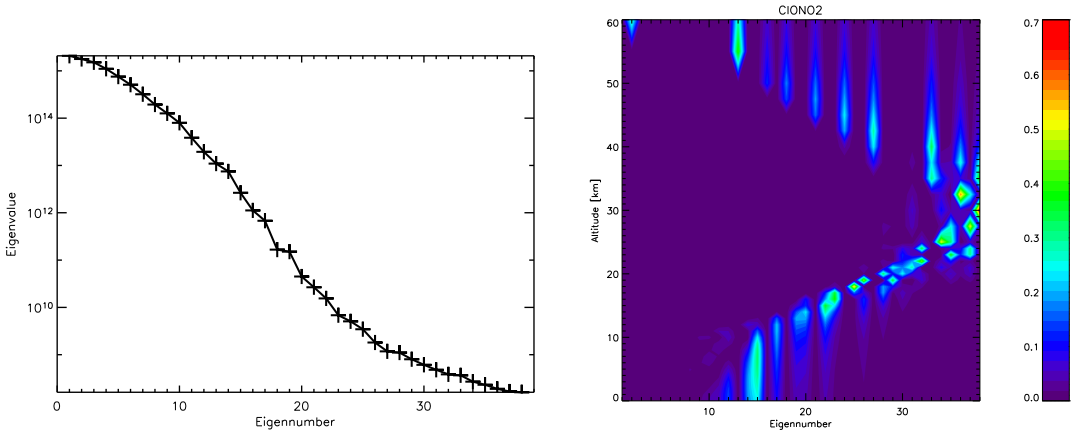

Figure 3.9: As in Fig. 3.3 but for $ClONO_2$ retrievals based on the two methods.

to corresponding values for H_2O. The contributions of eigenvector directions to a unity variance in the transformed quantity $\mathbf{z}_i$ at each altitude i in right panel of Fig. 3.9 show that the variance contributions to $\mathbf{z}_i$ at altitudes of 27-37 mainly come from shallowest directions. The departure from linear approximation at 30 km (see Fig. 3.7) is also related to the shallowest eigenvector directions indicating that the source of the problem is the high sensitivity of this direction in the fine details of Hessian matrix calculation or equivalently the inverse Hessian.

The variation of χ^2 in $\mathbf{z}$ coordinate as a function of displacement from the solution is expected to be quadratic. This is shown for $ClONO_2$ in Fig. 3.10-3.11 for altitudes of 10, 25, 37.5 and 50 kms. Unlike the water vapour retrievals, χ^2 is nearly quadratic far beyond the proximity of minimum for both retrieval results suggesting that effect of model nonlinearity is minimal. The accuracy with which the uncertainities are determined, however, is affected by the wide range of eigenvalues. The performance of the Hessian approach in estimating the uncertainities in $\mathbf{z}_i$ which come mainly from shallow directions is better than the Gauss-Newton method. A good example in support of this argument is the behaviour of χ^2 as a function of $\mathbf{z}_i$ at 37.5 km in Fig. 3.11. The variance in $\mathbf{z}_i$ at this altitude is governed by shallow directions (see Fig. 3.9) as compared to other levels in the same plot of Fig. 3.11 and Fig. 3.10. χ^2 as a function of $\mathbf{z}_i$ shows asymmetric variance. Moreover, at a distance equal to 1σ of $\mathbf{z_i}$ i.e. unity the χ^2 value deviaties by 10% from expected value of unity.

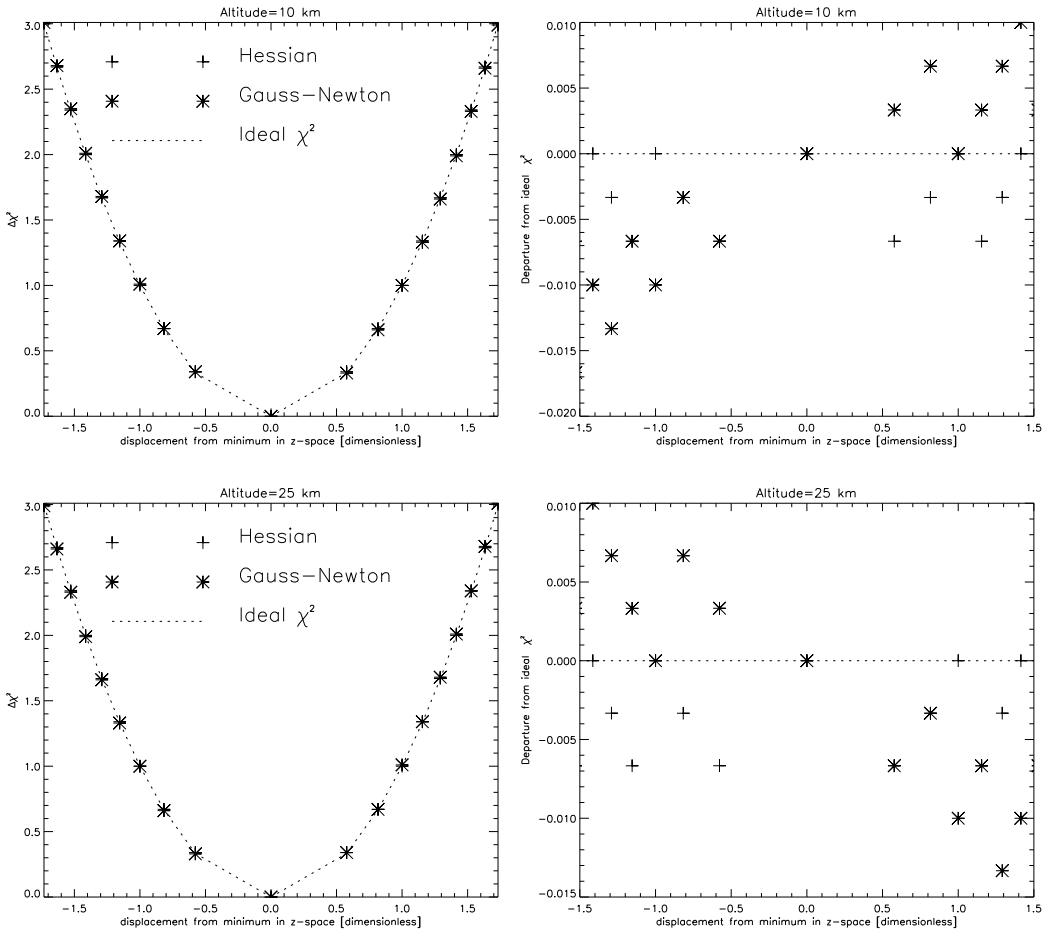

Figure 3.10: Left: The distribution of $\Delta\chi^2$ as a function of a departure of profile from minimum in **z**-space for $ClONO_2$ for altitudes of 10 and 25 kms. Right: The departure of χ^2 from ideal quadratic form indicated by the same symbols in the left panel for Hessian and Gauss-Newton.

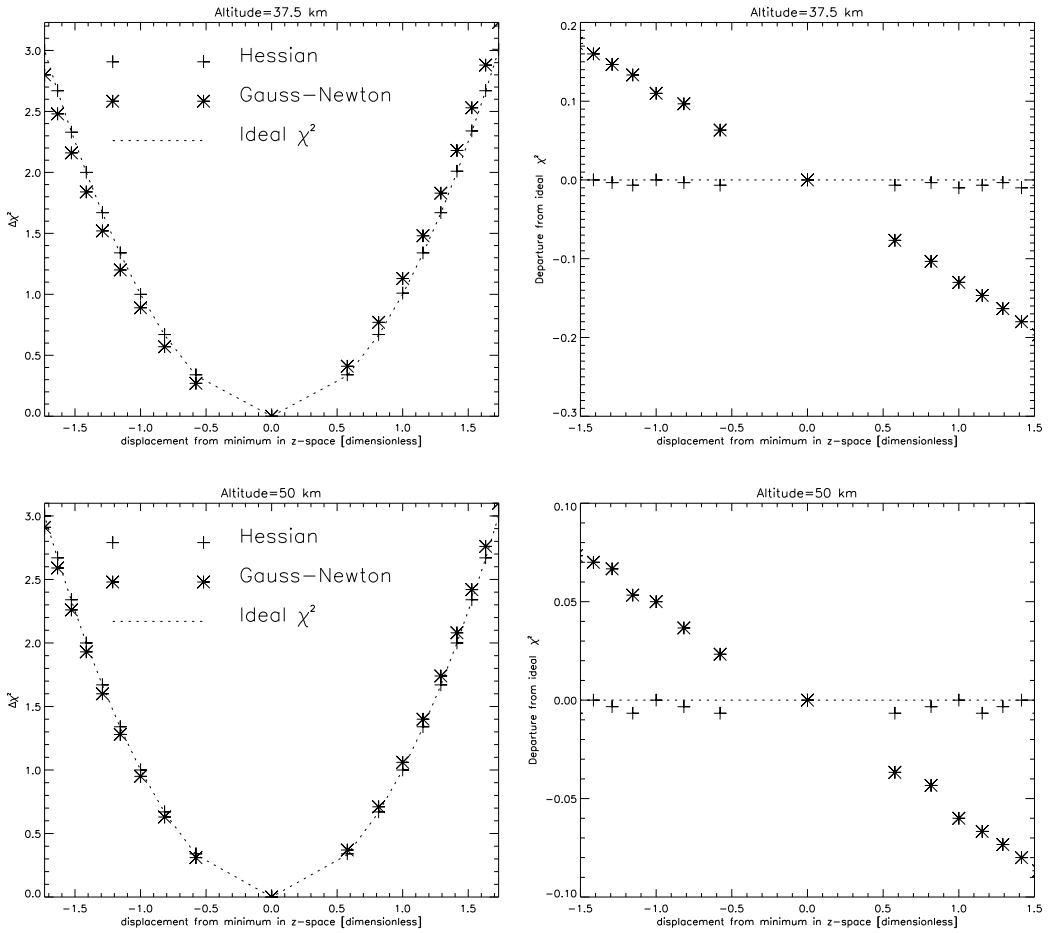

Figure 3.11: Left: The distribution of $\Delta\chi^2$ as a function of a departure of profile from minimum in **z**-space for $ClONO_2$ for altitudes of 37.5 and 50 kms. Right: The departure of χ^2 from ideal quadratic form indicated by the same symbols in the left panel for Hessian and Gauss-Newton.

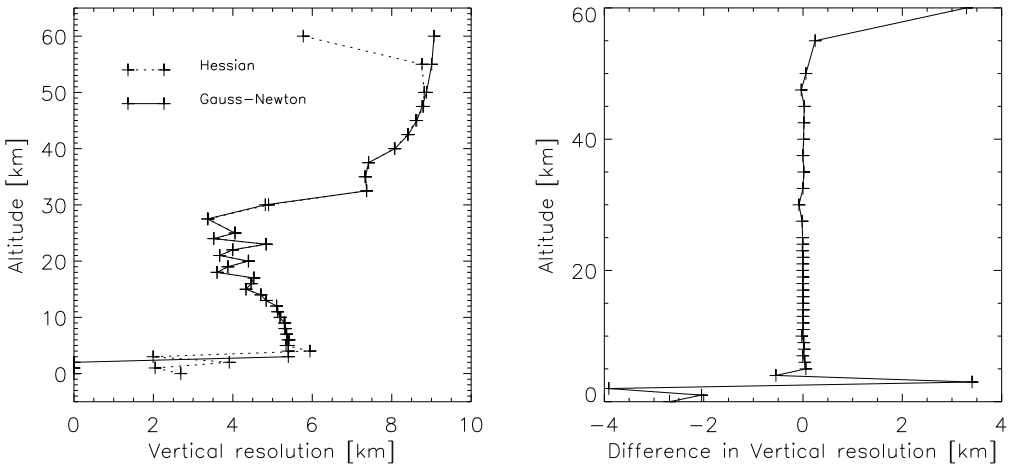

Figure 3.12: The vertical resolutions of $ClONO_2$ retrievals form the two methods as noted in the legend and their differences.

The degrees of freedom of retrieval, i.e. trace of the averaging kernel, as computed from the averaging kernels are 5.0 in both retrievals. The vertical resolution of the retrievals showed some differences. The vertical resolution of retrievals which were not possible to calculate for the lowest three altitudes in the case of Gauss-Newton averging kernel turned out to be between 2 to 4 km in the case of Hessian retrievals as indicated in Fig. 3.12. There are also some improvement in the resolution above 50 km while at most retrieval grids the vertical resolution is identical (see left panel of Fig. 3.12).

Chapter 4

Retrieval of N_2O_5, an important component of NO_y

In this chapter we present and discuss an approach to the retrieval of N_2O_5, which solves the problem to distinguish between the continuum-like N_2O_5 spectral signature and the background continuum radiance signal, and apply this approach to a MIPAS data set recorded in Austral spring 2002.

4.1 Retrieval of N_2O_5

4.1.1 General Retrieval Sequence and Specific Strategy for Retrieval of N_2O_5

Species retrievals are the third step in the retrieval chain, after retrieval of spectral shift, temperature and pointing information [*von Clarmann et al.*, 2003b]. The retrieval processor derives the atmospheric and instrumental state parameters by constrained nonlinear least squares fit, using the Karlsruhe Optimized and Precise Radiative Transfer Algorithm (KOPRA) for the forward modeling of radiative transfer [*Stiller*, 2000]. For retrieval of N_2O_5, the radiative transfer modeling assumes local thermodynamic equilibrium (LTE). The spectroscopic data were taken from the HITRAN database [*Rothman et al.*, 1998], which includes cross-section data for N_2O_5 [*Cantrell et al.*, 1988].

The abundance profiles of N_2O_5 are retrieved from its ν_{12} vibration-rotation band. While ν_{12} is a prominent band, this spectral region also contains significant contributions from CH_4, N_2O and H_2O. Furthermore, the N_2O_5 line widths are larger than line spacings such that its signal is continuum-like. In effect, the quasi-continuum made up by far line wings of other species of uncertain abundances and particle continua from aerosols and clouds contribute to the continuum-like signal, which makes it difficult to separate the N_2O_5 emission.

The background continuum in the ν_{12} band is assumed to be approximately the same as that found in the spectral region near the ν_{12} band. On the basis of this assumption, we propose a retrieval scheme which includes a spectral region virtually free of any N_2O_5 signal and constrains contin-

uum signal of other species and particle continuum in the ν_{12} band to values in the N_2O_5-free spectral region. Two so-called microwindows within the ν_{12} band and one external microwindow were selected for this purpose. The N_2O_5-free spectral microwindow covers spectral region 1215.725 - 1216.725 cm^{-1} while the target analysis windows cover 1239.0 - 1243.0 cm^{-1} and 1275.0 - 1276.0 cm^{-1} of the ν_{12} band. These microwindows belong to band B of MIPAS instrument with NESR between 12 and 16 nW/(sr cm^2 cm^{-1}) inferred from inflight measurements. These values are slightly higher than the preflight estimates but lower than the requirements. In analysis of spectra recorded from a balloon-borne platform (MIPAS-B), the continuum problem was solved by using a large analysis window, which contains also regions of negligible N_2O_5 signal [*Wetzel et al.*, 1995]. Excessive computational requirements of this approach, however, are prohibitive for analysis of large amounts of data as in the case of MIPAS/ENVISAT.

4.1.2 Elements of the state vector and regularization in N_2O_5 retrieval

The nominal strategy in IMK retrieval processor for infering geophysical variables is the joint retrieval of target gas, main interfering species (optional) in the retrieval spectral window, a constant absolute radiance offset per spectral window for compensation of zero-level radiance calibration uncertainities and continuum absorption coefficients for altitudes below 33 km and per spectral window. Therefore, the state vector of unknown variables in (2.7) consists of the VMRs of the target gas and main interfering species at altitudes of the retrieval grid, altitude-constant absolute radiance offset per spectral window and continuum optical thickness per altitude and spectral window. The main interfering species in the case of N_2O_5 retrieval are CH_4, N_2O and H_2O, which are included in the state vector. All further interfering gases are considered in the forward calculation but not adjusted during the retrieval. The regularization matrix $\mathbf{R}$ for the state vector consists of block matrices along its diagonal i.e.

$$\mathbf{R} = \begin{bmatrix} \mathbf{R}_{N_2O_5} & (0) & (0) & (0) & (0) & (0) \\ (0) & \mathbf{R}_{CH_4} & (0) & (0) & (0) & (0) \\ (0) & (0) & \mathbf{R}_{N_2O} & (0) & (0) & (0) \\ (0) & (0) & (0) & \mathbf{R}_{H_2O} & (0) & (0) \\ (0) & (0) & (0) & (0) & (\mathbf{R}_{cont}) & (0) \\ (0) & (0) & (0) & (0) & (0) & (\mathbf{R}_{offset}) \end{bmatrix},$$

where $\mathbf{R}_{N_2O_5}$, $\mathbf{R}_{CH_4}$, $\mathbf{R}_{N_2O}$, $\mathbf{R}_{H_2O}$, $\mathbf{R}_{cont}$, and $\mathbf{R}_{offset}$ are regularization matrices for N_2O_5, CH_4, N_2O, H_2O, continuum and offset respectively. The regularization matrices, $\mathbf{R}_{N_2O_5}$, $\mathbf{R}_{CH_4}$, $\mathbf{R}_{N_2O}$, and $\mathbf{R}_{H_2O}$, are constructed based on a variant of Tikhonov's first derivative operator for smoothing the profiles [*Steck*, 2002]. The off-diagonal matrices are filled with zeros.

The altitude grid used for N_2O_5 retrieval consists of 60 levels with 1 km altitude width up to 44 km and 2-10 km width up to 120 km. The initial guess profiles used for retrieval, which is the same as the a priori profiles in our application, are achieved from various sources ranging from remote to in-situ measurements which allows differences in the climatology of the geolocations. The joint-fit gases CH_4, N_2O and H_2O are also retrieved on the same altitude grid as N_2O_5. The initial guesses are equal to the a priori in the case of joint-fit gases as well.

The observed spectral lines are superimposed on some spectrally flat signal which arises through

both instrumental effects such as possible radiative calibration errors and atmospheric effects such as continuum emission. The gas continua caused by interaction of molecular pairs N_2-O_2 and O_2-O_2 and superposition of line wings from strong lines of H_2O and N_2O, as well as broadband continuum due to atmospheric aerosol contribute to continuum signal in the vicinity of N_2O_5. While all these continua except particle continua are modelled explicitly by KOPRA, any signature due to unknown aerosol or less than perfect modeling of the other sources of continuum emission can alter the background radiance signal (e.g., due to forward model approximations or spectroscopic uncertainities). Therefore, a purely empirical vertical profile of extinction coefficients is additionally retrieved in the IMK processing scheme in order to compensate continuum signal uncertainities described above.

The retrieval grid for continuum per spectral microwindow used consists of 60 levels with the same altitude spacing as the gases, however, continuum is forced to zero above 33 km. The initial guess continuum is always set to zero. Formally individual continuum profiles are retrieved per microwindow. In fact, through strongly constraining them in the wavenumber domain to each other, a common continuum profile for all three microwindows is retrieved. This is achieved by the continuum regularization matrix $\mathbf{R}_{cont}$. The part of $\mathbf{R}_{cont}$ that smoothes the vertical profile of continuum, $\mathbf{R}_{profile}$, is constructed using Tikhonov's first derivative operator in the altitude domain in the same manner as for trace gas abundances while the other part relates the profiles in different microwindows.

The continumm regularization $\mathbf{R}_{cont}$ for three microwindows is constructed as:

$$\mathbf{R}_{cont} = \mathbf{R}_{profile} + \alpha_{mw}^2 \begin{bmatrix} I\frac{1}{(\nu_1-\nu_0)^2} & (0) & (0) \\ (0) & I(\frac{1}{(\nu_1-\nu_0)^2}+\frac{1}{(\nu_2-\nu_1)^2}) & (0) \\ (0) & (0) & \mathbf{I}\frac{1}{(\nu_2-\nu_1)^2} \end{bmatrix},$$

where ν_i, $i = 0, 1, 2$ is the central wavenumber of the microwindows and α_{mw} is a parameter which determines the strength of the regularization. $\mathbf{I}$ is identity matrix of dimension $n \times n$ where n equals the number of vertical grids at which continuum is retrieved. The regularization parameter α_{mw} was determined to be 9.0×10^5 on the basis of test retrievals.

Test calculations justify our assumption that aerosol contributes to the residual radiance at nearly equivalent level in the three selected spectral regions. Aerosol continuum is estimated for two sulphate aerosol species containing H_2SO_4 as shown in Fig. 4.1 for maximum volume density of 0.025 $\frac{\mu m^3}{cm^3}$. While the effects of scattering of radiation along the line of sight for the selected aerosol species can be neglected, our simulation includes the scattering into the line of sight. The simulation results as shown in the difference plot (left column of Figure 1) revealed for both equatorial and midlatitude model atmospheres that continuum emissions in the spectral regions are identical. Thus MIPAS measurements contain virtually no independent information on continuum in the various analysis windows used, allowing α_{mw} to be adjusted in a way that the continuum in all the microwindows is approximately the same, following the rationale discussed above.

In order to compensate for calibration uncertainities, along with the retrieval of state parameters an altitude independent absolute radiance offset is retrieved per analysis window. The initial guess as well as a priori is zero. Unlike other elements of the state vector, no smoothing constraint is applied so that $\mathbf{R}_{offset}$ equals zero.

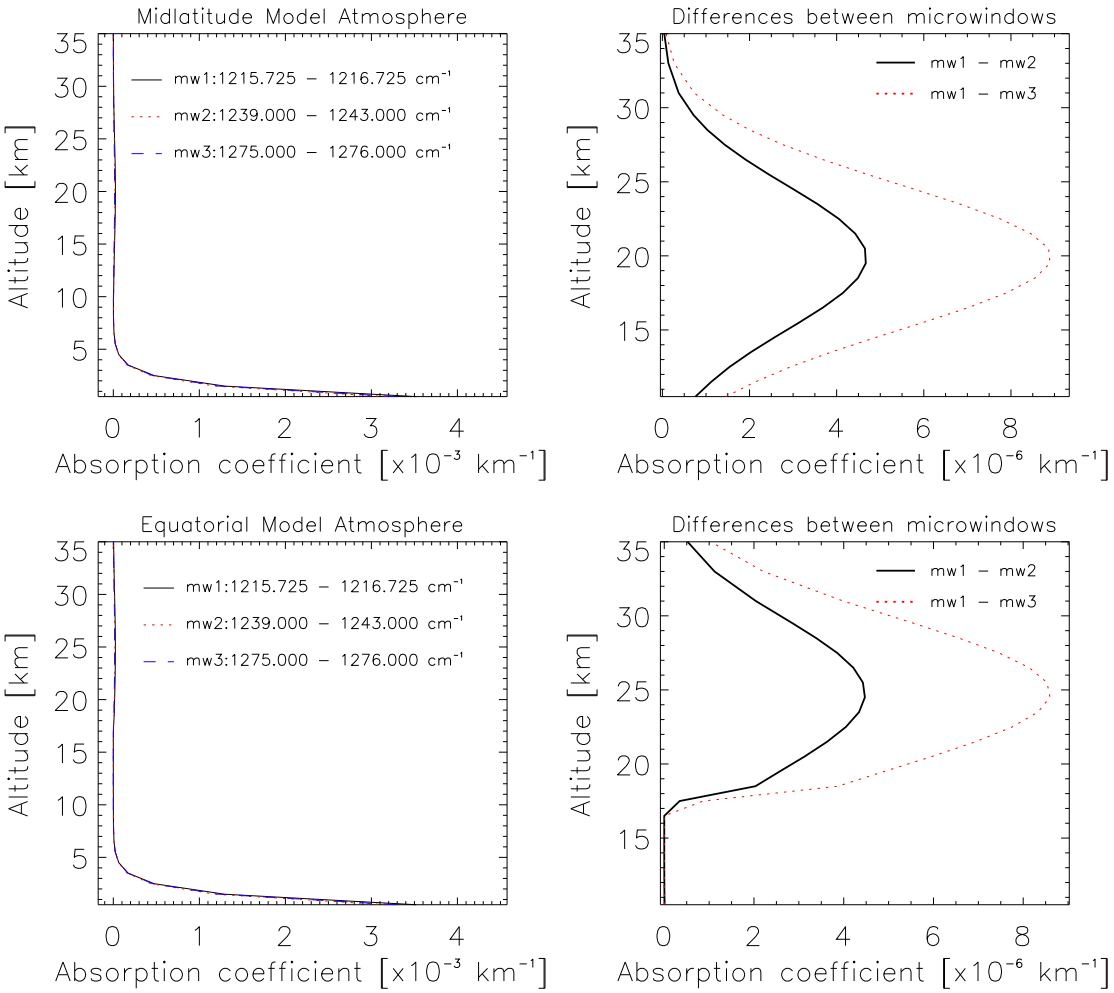

Figure 4.1: The broadband background continuum simulated for two sulphate aerosol species containing H_2SO_4 of sizes 0.04 μm and 0.68 μm for midlatitude and equatorial model atmospheres. The difference of the two microwindows in ν_{12} band of N_2O_5 from the external microwindows is hardly seen in the left panel. The right panel shows the differences which is slightly visible below 5 km and in the altitude ranges centered on 20 km and 25 km for midlatitude and equatorial atmospheres respectively.

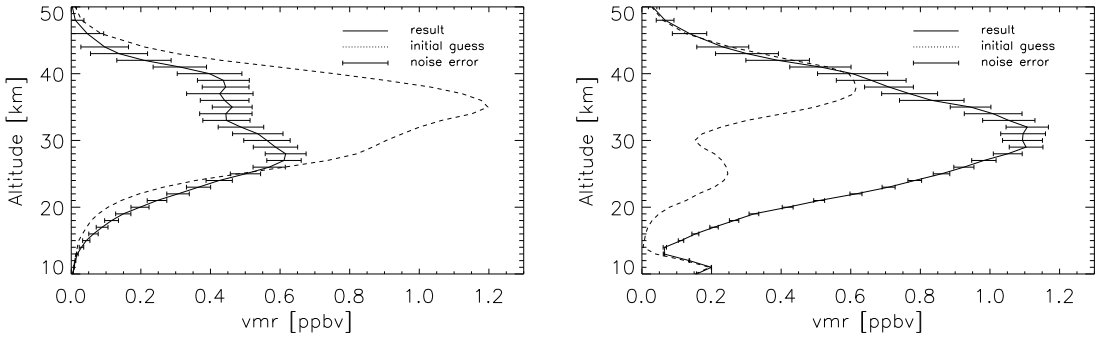

Figure 4.2: Daytime N_2O_5 profiles (solid lines) as retrieved from measurements taken when the satellite is in orbit 02994 for geolocation inside (left) and outside (right) of the southern polar vortex on September 26, 2002. The dotted line is the a priori. The error bars represent noise induced errors.

4.2 Results and Diagnostics

Fig. 4.2 shows representative daytime profiles for inside vortex (left) and outside vortex (right) derived from measurements taken when the satellite was in orbit 02994 on September 26, 2002. The initial guess for inside vortex region has a single maximum at 35 km of 1.2 ppbv. The retrieved peak VMR inside vortex is about 0.65 ppbv and shifted to lower altitude of 28 km. On the other hand, the outside vortex first guess has triple maxima at 11, 25 and 35 kms. The retrieved profile exhibits two peaks at 11 km and about 31 km. While the pronounced differences between a priori information and results prove that in general the retrievals are not overconstrained, the N_2O_5 peak at the altitude of 11 km is a mapping of a priori information onto the retrieval and thus not significant. The latter is reflected by the very low diagonal value of the averaging kernel at this altitude which is only 0.0014. In contrast, the main peak VMR near 31 km comes from information in the recorded N_2O_5 emission signal. This is reflected by the large values of the averaging kernel of 0.285 and further supported by the fact that the two daytime profiles retrieved with the peak in the a priori profiles at the same altitude have their maximum in different altitudes. The degree of freedom, $d_r = tr(A)$, of the retrieved N_2O_5 profile allowed by the smoothing constraint is 6 on average. The altitude resolution, which is the full width at half maximum (FWHM) of columns of the averaging kernel, for the ex-vortex profile is given in Fig. 4.3 (top, right panel). The vertical resolution in the altitude range near the peak VMR is only slightly larger than 3 km which is the nominal vertical resolution of a limb sounder with 3 km tangent altitude spacing. This coincides very well with the strong sensitivity of N_2O_5 signal as shown in the averaging kernel (bottom panel). Useful information can also be obtained down to an altitude of 15 km, however with degraded altitude resolution in the range of 5-9 km. The noise-induced percentage estimated standard deviation (ESD) for the ex-vortex profile is also given in Figures 3 (top, left panel). The percentage ESD is better than 5% in the altitude range of 10-35 kms while steadily rising to above 40% at 50 km. The vertical resolution is approximately equal to 3 km, the nominal vertical resolution of the instrument in the altitude range near the peak VMR. The results of linear error analysis are listed for representative retrievals inside and outside the polar vortex for nighttime measurements on September 26, 2002 in Table 1. The estimates on systematic uncertainities given in Table 1 are based on climatological variablity for interfering species, uncertainity of 1 K for temperature, gain calibration error of 1%, 15% error in linear modulation efficiency of instrumental line shape,

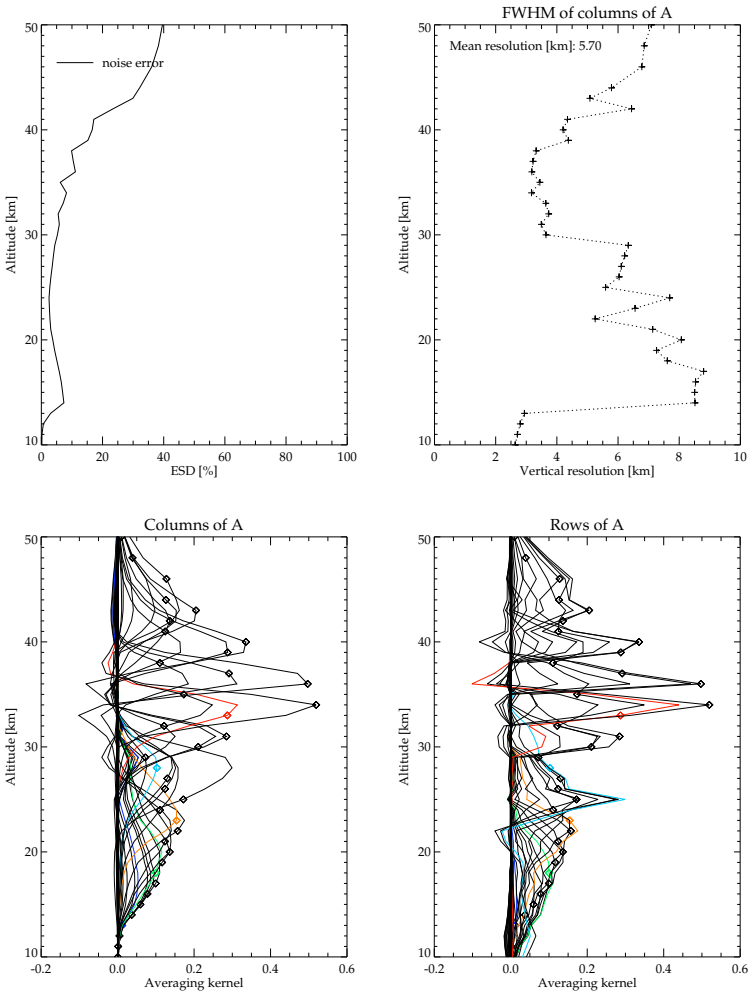

Figure 4.3: The relative random error and vertical resolution (top) and the averaging kernel(A) (bottom) corresponding to the profile outside the vortex

Altitude [*Km*]	total error	spectral noise	syst. error	Interf. gases	Temp.	Spectro. data	Point.	Spectral shift	Gain	ILS	non-LTE
15.0	19(76)	8(35)	17(68)	2(9)	1(6)	15(60)	5(20)	<1(<1)	<1(1)	2(9)	<1(2)
20.0	47(28)	20(12)	43(26)	10(6)	2(1)	40(24)	8(4)	<1(<1)	<1(<1)	7(4)	<1(<1)
25.0	71(9)	37(4)	61(7)	18(2)	7(<1)	53(6)	14(1)	<1(<1)	4(<1)	18(2)	2(<1)
30.0	150(12)	64(5)	140(11)	38(3)	20(1)	130(10)	18(1)	4(<1)	18(1)	14(1)	18(1)
35.0	230(27)	82(9)	220(26)	31(3)	59(7)	180(21)	62(7)	1(<1)	14(1)	85(10)	6(<1)
40.0	210(53)	110(27)	180(45)	32(8)	34(8)	95(23)	46(11)	1(<1)	<1(<1)	140(35)	14(3)

Altitude [*Km*]	total error	spectral noise	syst. error	Interf. gases	Temp.	Spectro. data	Point.	Spectral shift	Gain	ILS	non-LTE
15.0	34(78)	10(23)	32(74)	18(41)	1(3)	25(57)	6(15)	<1(<1)	<1(<1)	4(9)	<1(<1)
20.0	73(36)	26(13)	68(34)	38(19)	1(<1)	53(26)	13(6)	<1(<1)	<1(<1)	13(6)	<1(<1)
25.0	83(16)	43(8)	71(14)	45(8)	3(<1)	48(9)	1(<1)	1(<1)	1(<1)	26(5)	<1(<1)
30.0	140(24)	67(11)	120(21)	39(7)	20(3)	110(19)	19(3)	3(<1)	10(1)	9(1)	3(<1)
35.0	150(32)	57(12)	130(28)	38(8)	66(14)	82(17)	64(13)	2(<1)	11(2)	37(8)	3(<1)
40.0	170(42)	93(23)	140(35)	58(14)	22(5)	90(22)	20(5)	1(<1)	7(1)	84(21)	1(<1)

Table 4.1: The estimated total error, random error due to spectral noise, the total systematic error, systematic error due to interfering gases, temperature, spectroscopic data (due to uncertainity in band intensity), pointing information, residual spectral shift, gain caliberation, instrumental line shape and non-LTE for typical profiles of daytime midlatitude (top) and nighttime polar vortex (bottom) for selected altitudes for measurements on September 26, 2002. The errors are given in absolute unit [pptv] and relative unit [%] (number in bracket). The species that are assumed to interfere in retrieval spectral regions of N_2O_5 are CO_2, O_3, SO_2, NO_2, HNO_3, HOCl, H_2O_2, C_2H_2, COF_2, F14, and $ClONO_2$.

0.0005 cm^{-1} spectral shift error, tangent altitude uncertainity of 150 m, and model error estimated as a climatological difference of non-LTE and LTE forward calculations. The uncertainity of the N_2O_5 band intensity is assumed to be 5%; all uncertainities are 1σ.

The retrieved profiles of the continuum absorption coefficient decrease from about 4.0×10^{-4} km^{-1} at and below 8 km to 3.0×10^{-5} km^{-1} from 17-33 km. These are an order of magnitude lower than those simulated for the two-mode background sulphate aerosol within the framework of test calculations described in Section 3.2. This implies that the approximation of locally wavenumber-independent continuum propagates no noticeable error contribution to the N_2O_5 retrieval. These are also low compared to 1.2×10^{-3} km^{-1} at 11 km, 2.5×10^{-4} km^{-1} at 16 km and 5×10^{-5} km^{-1} at 19 km reported by *Echle et al.* [1998] for the Mt. Pinatubo aerosol. The degree of freedom for continuum is approximately 15 which slightly less than the number of tangent altitudes, due to the smoothing constraint.

Fig. 4.4 shows the measured and fitted spectra at a tangent altitude of 29 km on the left side and their difference on the right side for all three spectral intervals used. The measured spectra at this altitude is one of 16 limb sequences used to retrieve the profile shown on the right side in Fig. 4.2. The retrieval noise error at this altitude is approximately 5% (see Fig. 4.3, top left). The spectra calculated using the retrieved profile fits well with the measured spectra in all the three spectral intervals. The residual radiances lie within the range of NESR in all parts of the spectral intervals with strong signatures.

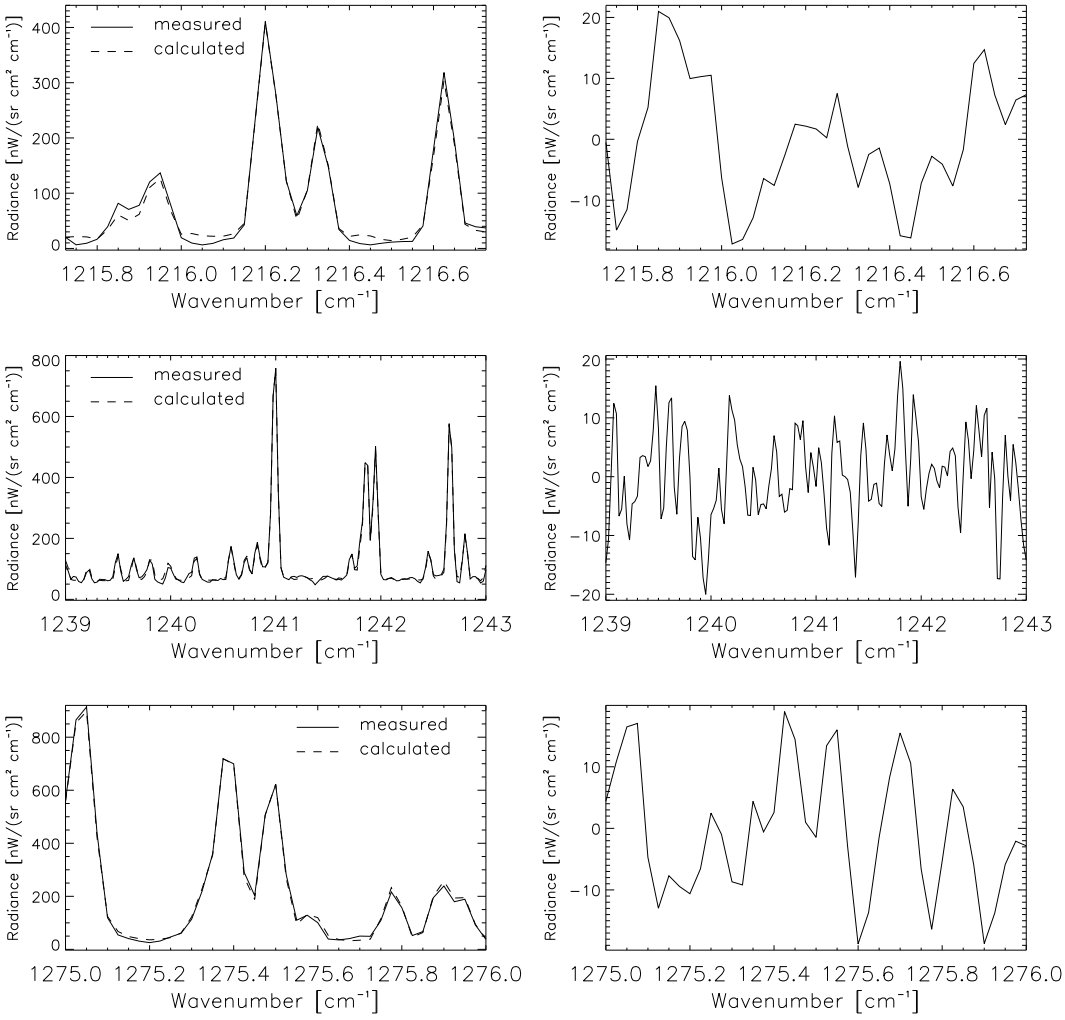

Figure 4.4: The measured and calculated spectra in all three spectral intervals for tangent altitude of 29 km. The right column represents the residual spectra (fitted spectra subtracted from measured spectra). The spectra correspond to the retrieved profile shown in Fig. 4.2 (right).

Chapter 5

Validation of MIPAS/ENVISAT NO_y, HNO_3 and N_2O_5

5.1 Brief Description of Instruments

5.1.1 MIPAS-B2 FTIR Spectrometer

MIPAS-B2 is a balloon-borne limb-emission sounder for atmospheric research. The heart of the instrument is a Fourier spectrometer that covers the mid-infrared spectral range (4 to 14 μm) and operates at cryogenic temperatures. Essential for this application is the sophisticated line of sight stabilization system, which is based on an inertial navigation system and supplemented with an additional star reference system. The major scientific benefit of the instrument is the simultaneous detection of complete trace gas families in the stratosphere, without restrictions concerning time of the day and viewing directions. Specifications, the design considerations, the actual realization and characterization of the instrument are described by *Friedl-Vallon et al.* [2004]. The nitrogen reservoir species N_2O_5 was measured the first time by MIPAS-B2 during its first flight in February 1995 [Wetzel et al., 1997].

5.1.2 MkIV Interferometer

The Jet Propulsion Laboratory (JPL) MkIV balloonborne instrument is a high resolution Fourier transform spectrometer that is operated in solar occultation mode. The MkIV uses a double-passed optical configuration for compactness and to provide passive shear compensation. Two parallel detectors, an HgCdTe photoconductor covering 650-1950 cm^{-1} and an InSb photodiode covering 1850-5650 cm^{-1}, allow the entire mid-infrared spectrum to be measured simultaneously. High signal-to-noise ratio solar occultation spectra will be measured throughout the mid-infrared region (650-5650 cm^{-1}) at high spectral resolution (0.01 cm^{-1}) at sunrise or sunset.

5.1.3 SIOUX in situ chemical instrument

The SIOUX instrument onboard M55-Geophysica aircraft is an in situ chemical instrument which is operated by German Aerospace Center (DLR). It is a 2-channel NO-O_3 chemiluminescence system. In one of the two channels, the single NO_y species are first converted into NO by the help of an Au converter heated at 300^oC with CO (0.2%) as the reduction agent. The nominal detection limit at 1 Hz sampling frequency is 15 pptv of NO_y. The accuracy of the measurement is 15% for NO_y.

5.1.4 Microwave Limb Sounder (MLS) on UARS

MLS is the first satellite experiment using limb sounding techniques at microwave frequencies. The latitudinal coverage of the MLS measurements extended from 80^o on one side of the equator to 34^o on the other due to the 57^o inclination of UARS orbit. HNO_3 is secondary MLS measurement goal. A polarization grid separates signals to different frequency radiometers (e.g. the 183-GHz radiometer for 183.310-GHz H_2O and 184.378 GHz O_3; the 205-GHz radiometer for 204.352-GHz ClO, 206.132-GHz O_3 and several weak lines of HNO_3) [*Barath et al.*, 1993].

5.2 Comparison

The selection of profiles for comparison from MIPAS/ENVISAT measurements and measurements from instruments described above are based on best temporal and spatial match. In addition, when the number of coincident measurements are large enough then quantities such as fractional difference, average of fractional difference and standard deviation of the average are calculated.

The fractional difference $D_{i,Z}$ at each altitude Z for each pair of profiles i is given as

$$\mathbf{D}_{i,Z} = \frac{2\big([\mathbf{NO_y}]_{(MIPAS/ENVISAT)} - [\mathbf{NO_y}]_{(other)}\big)_{i,Z}}{\big([\mathbf{NO_y}]_{(MIPAS/ENVISAT)} + [\mathbf{NO_y}]_{(other)}\big)_{i,Z}}. \tag{5.1}$$

The average fractional difference for N pairs of profiles is calculated as

$$\mathbf{D}_{Zave} = \frac{1}{N}\sum_{i=1}^{N}\mathbf{D}_{i,Z},$$

and the standard deviation of the mean difference σ_D is calculated as

$$\sigma_D = \sqrt{\Big(\frac{[\sum_{i=1}^{N}(\mathbf{D}_{i,Z} - \mathbf{D}_{Zave})^2]}{N(N-1)}\Big)}.$$

Comparison of measurements from instruments with substantial difference in vertical resolution requires degrading of the profiles measured by the high resolution instrument to a low resolution instrument. The transformation of this kind can be made following the approach of *Rodgers* [1990,

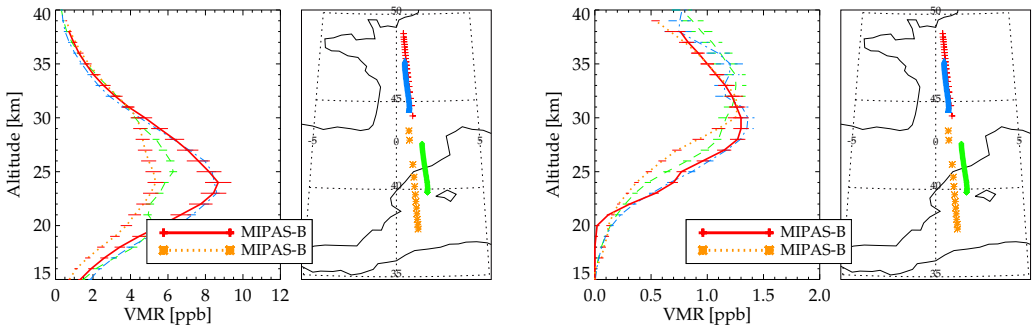

Figure 5.1: MIPAS/ENVISAT N_2O_5 (right panel) and HNO_3 (left panel) profiles in September compared with MIPAS-B2 profiles (red for Northern flight and orange for the southern flight). MIPAS/ENVISAT profiles as well as satellite tracks are indicated by green and blue colors.

2000]; *Rodgers and Connor* [2003]. The retrieved profile $\mathbf{x}$ is related to the true profile $\mathbf{x}_t$ and a priori information $\mathbf{x}_a$ used in its retrieval by

$$\mathbf{x} - \mathbf{x}_a = \mathbf{A}(\mathbf{x}_t - \mathbf{x}_a) + \sigma_{random}, \tag{5.2}$$

where σ_{random} is the square root of the diagonal elements of random noise covariance $\mathbf{S}_{random}$ and $\mathbf{A}$ is the averaging kernel. Assuming the high resolution represents quite closely the true state of the atmosphere, $\mathbf{x}_t$ can be taken as measurements from the high resolution instrument. We applied this transformation only to the in-situ SIOUX measurements which has a vertical resolution of approximately 7 m. In this circuminstance, $\mathbf{x}_t$ is the profile constructed from SIOUX measurements.

5.2.1 Comparison With MIPAS-B2

Two validation campaigns in September 24, 2002 and March 20, 2003 over Kiruna are made with MIPAS-B2. On September 24, 2002 two profiles were determined from balloon flights near 40^o N and 46^o N. The MIPAS/ENVISAT coincident measurement for flight near 46^o N covered nearly the same latitudes and longitudes along track of the flight while the flight near 40^o N is slightly different from MIPAS/ENVISAT trajectory. The March measurement was taken near 66^o N, 15^o E and covered a wide range of longitudes (greater than 10^o).

The agreements between MIPAS/ENVISAT and MIPAS-B2 HNO_3 and N_2O_5 profiles dervied from September 24, 2002 radiance measurements are very good while HNO3 profiles derived from March 20, 2003 have shown significant differences. The discrepancies in March measurements might be related to horizontal inhomogeneity within a wide range of longitudes covered by MIPAS-B2. Moreover, the measurements are made near the vortex boundary where the variation of NO_y species is highly pronounced due to difference in chemical processes on either sides of the vortex edge. The disagreements which are more pronounced for HNO_3 than N_2O_5 support the horizontal inhomogeneity as the main cause since HNO_3 exhibits stronger latitudinal gradient than N_2O_5, particularly near the vortex edge.

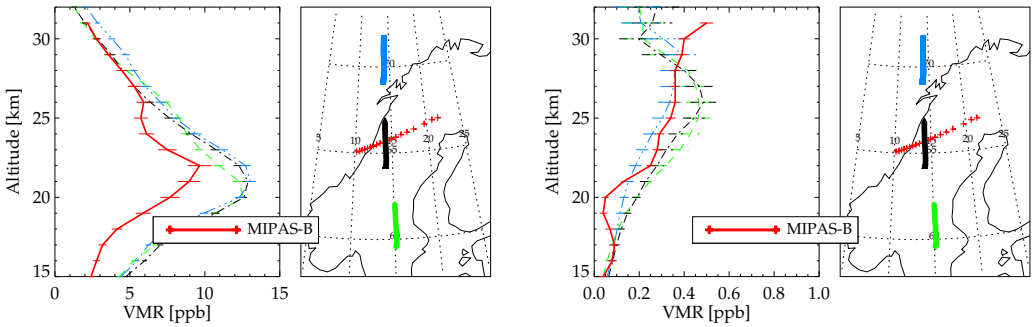

Figure 5.2: MIPAS/ENVISAT N_2O_5 (right panel) and HNO_3 (left panel) profiles in March compared with MIPAS-B2 profiles.

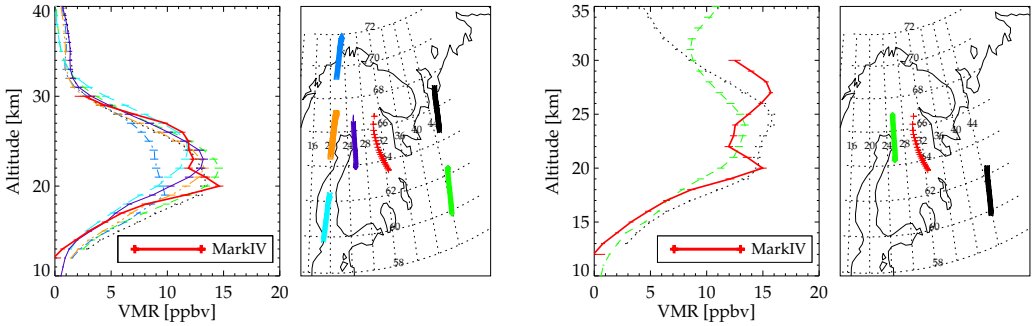

Figure 5.3: MIPAS/ENVISAT NO_y (right panel) and HNO_3 (left panel) profiles in December compared with MkIV profiles (red).

5.2.2 Comparison With MkIV

There were two sunrise measurements over Esrange, Sweden in December 16, 2002 and April 1, 2003 during SOLVE2/VINTERSOL campaigns. MkIV Balloon Interferometer detects most of NO_y species, however, comparision of species that show diurnal variations with other instruments requires normalization to the same solar zenith angle (SZA). In this work, only HNO_3 and NO_y from MkIV were compared to MIPAS/ENVISAT HNO_3 and NO_y without such adjustment. There were 6 coincident MIPAS/ENVISAT profiles corresponding to MkIV December, 16, 2002 HNO_3 and only 2 of these are available for comparison with MkIV NO_y. The comparison of the December measurements shows substantial differences since the MkIV measurements were taken near the vortex edge and NO_y is sensitive to both latitudinal and longitudinal differences in this region. As shown in Fig. 5.3, the three MIPAS measurements centered near 65^o as MkIV measurement exhibit better agreements than those profiles which are completely inside and outside (centered near 70^o and 61^o respectively) vortex. In contrast, MIPAS and MkIV April NO_y and HNO_3 measurements are in reasonable agreements due to homogeneous airmasses though there were the same level of spatial mismatch.

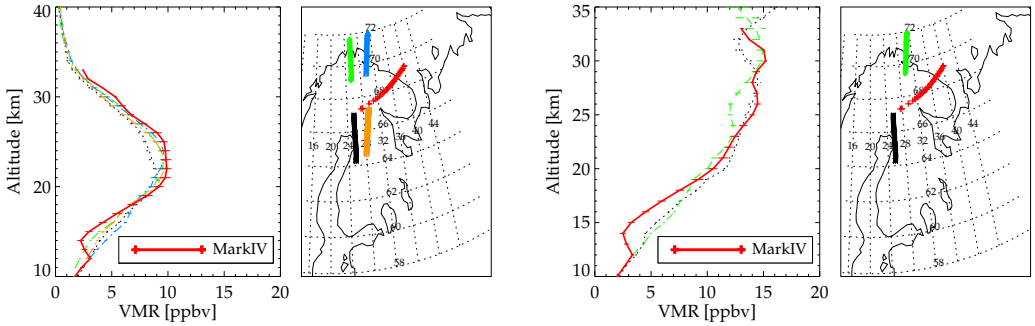

Figure 5.4: MIPAS/ENVISAT NO_y (right panel) and HNO_3 (left panel) profiles in April compared with MkIV profiles (red).

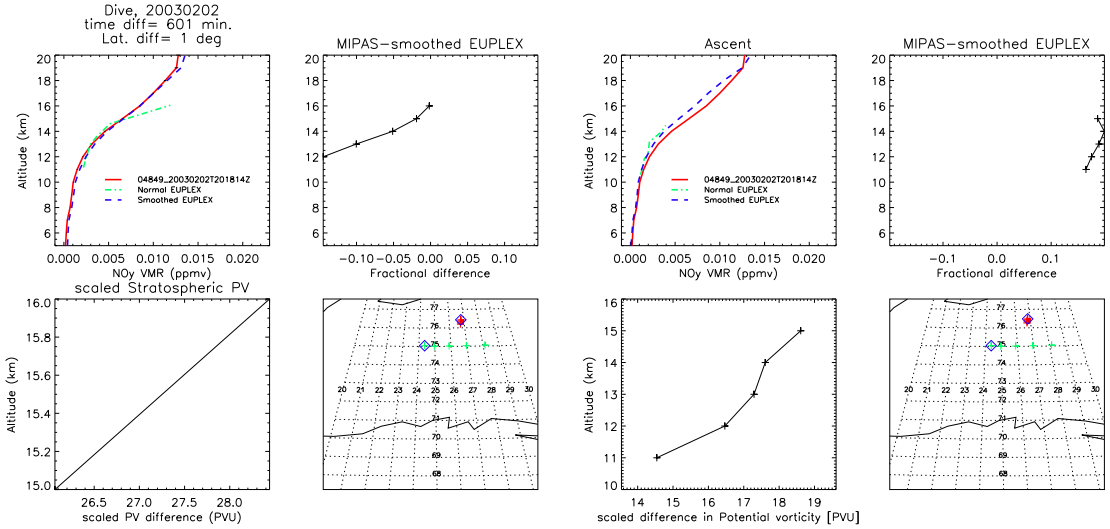

Figure 5.5: Example of MIPAS/ENVISAT profile comparison with SIOUX profiles. Left: The dive part of SIOUX NO_y compared with coincident MIPAS/ENVISAT measurement from scan 04849_20020202T201814Z. Right: The same scan compared to the ascent part of SIOUX measurements.

5.2.3 Comparison With SIOUX

M55-Geophysica aircraft flew 3 times in January, 2003 and 4 times in February, 2003, during the EUPLEX campaigns. NO_y was measured by in-situ particle counter based on the chemiluminensce technique. In a single flight the SIOUX measures NO_y during ascent, constant level and dive part of the flight. From the ascent and dive parts of the flight, profiles for an average geolocation can be derived. The main problem encountered in comparing MIPAS/ENVISAT NO_y with SIOUX is the large area covered by M55-Geophysica within a small altitude range of approximately 12 km allowing for a possible sampling of different airmasses. The dive part of the SIOUX NO_y in green and MIPAS NO_y in red (Fig. 5.5 top left panel) differ substantially above 15 km. When SIOUX NO_y is degraded by the averaging kernel of SIOUX NO_y according to (5.2) (see black dash line in the same figure), however, the agreement has improved dramatically to better than 5% of the mean VMR above this altitude. The differences at altitudes lower than this

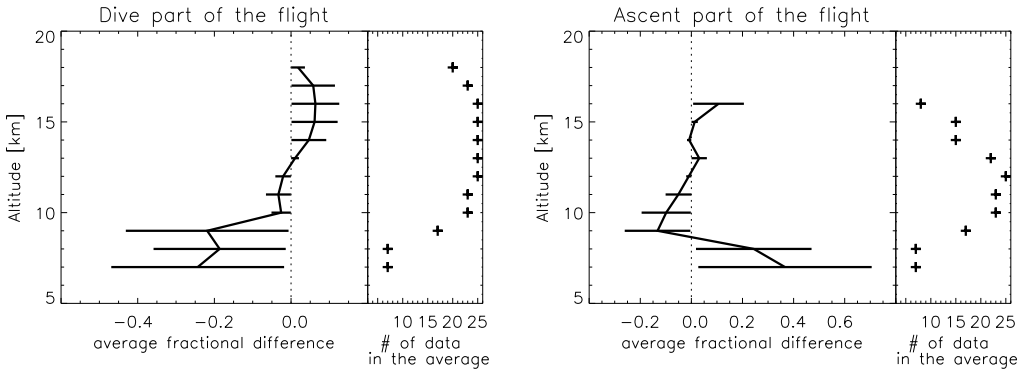

Figure 5.6: MIPAS/ENVISAT-SIOUX average fractional difference profile comparison. The dive part (left) and ascent part (right) along with the number of data points used for the calculation of average and standard deviation of the average fractional difference.

altitude have not shown significant improvements, instead, the differences became more apparent (second column, top panel). Nevertheless, these differences are very small in absolute units due to low VMR there. Likewise, agreements between ascent part of SIOUX NO_y and MIPAS NO_y have improved following smoothing of SIOUX NO_y by MIPAS NO_y averaging kernel. The differences between the two measurements for the ascent part of SIOUX measurements increase with increasing differences in PV suggesting the remaining discrepancy, after smoothing is applied, is attributable to airmass inhomogeneity (see bottom panel, third column).

In Fig. 5.6, the average fractional difference profile remained near the zero line in general. Moreover, the mean standard deviation include the unbiased line (zero line) as shown by error bars for altitude higher than 10 km. In general, NO_y from SIOUX on M55-Geophysica during EUPLEX campaigns in January and February, 2003 agree within average difference of less than 10% between 10-18 km. Scarcity of good coincidence in space and horizontal inhomogeneity, that could arise due to a wider range of longitude sampled by SIOUX measurements, might have contributed to much of the observed differences.

Not all fractional differences are meaningful since in some cases the MIPAS/ENVISAT NO_y averaging kernels are limted to altitude higher than shown in the comparison. The fractional differences below altitude indicated by averaging kernels is then the difference between a priori profiles and the SIOUX profiles which come from climatology. Two extreme examples of averaging kernels are shown in Fig. 5.7.

5.2.4 Comparison of MIPAS HNO_3 with MLS HNO_3 climatology

We made comparison of MIPAS HNO_3 with the Microwave Limb Sounder (MLS) onboard the Upper Atmosphere Research Satellite (UARS) HNO_3 climatology in order to assess whether MIPAS HNO_3 lies within the limit of scatter of MLS HNO_3 over the 8-year period.

The UARS MLS HNO_3 data set is by far the complete observational record which includes the global distribution of stratospheric HNO_3 over annual cycles for much of the 1990s. This data set was examined previously by *Santee et al.* [1999] and very recently some of the limitations in that

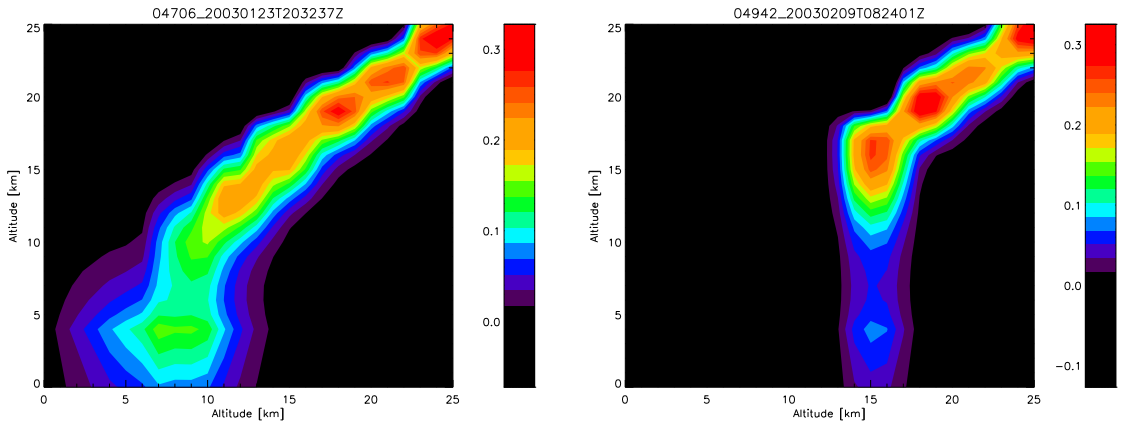

Figure 5.7: MIPAS/ENVISAT averaging kernels (left: information comes from measurements down to 7 km) and (right: information comes from measurements only above 15 km).

study were removed by the use of version 6 data set and calculation of zonal mean using equivalent latitude data bins [*Santee et al.*, 2004].

Santee et al. [2004] have made averages from 5^o equivalent latitude bands which were used to look at interannual and interhemispheric differences in the HNO_3 seasonal cycle for seven years at 585 K. MIPAS HNO_3 at the same theta level, which are averages of 4^o equivalent latitude band for the periods in September/October, 2002 are compared with MLS HNO_3 of September period. The MLS HNO_3 climatology at 585 K shows that Southeren hemisphere HNO_3 in the region South of 75^o is approximately 4.0 ppbv averaged over the 1991-98 period. The MIPAS HNO_3 for the same equivalent latitude band in Fig. 6.3 exhibits the same value of 4.0 ppbv. The MIPAS HNO_3 near the vortex edge region (55-60^o) increases to a value over 9 ppbv while MLS HNO_3 varies between 8-12 ppbv showing annual variation. The values agree within the uncertainity of 2 ppbv of MLS HNO_3.

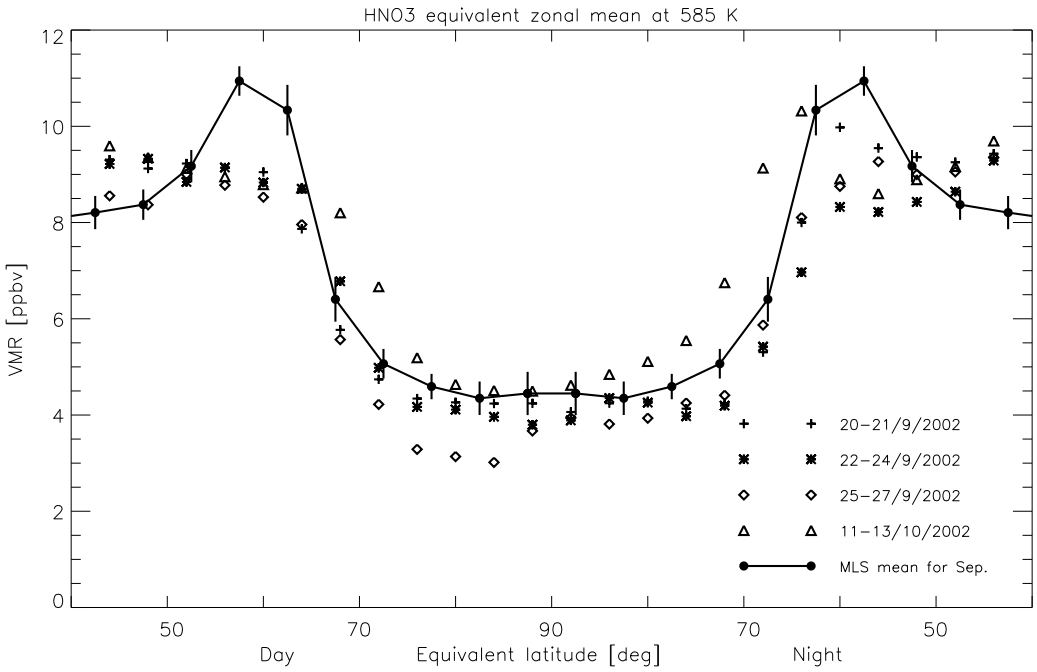

Figure 5.8: HNO_3 on 585 K level to facilitate comparison with MLS HNO_3 Climatology. The zonal mean is calculated from data binned in to 4^o equivalent latitude.

Chapter 6

NOy in the Austral Spring 2002

The Antarctic polar vortex split in September/October is an unusual event which was reasonably well covered during its evolution by MIPAS measurements. The large data set was used to retrieve the volume mixing ratios of reactive nitrogen compounds (NO_y), and the source gases CFC-11, N_2O and CH_4. In this chapter, the implication of major warming on N_2O_5 VMR, the NO_y budget and its partitioning as well as denitrification and mixing in the lower and middle stratosphere are studied for four periods: early presplit period (20-21 September), presplit period (22-24 September), split period (25-27 September), and early mid-October (postsplit, 11-13 October). The time categories are fairly reasonable and justifiable owing to the different dynamics and conditions for chemical processing at these times. Mixing processes during the event have been investigated using source gases and ozone distributions [*Glatthor et al.*, 2004]. Examination of possible isentropic mixing has indicated that mixing points or clusters instead of mixing lines were observed. As noted in that paper, $[CH_4]$:$[N_2O]$ relations inside the vortex are more linear for N_2O between 50 and 300 ppbv, from which relatively straight lines can be obtained over a wide range of theta levels. Quantification of mixing-induced deficit in NO_y from such 'mixing lines' leads to overestimation of the deficit due to mixing. On the other hand, the accuracy of the artificial-reference tracer method is limited if the number of long-lived species used in its construction is not high enough. We therefore consider both mixing line approach and constructing artificial 'reference tracer' to distinguish mixing-induced changes from the contribution of denitrification to the observed NO_y deficit inside the polar vortex and compare the results.

6.1 Data

6.1.1 MIPAS NO_y and Long-lived Species

The volume mixing ratios of NO_y, CH_4, CFC-11 and N_2O used for this study were derived from infrared limb spectral radiances observed by MIPAS on board of ENVISAT during a period of eleven days from September 20 to October 13, 2002. Data are missing between September 28 and October 10 due to MIPAS switch off resulting from a failure of the stirling cooler.

The NO_y compounds retrieved from the limb emission radiances are HNO_3, $ClONO_2$, N_2O_5, NO

No.	Microwindow [cm^{-1}]	Height occupation 5-56 km in 3km steps
1	861.575 - 864.550	= = = T T = = = = T T T T = T = T =
2	865.225 - 868.200	= = T T T T T = T T T T T = T = T =
3	865.225 - 868.200	= = T = = = T T T T T T T = T = T =
4	871.225 - 873.975	= T = = = = T T T T T T T = T = T =
5	877.075 - 877.425	= = T T T T T T = T T T T = T = T =
6	878.375 - 881.350	T T = T T = = = T T T T T = T = T =
7	881.625 - 884.600	= T T = = = = T T T T T T = T = T =

Table 6.1: Occapation matrix used for joint retrieval of HNO_3 and O_3. The columns represent from left to right: the microwindow number, the microwindow and the height at which it is used (label "T" indicates the microwindow is used at the given height begining with 5 km (left corner of the column) and 56 km (right corner of the column).

and NO_2. Mixing ratios of the long-lived species CFC-11, N_2O and CH_4 were taken from *Glatthor et al.* [2004]. The N_2O_5 profiles are retrieved as described in previous chapter. NO and NO_2 were retrieved as reported by *Funke et al.* [2003] and $ClONO_2$ was retrieved as reported by *Höpfner et al.* [2004].

HNO_3 was retrieved jointly with ozone using optimized spectral regions with respect to total retrieval error [*von Clarmann and Echle*, 1998] in its ν_5 and $2\nu_9$ bands. Not all selected spectral regions are used for all observation geometries in order to optimize computation time and minimize systematic errors. Therefore, height dependent combinations of microwindows (so-called occupation matrices) are selected with a trade-off between computation time and total retrieval error [*Echle et al.*, 2000] as listed in Table 6.1. For the MIPAS spectroscopic database, the HNO_3 band intensity is scaled by a factor of 0.879 (Flaud et al., pers. communication) with respect to the HITRAN database [*Rothman et al.*, 1998] which led to an average of 12% increase in HNO_3 VMR.

6.1.2 Potential Vorticity and related Quantity derived from Meteorological Data

For the assessment of mixing through the vortex boundary an appropriate definition of the edge of the polar vortex is needed. Very often, the vortex edge is defined as the maximum meridional gradient of a conserved tracer. A tracer, such as potential vorticity (PV), may not be a monotonic function of geographical latitudes particularly during the perturbed atmosphere, e.g. during major warming. Under such circumstances, appropriate transformation is required such that the tracer is a monotonic function of the transformed quantity. Since PV is used as a dynamical tracer, mapping of PV values into their equivalent latitudes is made by comparing the areas enclosed by the isolines of PV with those enclosed by the latitudinal circles. Applying the procedure described by *Nash et al.* [1996] can then give a reasonably accurate vortex edge. Specifically, the equivalent latitude of the vortex edge can be obtained by the maximum of the average wind multiplied by PV. After having determined the equivalent latitudes from the potential vorticity derived from United Kingdom Meteorological Office (METO) assimilated winds, this method is used to mark the vortex edge (see Figs. 6.1-6.2 for the vortex edge averaged over the days in the respective period). The vortex edge region is refered to as a wide area enclosed by $\pm$5 degree equivalent latitude from the edge.

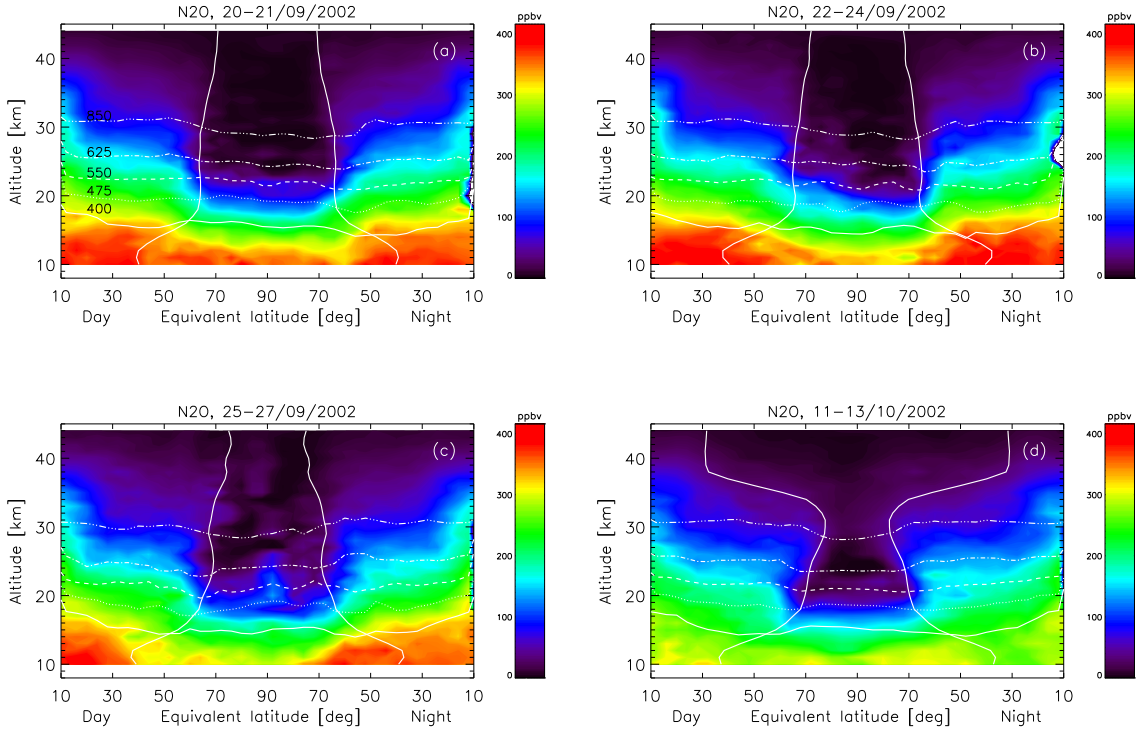

Figure 6.1: N_2O as a function of equivalent latitudes. The vortex edge is overlaid by white solid line extending along the altitude axis and a wide vortex edge region is assumed to lie within 5 degree equivalent latitude width from the edge in either sides. White lines indicate potential temperature levels of 400 (solid), 475, 550, 625, 850 K (dash-dot-dot).

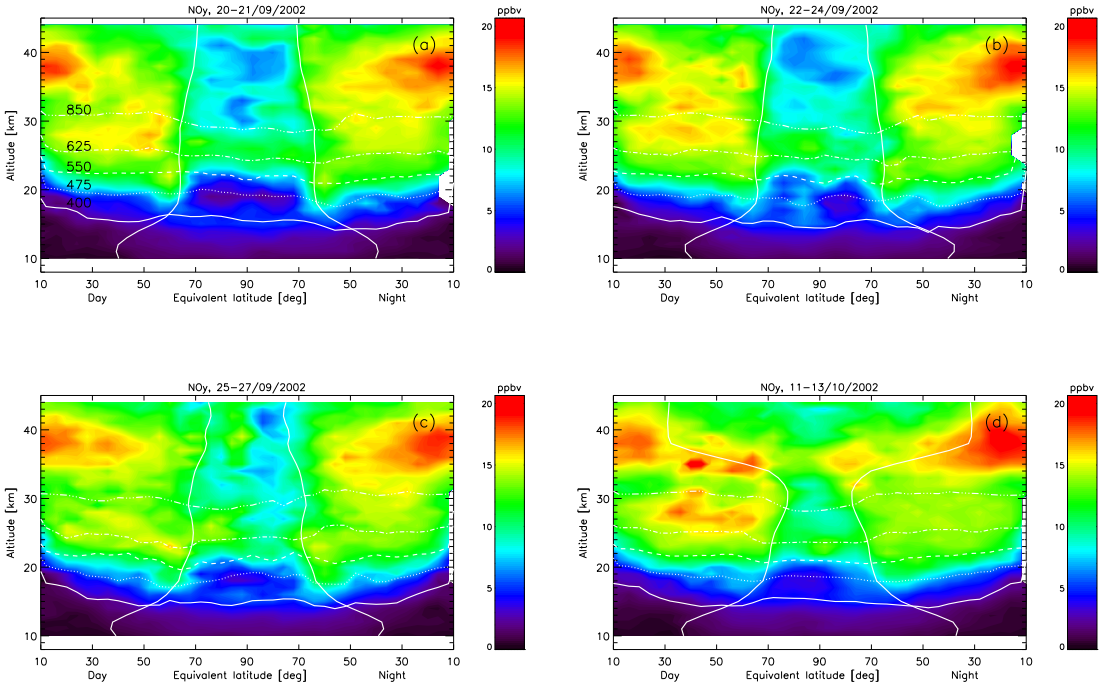

Figure 6.2: NO_y as a function of equivalent latitudes. The vortex edge is overlaid by white solid line extending along the altitude axis and a wide vortex edge region is assumed to lie within 5 degree equivalent latitude width from the edge in either sides. White lines indicate potential temperature levels of 400 (solid), 475, 550, 625, 850 K (dash-dot-dot).

Nighttime midlatitude

Altitude [Km]	Total error	Spectral noise	Syst. error	Interf. gases	Temp.	Spectro. data	LOS	Spectral shift	Gain calib.	ILS	Forward model
10	77(56)	27(19)	72(53)	3(2)	<1(<1)	68(50)	4(2)	<1(<1)	3(2)	23(16)	<1(<1)
15	110(7)	49(3)	95(6)	12(<1)	17(1)	86(5)	20(1)	<1(<1)	18(1)	22(1)	2(<1)
20	380(6)	200(3)	330(5)	85(1)	18(<1)	170(3)	100(1)	16(<1)	110(1)	210(3)	8(<1)
25	680(6)	290(2)	610(6)	14(<1)	262(2)	140(1)	38(<1)	33(<1)	180(1)	500(5)	13(<1)
30	790(11)	190(2)	770(11)	7(<1)	270(4)	310(4)	300(4)	2(<1)	140(2)	560(8)	44(<1)
35	630(37)	81(4)	630(37)	7(<1)	170(10)	480(28)	340(20)	<1(<1)	69(4)	98(5)	<1(<1)
40	150(50)	37(12)	150(50)	1(<1)	33(11)	110(36)	91(30)	<1(<1)	15(5)	22(7)	6(2)
44	63(53)	19(16)	60(50)	<1(<1)	13(11)	45(38)	37(31)	<1(<1)	5(5)	9(8)	2(2)

Nighttime polar vortex

Altitude [Km]	Total error	Spectral noise	Syst. error	Interf. gases	Temp.	Spectro. data	Point.	Spectral shift	Gain calib.	ILS	Forward model
10	54(7)	28(3)	46(6)	2(<1)	15(2)	42(5)	5(<1)	<1(<1)	12(1)	1(<1)	1(<1)
15	81(3)	55(2)	59(2)	5(<1)	32(1)	24(1)	2(<1)	<1(<1)	37(1)	22(<1)	4(<1)
20	390(16)	180(7)	350(15)	56(2)	77(3)	310(13)	3(<1)	4(<1)	44(1)	130(5)	5(<1)
25	310(7)	250(6)	180(4)	9(<1)	51(1)	47(1)	42(1)	5(<1)	42(1)	150(3)	6(<1)
30	250(24)	170(16)	190(18)	6(<1)	52(5)	57(5)	94(9)	5(<1)	28(2)	140(13)	26(2)
35	110(27)	48(11)	100(24)	5(1)	16(3)	84(20)	53(13)	<1(<1)	11(2)	9(2)	6(1)
40	50(40)	34(27)	37(29)	1(1)	5(4)	31(24)	18(14)	<1(<1)	4(3)	5(4)	<1(<1)
44	24(58)	18(43)	16(38)	<1(1)	2(5)	13(31)	7(18)	<1(<1)	1(4)	2(6)	<1(<1)

Table 6.2: The estimated total error, random error due to spectral noise, the total systematic error, systematic error due to interfering gases, temperature, spectroscopic data (due to uncertainity in band intensity and half line width), line of sight (LOS), residual spectral shift, gain caliberation, instrumental line shape and forward model for typical profiles of nighttime midlatitude (top) and nighttime polar vortex (bottom) for selected altitudes for measurements on September 26, 2002. The errors are given in absolute unit [pptv] and relative unit [%] (number in bracket). The species that are assumed to interfere in the microwindows selected for HNO_3 retrieval are H_2O, CO_2, O_3, NO_2, N_2O, CH_4, C_2H_6, CFC-11, CFC-12, ClO, OCS and NH_3.

The analysis of daytime and nighttime NO_y partitioning is separately based on average of data within the same airmass as well as individual data points. The latter may help understanding finer details that could be smoothed out in the mean values. Understanding of the zonal mean values of geographic latitudes may not be straightforward due to the large geographical as well as dynamical latitude range covered by the vortex during the course of the observation time, particularly when comparing averages from different periods. The equivalent latitude zonal mean gives a much more representative view of the behaviour of NO_y and its constituents in the context of stratospheric flow and vortex evolution than the usual zonal mean from geographic latitudes, particularly during the major warming.

6.1.3 Error Estimation for NO_y

The random retrieval noise error and systematic errors due to the uncertain parameters are available from the original papers [*Glatthor et al.*, 2004; *Höpfner et al.*, 2004; *Funke et al.*, 2003] and in Chapter 4 for N_2O_5, which are determined for each constituent species according to linear error analysis. The random retrieval noise error and systematic errors of HNO_3 for representative nighttime inside polar vortex and midlatitude retrievals for measurements on September 26, 2002 are tabulated in Table 2.

The random retrieval noise error and systematic errors of NO_y are determined from the estimated errors of its components. The total systematic error of the constituent species includes the uncertainities from all interfering gases which are not jointly retrieved with the constituent gas and uncertainities from temperature, line of sight, instrumental line shape, spectral shift, calibration

Nighttime midlatitude

Altitude [Km]	Total error	Spectral noise	Syst. error	Interf. gases	Temp.	Spectro. data	LOS	Spectral shift	Gain calib.	ILS	Forward model
10	101(29)	22(6)	79(23)	2(<1)	9(2)	46(13)	3(1)	<1(<1)	6(1)	9(2)	<1(<1)
15	269(12)	56(2)	212(9)	8(<1)	41(1)	94(4)	19(<1)	<1(<1)	26(1)	19(<1)	1(<1)
20	799(11)	183(2)	615(8)	73(1)	17(<1)	158(2)	84(1)	13(<1)	90(1)	170(2)	7(<1)
25	1229(8)	274(1)	954(6)	17(<1)	178(1)	151(1)	35(<1)	25(<1)	133(<1)	404(2)	8(<1)
30	1674(11)	315(2)	1359(9)	69(<1)	180(1)	245(1)	166(1)	15(<1)	84(<1)	576(4)	21(<1)
35	2206(19)	694(6)	1511(13)	64(<1)	274(2)	810(7)	257(2)	22(<1)	53(<1)	29(<1)	<1(<1)
40	1526(19)	449(5)	1077(13)	5(<1)	112(1)	362(4)	89(1)	36(<1)	73(<1)	397(4)	<1(<1)
44	1360(18)	204(2)	1155(16)	4(<1)	163(2)	333(4)	52(<1)	2(<1)	89(1)	509(7)	<1<1)

Nighttime polar vortex

Altitude [Km]	Total error	Spectral noise	Syst. error	Interf. gases	Temp.	Spectro. data	Point.	Spectral shift	Gain calib.	ILS	Forward model
10	162(15)	33(3)	129(12)	2(<1)	16(1)	36(3)	6(<1)	1(<1)	8(<1)	56(5)	1(<1)
15	489(13)	99(2)	390(10)	6(<1)	42(1)	45(1)	13(<1)	3(<1)	24(<1)	251(6)	3(<1)
20	766(16)	169(3)	596(12)	33(<1)	58(1)	233(4)	10(<1)	9(<1)	28(<1)	215(4)	6(<1)
25	937(8)	312(2)	625(5)	25(<1)	89(<1)	152(1)	25(<1)	57(<1)	75(<1)	134(1)	65(<1)
30	2455(27)	282(3)	2173(24)	112(1)	198(2)	1127(12)	127(1)	4(<1)	66(<1)	501(5)	35(<1)
35	1942(26)	208(2)	1734(24)	62(<1)	169(2)	1039(14)	58(<1)	29(<1)	107(1)	208(2)	59(<1)
40	2140(21)	250(2)	1890(18)	12(<1)	229(2)	604(5)	32(<1)	26(<1)	114(1)	592(5)	276(2)
44	2566(32)	220(2)	2345(29)	8(<1)	301(3)	552(6)	218(2)	4(<1)	118(1)	651(8)	490(6)

Table 6.3: The same as Table 6.2, but for NO_y.

uncertainity, forward modelling and spectroscopic errors.

The random noise error and uncertainity in spectroscopic data in NO_y are considered as random errors among all NO_y components and determined by adding VMR weighted individual values of the constituent species quadratically. All the remaining components are assumed to be systematic among all NO_y components and estimated from VMR weighted linear sum. The estimates determined in this manner for the same representative geolocations as HNO_3 are listed in Table 3.

6.2 Vortex as observed from evolution of NO_y and N_2O

The vortex was approximately centred on the pole in the early-presplit period of MIPAS measurements, and shifted towards lower latitudes during the presplit period. During the split period, MIPAS observed airmasses at high-latitudes South of 80^oS above 475 K that originated from lower latitude, as shown in Figs. 6.3-6.4. MIPAS sampled ex-vortex air of mid-latitude origin even in the presplit periods at and above 475 K levels at these latitudes suggesting that the vortex has weakened in the region connecting the two vortices evolving from the strong pole-centered vortex prior to the major warming. In the early mid-October, the vortex recentred on the pole.

The size of the vortex prior to the split and in split periods was large and remained nearly constant at a radius of approximately 30^o as inferred from equivalent latitude of the vortex edge in contrast to its radius which decreased with altitude from about 25^o at 400 K to 12^o at 850 K (see Figs. 6.3-6.4) in the postsplit period. The shrinkage in size determined from equivalent latitude of PV fields is in good agreement with that implied by the strong chemical tracer gradients of N_2O and NO_y at the vortex edge shown in Figs. 6.1-6.2. The weakening of the PV gradient and the weaker vortex barrier above 33 km in the postsplit is also captured by the equivalent zonal mean of N_2O and NO_y since comparable values are observed across the edge.

The change in vortex size and position over the course of the study period implies that the vortex airmass was subject to different underlying meteorological conditions characteristic to the lati-

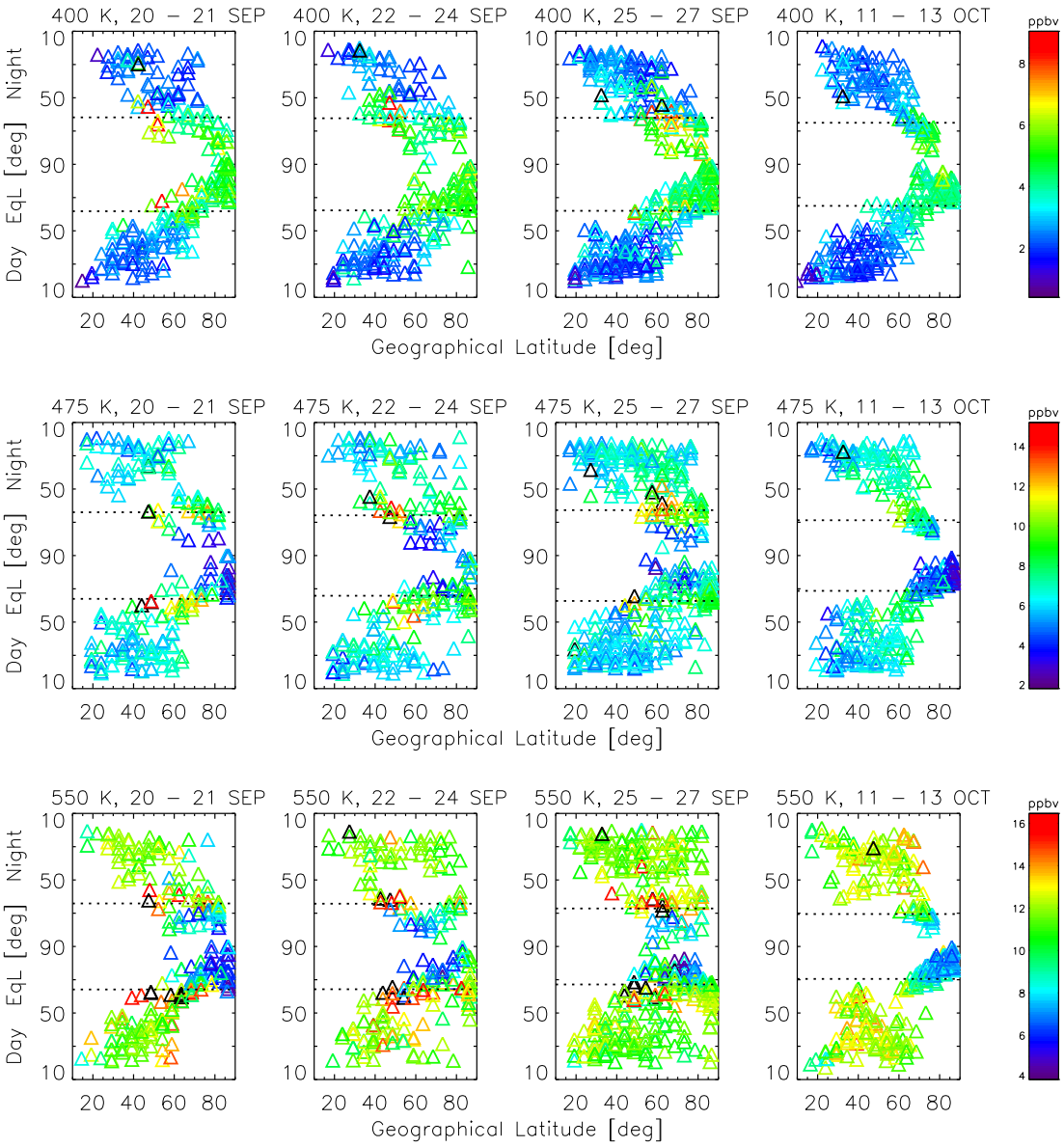

Figure 6.3: The evolution vortex position and size as seen from NO_y VMR, geographic latitudes and equivalent latitudes at a potential temperature of 400 K (top), 475 K (middle) and 550 K (bottom) for the periods indicated at the top of each panel. The dotted horizontal lines represent the vortex edge barrier on the day and night sides of the vortex.

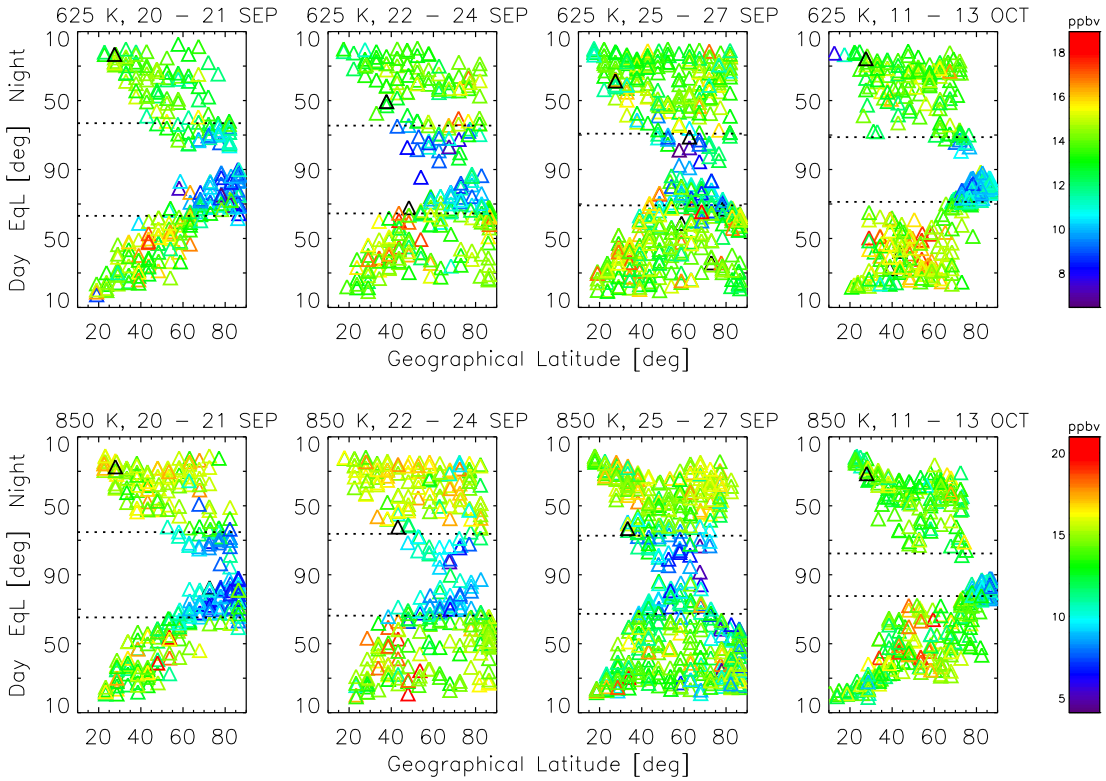

Figure 6.4: the same as Fig. 6.3 at a potential temperature of 625 and 850 K.

tudes. The geographic latitudes of the vortex airmass, for instance, cover 60-90^o, 55-85^o, 45-80^o and 65-90^o in early presplit, presplit, split phases and early mid-October, respectively, at 550 K. There is a variation in the latitudes of vortex airmass with altitude which is prounounced during the split period, e.g. from 45-80^{o}S at 550 K to 40-70^{o}S at 850 K. This indicates that the chemical processes governing the partitioning inside the vortex during these periods have taken place under different conditions, e.g. the photochemistry which is particularly important. Therefore, our analysis of NO_y partitioning treats individual data points as well as equivalent latitude zonal mean.

6.3 Stratospheric N_2O_5: Application to the major warming event

In the following, we discuss the retrieved N_2O_5 VMR in the context of an unprecedented Antarctic major warming. Altitude-latitude cross-sections of N_2O_5 VMR measured on 21-22 and 26 September, and 13 October are shown in Fig. 6.5 as examples of three typical situations during the vortex split event. On 21 September, the very low VMR between day (left of 90^{o}S) and night (right of 90^{o}S) cross-sections of the orbit indicates that the vortex was slightly displaced away from the pole with its center close to 80^{o}S. On 22 September, a sharp buildup of N_2O_5 VMR was observed for nighttime observations. There was also a buildup for daytime observations though not as distinct as that seen in nighttime observations. On 26 September, the vortex was displaced farther away close to 65^{o}S on the day side of the hemisphere and 50^{o}S on the night side with very high VMR over the pole both on the day and night side of the hemisphere. These features are

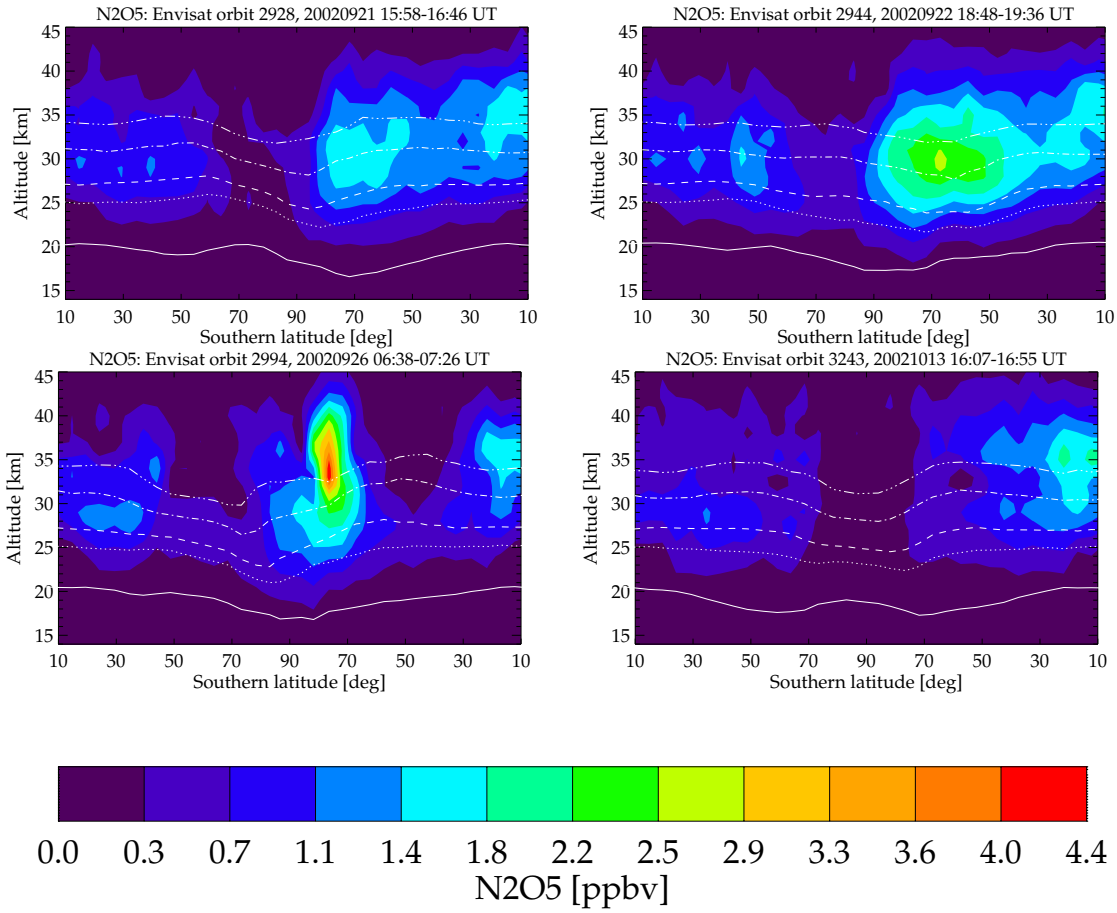

Figure 6.5: VMR along the orbit track on September 21, 22, 26 and October 13. The first row represents conditions during the presplit vortex while the second row denotes that of a split and postsplit of the vortex. Left of 90^o is the daytime (descending) and right of 90^o is the nighttime (ascending) part of the orbit. White lines indicate potential temperature levels of 625 (solid), 700, 850, 1000, 1200 K (dash-dot-dot).

further exhibited in the polar orthographic projections given in Fig. 6.6 for all orbits on selected observation days. This indicates the surge of midlatitude airmasses in between the two fragments of the vortex. Exceptionally high N_2O_5 VMR of up to 4.4 ppbv was observed at high latitudes beginning 22 September, after the vortex was fully displaced from the pole, and lasted throughout the split period. This enhancement can be seen from both Fig. 6.5 (in the range of 850-1200 K for single orbit) and Fig. 6.6 at 850 K for all the orbits. On 13 October, the vortex is reestablished and showed better symmetry with respect to the pole than at the beginning of the investigation period as seen from very low N_2O_5 concentrations.

The day-night asymmetry expected from the known chemistry of N_2O_5 is clearly exhibited in Fig. 6.5. The nighttime values on the right side of 90^oS differ from the daytime measurements by 1-3 ppbv at the peak altitude of N_2O_5 VMR around 35 km.

Due to the orbital geometry of ENVISAT and the equinox conditions during the measurement period, the variation of SZA over the period of the observations is more of a reflection of the vari-

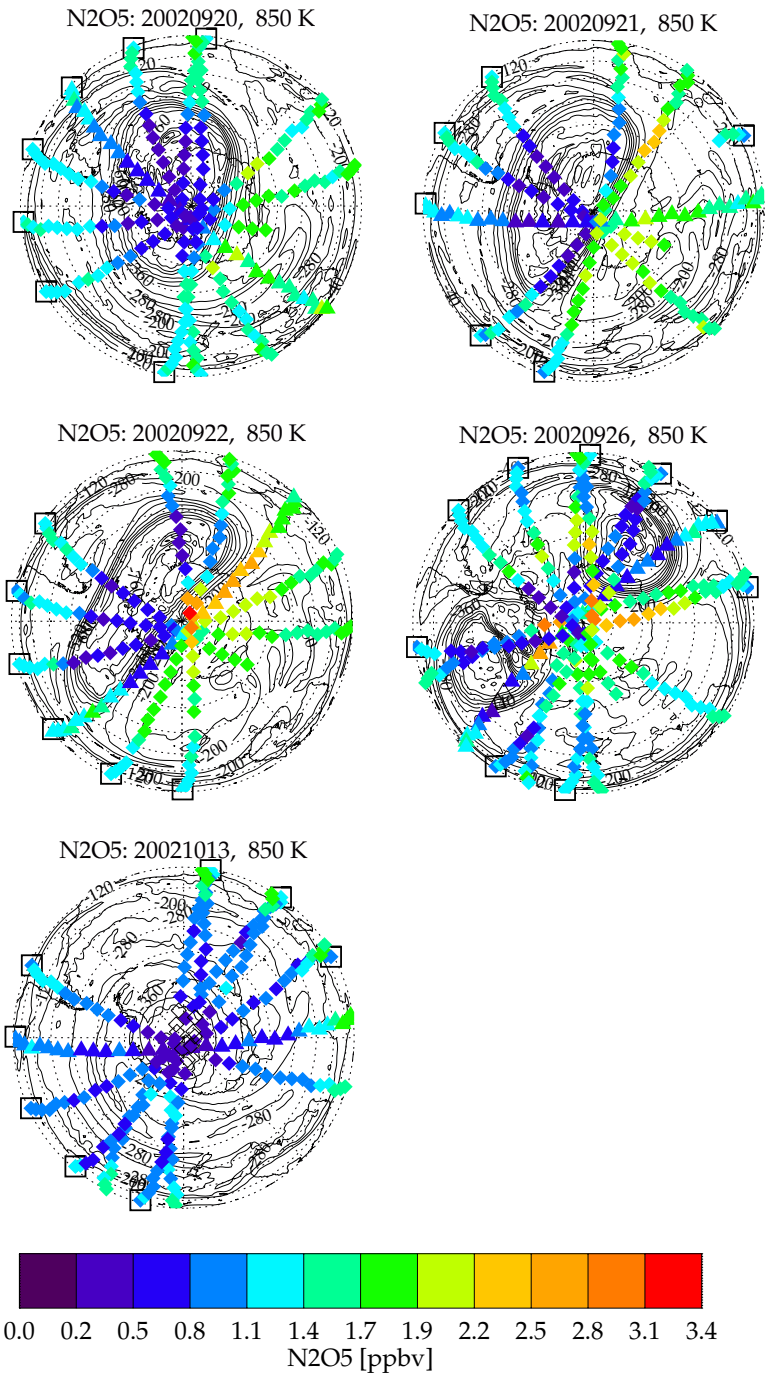

Figure 6.6: N_2O_5 distributions on 850 K level of potential temperature. The measurements during 20-22 September, 2002 represent presplit of the vortex while that during 26 September and 13 October, 2002 represent split and postsplit periods in this order. The underlying contour lines show potential vorticity. Symbols enclosed by boxes mark the beginning of each orbit on the dayside.

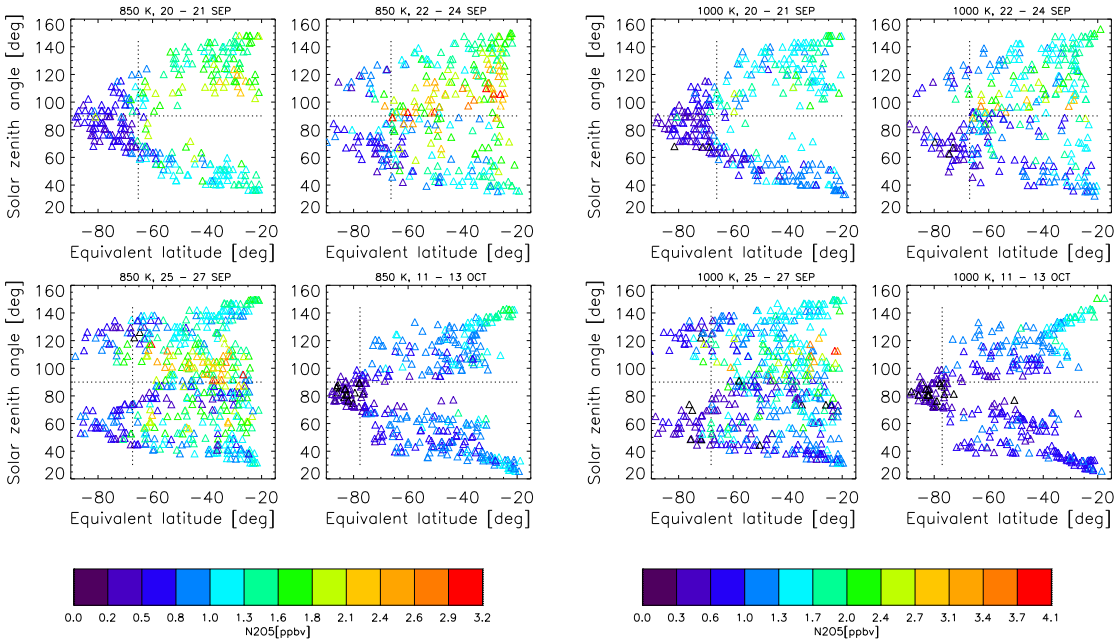

Figure 6.7: The solar zenith angle dependence of N_2O_5 VMR as a function of equivalent latitudes at a potential temperature of 850 K (left) and 1000 K (right). The dotted vertical and horizontal lines represent the vortex edge and SZA=90^o respectively. The vortex edge is determined according to *Nash et al.* [1996] using METO analysis data and averaged over the number of days in the respective periods.

ation of geographic latitudes than of the local observation time (note that there are only two local observation times corresponding to day and nighttimes as described in section 2.2 of Chapter 2).

The SZA-equivalent latitude cross-sections of N_2O_5 VMR at 850 and 1000 K potential temperature levels in Fig. 6.7 show the day-night asmmetry in N_2O_5 concentrations for all individual measurement locations of all observation days separated into four periods. They characterize the early presplit, presplit, split and postsplit situations. MIPAS sampled the vortex airmass within SZA ranging from 70^o to 120^o, 65^o to 125^o, 50^o to 130^o, and 65^o to 100^o in early presplit, presplit, split and early mid-October respectively. Quantitative comparison of N_2O_5 evolution during these periods is not straightforward due to different SZAs sampled (see Fig. 6.7 and Fig. 6.8 (left panel)) in addition to difference in day length between September and October. The latter led to a significant decrease of VMR in the vortex and ex-vortex regions from September to early mid-October.

The distribution of SZA versus equivalent latitudes reflects the displacement from the pole and split of the vortex during 22-27 September. The nighttime ex-vortex observations (triangular data points in the upper right quadrants in the plots) always exhibit the highest N_2O_5 VMR observed, reaching the maximum in the pre-split and split periods. Within the nighttime ex-vortex the highest VMRs are reached for the lowest SZA around 100^o, i.e. for locations closest to the pole. VMRs are generally smaller in the vortex than outside for both day and nighttime observations. The dependence on SZA is further highlighted in Fig. 6.8 (left and middle panels), which shows variation of N_2O_5 VMR with SZA for sections of airmasses of Fig. 6.7 located within the vortex and the equiv-

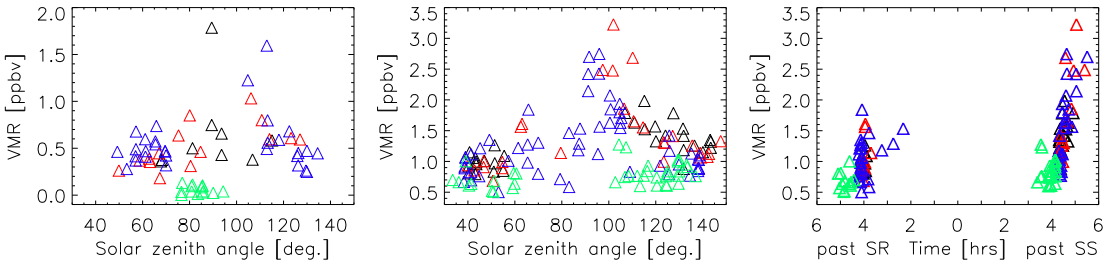

Figure 6.8: The solar zenith angle dependence of N_2O_5 VMR for inside vortex (left panel) and equivalent latitude bin of 35-40^o S (middle panel) at 850 K theta level extracted from the data shown in Figure 7. The right panel shows the observed VMR as a function of time since sunrise (SR) and sunset (SS) for data shown in the middle panel. The black, red, blue and green triangles represent the 20-21, 22-24, 25-27 September and 11-13 October periods respectively.

alent latitude bin of 35-40^o for all periods at the 850 K theta level. The latter equivalent latitude bin is so small, e.g. the CLAES nighttime zonal mean is about 2.7 ppbv between 28 and 34 km from 25 to 55^{o}S in September (see *http://www.lmsal.com/9120/CLAES/n2o5_night_v8.html*), that virtually no variation in the composition of airmass is expected. This means that we expect constant values of N_2O_5 VMR for nighttime observations (SZA $> 90^o$) within the equivalent latitudes of 5 ^{o} width. What is observed, however, is a maximum in N_2O_5 VMR near SZA=100 ^{o} or near geographic latitude of 80 ^{o}S for 22-27 September periods (representing presplit and split periods). The maxima belong to the region of enhanced N_2O_5 VMR close to the pole which are also obvious in the maps of Fig. 6.6 and which will be analyzed in detail below. The difference between day and nighttime values is less evident in the October data for the midlatitude airmass (Fig. 6.8, middle panel, green triangles). Moreover, there is no variation in N_2O_5 VMR for the vortex airmass (see Fig. 6.8, left panel, green triangles) due to small range of SZA sampled.

The variation in the time of measurements since sunrise and sunset is important for the diurnal cycle in N_2O_5 concentrations. The time since sunrise of daytime measurements for October data (Fig. 6.8, right panel, green triangles) increased in comparison to that of periods in September. In parallel, the time since sunset of nighttime measurements decreased from September to October indicating shorter time for buildup of N_2O_5 VMR before the measurements were taken. This decrease in time during which N_2O_5 builds up is the main reason for the decline in the difference between daytime and nighttime N_2O_5 VMR in October. However, the large scatter in nighttime N_2O_5 VMR during the periods of 22-27 September can not be due to diurnal variation alone since such a large scatter over a time interval less than half an hour is not expected from previous observations and model calculations [*Smith et al.*, 1996].

The vertical cross-sections of N_2O_5 VMR with respect to equivalent latitudes in Fig. 6.9 exhibit the chemical vortex boundary which is shown by the sharp VMR gradient with respect to equivalent latitudes. This boundary is consistent with the dynamical potential vorticity (PV) boundary indicated by the white solid lines. The low N_2O_5 VMR in October shows expected seasonal evolution due to lengthening of sunshine duration. Moreover, the vortex low VMRs progress towards the pole with recentering of the vortex. The nighttime average VMR with maximum at approximately 850 K potential temperature level for the period 22-24 September in the equivalent latitude range of 30 to 60^o in Fig. 6.9 results partly from the enhanced N_2O_5 VMR observed at geographical high latitudes (see Fig. 6.7 (left panel) along SZA=100^o for unusual high VMRs and

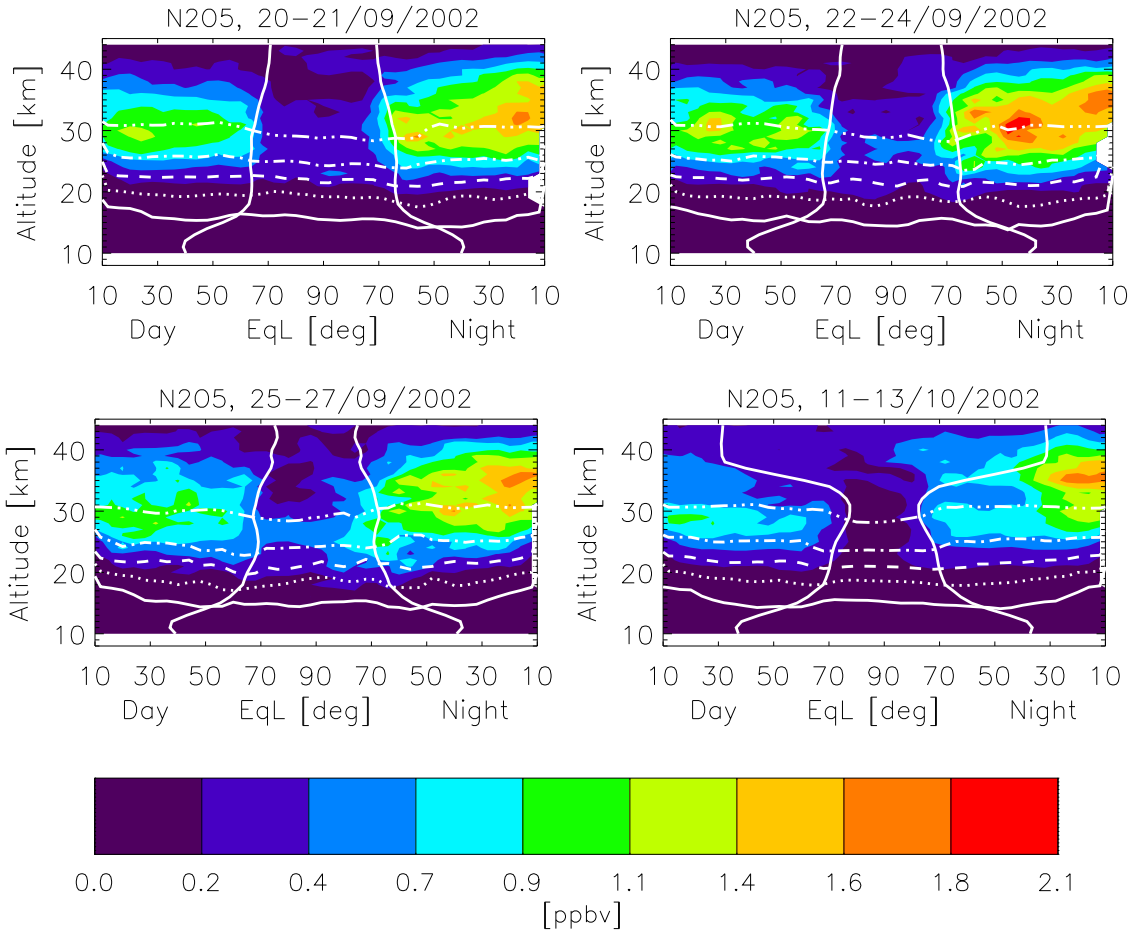

Figure 6.9: Vertical profiles of N_2O_5 VMR averaged over 4 degree equivalent latitude for early presplit, presplit, split and postsplit of the vortex. The vortex edge is overlaid by white solid line extending along the altitude axis and a wide vortex edge region is assumed to lie within 5 degree equivalent latitude width from the edge in either sides. White lines indicate potential temperature levels of 400 (solid), 475, 550, 625, 850 K (dash-dot-dot).

corresponding equivalent latitudes). This also holds for the period 25-27 September with a peak at approximately 1000 K theta level which is, however, less pronounced. This is an indication that low PV/low-latitude airmasses moved to these high latitude regions following the displacement of the vortex from the pole. The presence of airmasses corresponding to lower equivalent latitudes at high geographic latitudes in connection with generally high VMR during 22-27 September (shown in Fig. 6.7) suggests that subtropical air, relatively rich in NO_x and O_3, was being advected along the track of high N_2O_5. This argument will be substantiated later in section on NO_y partitioning.

The high VMRs observed between 22 and 27 September at high latitudes in regions which had been occupied by vortex airmasses earlier in the period are exceptionally larger than VMR which were seen in the airmasses outside the vortex on 20 September. This holds even when considering the higher VMRs outside the vortex as far away as 30^oS on 20 September. This excludes the possibility that the transport of ex-vortex airmass to high latitudes is the only factor for high VMR there. The high N_2O_5 VMRs must have been chemically produced. This is not the first time such a local enhancement of N_2O_5 VMR at high latitudes has been observed. *Kumer et al.* [1997] reported on high N_2O_5 up to a maximum of 6 ppbv at 1200 K on January 11, 1992 at high latitudes which were observed by ISAMS and CLAES on UARS during the January 1992 stratospheric warming of the northern hemisphere. They attribute the enhancement partly to locally fast chemical processes which follow the temperature contrast produced by the stratospheric warming in the order of 80 K. The temperature contrast produced by the stratospheric warming of the southern hemisphere 2002 is of similar strength between the cold pool at the pole and hot pool outside the vortex (compare the temperature on 20 September with 22 and 26 September over the high latitude regions shown in Fig. 6.10). However, the CLAES maximum enhanced N_2O_5 VMRs of 6 ppbv at 1200 K theta level are a factor of 3 larger than any measurements prior to UARS [*Kumer et al.*, 1997] and also higher compared to a value of 4.4 ppbv observed by MIPAS. The peak enhanced MIPAS N_2O_5 value is only a factor of 2 larger than its maximum values observed at the beginning of the warming. This difference might result from the fact that MIPAS measurements are taken after sunset at about 22:30 hrs local solar time while ISAMS and CLAES measurements include the maximum N_2O_5 VMR values just before sunrise. The CLAES zonal mean cited above for 25-55^oS in September at altitudes of 28-34 km is higher than the MIPAS equivalent zonal mean (see Fig. 6.9) due to the same measurement time difference that accounts for difference in the observed enhanced maximum values.

Examination of the evolution of the PV field and movement of the vortex in Fig. 6.6 shows that enhancement occurs as the warmer low latitude ex-vortex airmass (compare Fig. 6.10) moves into the region previously colder and occupied by the vortex airmass. Though the enhancement could not be investigated more closely (e.g by back trajectories calculations), the exceptional high N_2O_5 formation is believed to follow the production of relatively large amounts of NO_3 in transit through the hot pool in a similar manner as in the northern hemisphere observations of January 1992.

6.4 NO_y Budget and Partitioning

The budget and partitioning of the reactive nitrogen reservoir (NO_y) are examined using altitude-equivalent-latitude cross-sections of HNO_3, $ClONO_2$, NO_x, and N_2O_5 derived from MIPAS in the vortex, vortex edge and ex-vortex air covering the regions from vortex edge to 10^o.

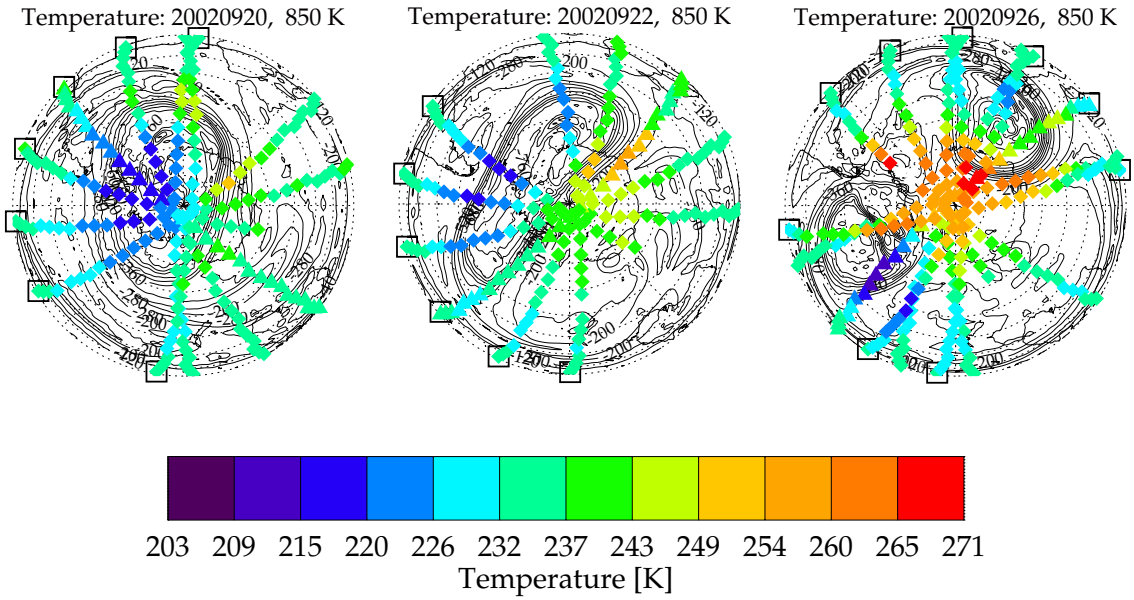

Figure 6.10: MIPAS temperature distribution at 850 K theta level for 20, 22, and 26 September measurements. The underlying contour lines show potential vorticity.

As shown in Fig. 6.11, all NO_y species have higher VMR values inside the vortex than in the vortex edge and ex-vortex regions at 400 K level (solid white line extending along horizontal axis, see also Fig. 6.3 in the total NO_y of individual data points) which is also true for all lower levels. This feature is also apparent in the equivalent zonal mean of NO_y in Fig. 6.2 constructed using 4^o equivalent latitude bins. We can exclude that this is a retrieval artefact since the maximum of the reference VMR profiles of all the species is at altitudes higher than this level. Therefore, we argue in favor of an unmixed diabatic descent or a re-nitrification caused by evaporation of PSCs. Begining at 475 K the vortex NO_y is lower than vortex edge and ex-vortex values which is exhibited in Figs. 6.2-6.11.

The high spatial variability of NO_y constituents (not shown) and the total NO_y (Figs. 6.3-6.4) during presplit and split periods within the vortex indicates that the vortex was not homogeneous. In early mid-October, the vortex became homogeneous except for the diurnal variability. These features are expected due to the fact that the vortex covered wider geographical latitudes and was thereby affected by a different degree of solar insolation and temperature distribution.

6.4.1 Inside-vortex region

We have studied daytime and nighttime partitioning of NO_y inside the vortex airmass (see Figs. 6.11-6.12). Fig. 6.12 depicts fraction of NO_y available in its constituent species in the altitude range of 10-44 km. The vortex region is bounded by two solid white lines extending along the altitude axis. The corresponding absolute values are shown in Fig. 6.11. The vortex region decreases with altitude for the whole study period with the exception of mid-October during which the vortex weakened above approximately 33 km (approximate theta level of 1000 K) and enclosed a wider area.

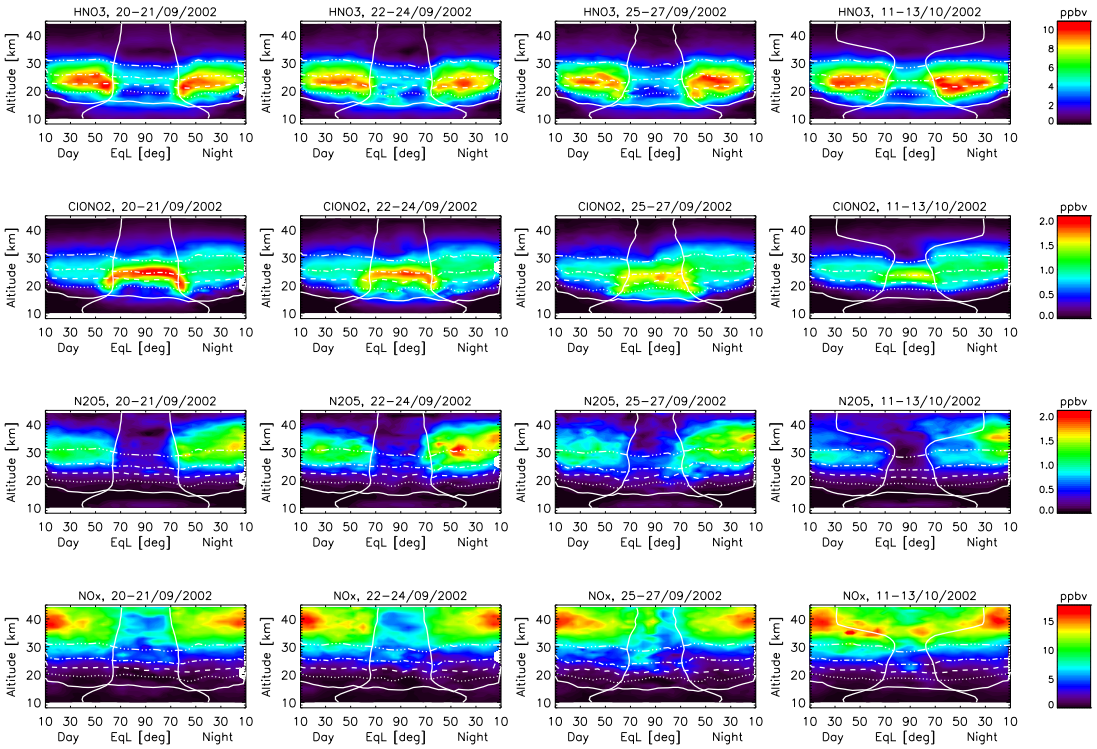

Figure 6.11: The same as Fig. 6.2 but showing daytime and nighttime NO_y partitioning in the stratosphere for individual components.

In the early presplit period and early mid-October, significant fraction of NO_y is in the form of HNO_3 and NO_x above the 400 K level which is true for other periods as well above the 550 K level (see Fig. 6.12). The two periods differ in that there was more NO_y in the form of NO_x in early mid-October than in the early presplit period. In contrast to this, most of the available day and nighttime nitrogen is in the form of HNO_3 and $ClONO_2$ between 400 K and 475 K levels during the perturbed atmosphere situation (presplit and split periods). This indicates that chlorine deactivation (via (1.4)) had taken place during the periods which is also supported by the last observation of polar stratospheric clouds by MIPAS on September 21 (for more on chlorine deactivation, see *Höpfner et al.* [2004]).

On 475 K level in Fig. 6.12, the fraction of NO_y in the form of HNO_3 decreased from about 90% in the early presplit to 60% in mid-October concurrent with a buildup of fraction of NO_y in the form of NO_x from close to zero to nearly 35%. On the 625 K level, the fraction of NO_y in the form of HNO_3 decreased from about 45% in the presplit to 30% in the split accompanied by a buildup in NO_x (via (1.14)) from approximately 30% to 40%. During the postsplit period in October, a shift in the NO_y fractioning from NO_x to HNO_3 was observed. The situation on 850 K for HNO_3 is similar to 625 K while the NO_x fraction increased from about 50% to 60% during the split and remained at this value in the postsplit period. The buildup of HNO_3 from NO_x (via (1.3)) is compensated by a sharp decline in N_2O_5 (via possibly reactions (1.10) or (1.11) or both) in the postsplit period so that NO_x remained roughly constant. This pattern of NO_y partitioning observed in equivalent zonal means is also clearly manifested in the individual data points shown in Fig. 6.13. Source/sink relations can easily be seen from such plots. The general trend towards

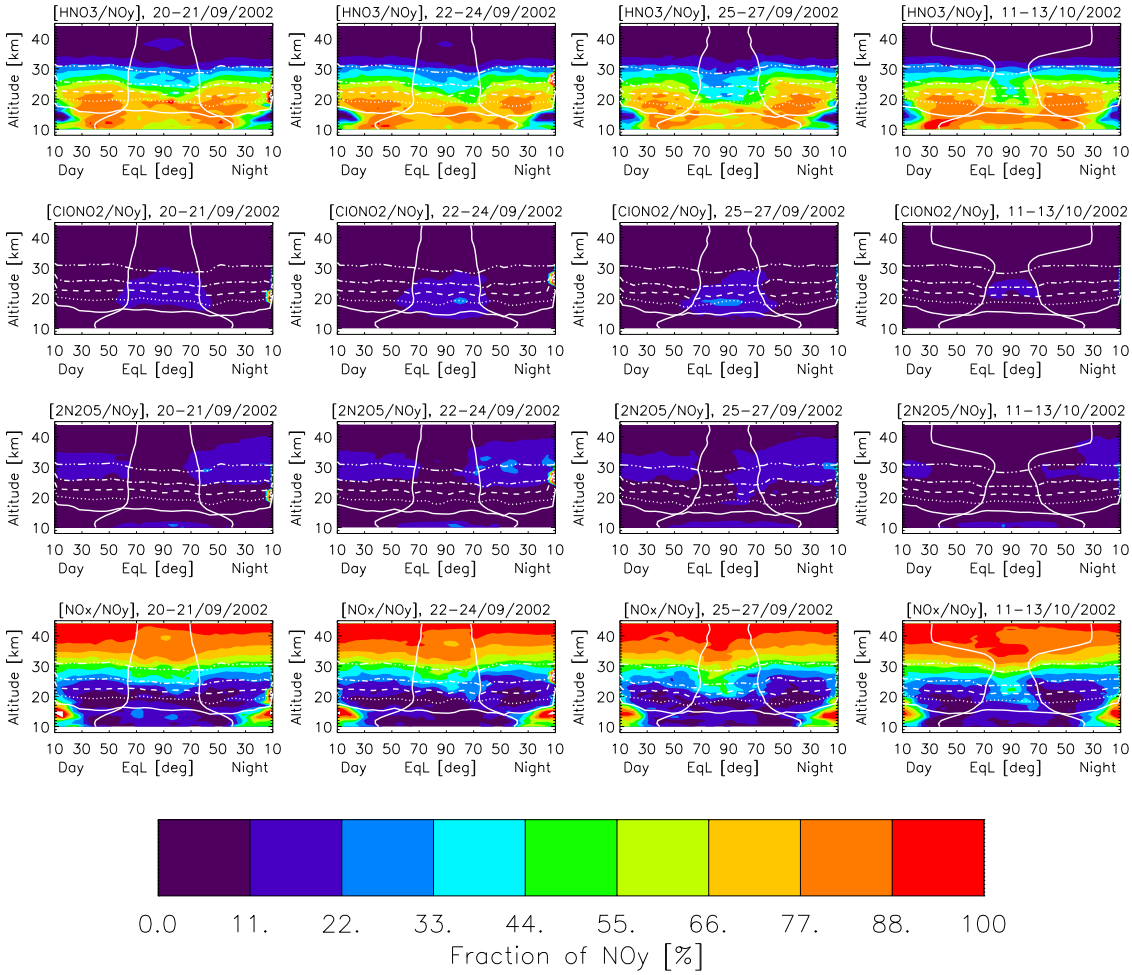

Figure 6.12: the same as Fig. 6.11 but showing daytime and nighttime NO_y fraction.

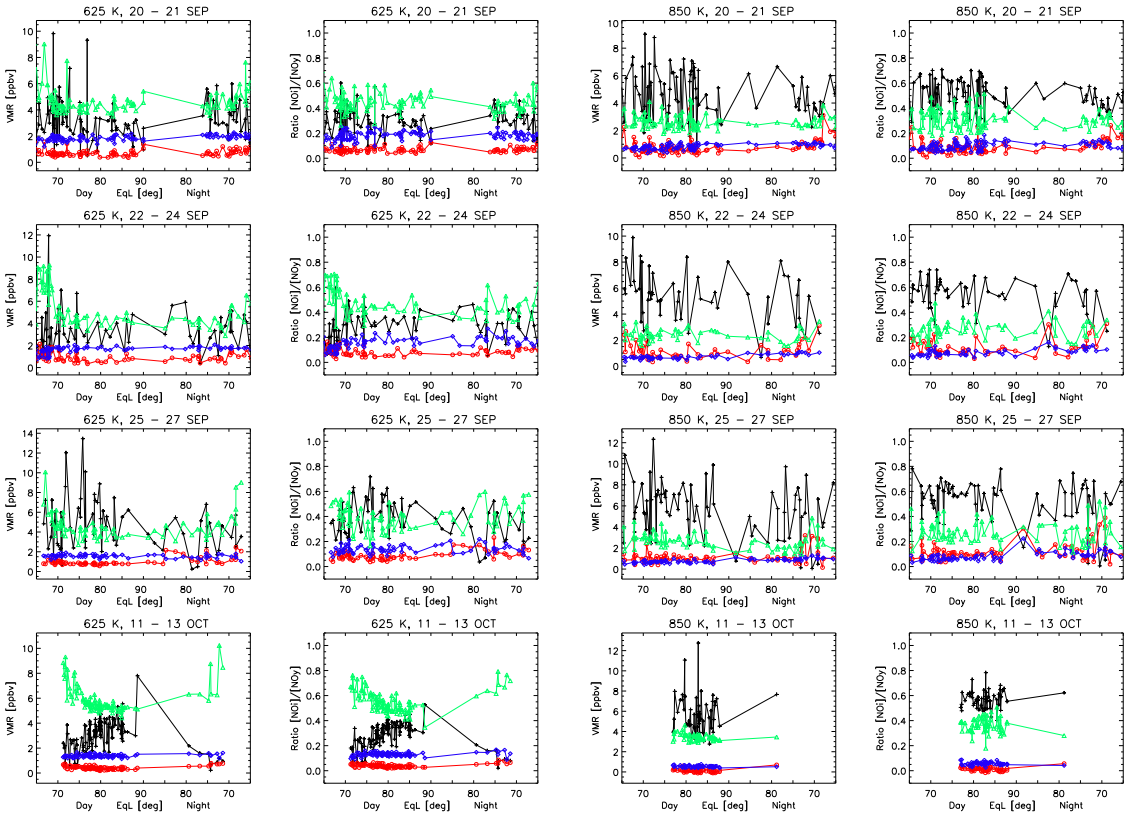

Figure 6.13: Vortex NO_y partitioning at potential temperature of 625 and 850 K. The ratio of individual NO_y components to total NO_y is ploted on the left side to separate dynamical from chemical effects. Green, black, blue and red lines represent HNO_3, NO_x, $ClONO_2$ and $2N_2O_5$ respectively.

enhanced conversion of HNO_3 into NO_x during the period 22 - 27 September on theta levels above 475 K is consistent with the displacement of the vortex from high to mid-latitudes thereby experiencing different photochemistry. The opposite trend in mid-October at 625 K is due to weak photolysis in the polar region.

There was a clear anticorrelation of $ClONO_2$ and NO_x before the vortex split so that the fraction of NO_y in the form of $ClONO_2$ has reduced remarkedly from 21-25% before the vortex split to 15-16% and 10-12% during the split and early mid-October periods at 625 K level (while these numbers refer to the range of values over all data points in the vortex, one can see this trend also in the altitude-equivalent-latitude cross-sections in Figs. 6.11-6.12). However, the dominant chemical processing during the split and afterwards was the general buildup of NO_x from HNO_3.

N_2O_5 increased substantially in the period 22 - 27 September at levels above 625 K (Figs. 6.11-6.12). In early mid-October, N_2O_5 decreased significantly leading to most part of nitrogen being found in the form of HNO_3 and NO_x. It remained at a constant value of vortex average of 1.0 ppbv before the split and during the split and sharply decreased in mid-October.

NO_x VMR in the vortex during the presplit is smaller than 7 ppbv in the altitude range of 30-40 km. Significant buildup to values larger than 10 ppbv during the split and to about 15 ppbv in October

were observed. NO_x fractions in NO_y practically remained at 75-100% for the period as a whole implying the major part of the observed buildup during the split and afterwards is transport related. However, the observed buildup in the altitude range of 20-30 km is related to photochemistry. On levels higher than 1000 K (about 33 km), NO_x accounted for most NO_y with minor contribution from N_2O_5 throughout the whole period. Observations of over 15 ppbv of NO_x in the vortex in mid-October is related to massive mixing following weakening of the mixing barrier. This is also evident in the total NO_y in Fig. 6.2.

6.4.2 Vortex edge and ex-vortex regions

A band of higher HNO_3 of up to 10 ppbv was observed in vortex edge region bewteen 475 and 550 K levels (see the 5^o wide region on either side of the vortex edge in Fig. 6.11) in early split period. This band of higher HNO_3 was also apparent in the split period but the values on the dayside of the vortex edge was smaller by 2 ppbv. The high HNO_3 along the vortex edge is known to arise from lower minimum temperature in the Antarctic vortex core than near the edge and it is known as "collar" region [*Toon et al.*, 1989]. The decrease in the values of HNO_3 in the collar region in the following days might be due to dilution of HNO_3 resulting from transport of dentrified air from the vortex interior. Further evidence in support of mixing of denitrified air from the vortex interior is the fact that values in the collar region are mainly decreased on 475 K in all three periods of September, a level which is characterized by severe denitrification as shown in Figure 2 of NO_y. The collar region is also characterized by high $ClONO_2$ VMR (for more discusion on chlorine deactivation see *Höpfner et al.* [2004] which exhibit similar decline at the same levels).

$ClONO_2$ abundance during day and nighttime in the vortex edge region (collar region) is generally higher than inside vortex values for all periods for the levels between 400 K and 550 K (see Fig. 6.11). The $ClONO_2$ VMR in the collar region as well as that in the vortex declined from early presplit to split period and significantly in mid-October. Having removed transport from chemical effects (using the ratio of individual components to the total NO_y since transport part has second order contribution in the continuity equation), the fraction of $ClONO_2$ in the vortex as well as in its edge region shows the same evolution observed in the absolute values indicating that chemical effects on partitioning are dominant factors.

The N_2O_5 buildup near the vortex edge in the latitude band of 28-35 km during presplit and split period (which is discussed in the preceeding section and indicated to be related with temperature sensitive N_2O_5 chemistry and dynamic situation during the major warming) has appeared in both Figs. 6.11-6.12. Furthermore, in the ratio of NO_x to NO_y, a sharp decline in NO_x fraction on the nightside of the plots is shown as a step function in connection with rise in the fraction of N_2O_5, a strong evidence for the formation of N_2O_5 from NO_x supporting the conclusion in that section.

6.5 Denitrification and mixing effects in NO_y deficit

A mixing line which refers to the tracer:tracer correlation pattern that results from various mixtures of two airmasses at the same potential temperature level is a key in estimating the amount of

descent followed by quasi-horizontal mixing of two airmasses along isentropic surfaces. The correlation of long-lived tracers [CH_4]:[N_2O] was used to quantify the effects of transport on the anomalous [NO_y]:[N_2O] canonical relationships of vortex air using the mixing line. Unlike the majority of the previous results in the literature, which used only very few observations [e.g measurements from balloon by *Wetzel et al.* [2002] to represent vortex and ex-vortex air, our measurements inside the vortex and midlatitudes consist of a large number of geolocations. As a result, the observed canonical relation is weakly affected by the outliers in the retrievals.

We construct compact canonical relations from measurements in the vortex and ex-vortex for the four periods. However, the vortex canonical relation constructed from these measurements is already altered by denitrification over the period of the winter. Therefore, we used the ex-vortex correlation as a proxy to early winter vortex correlation. The ex-vortex correlation might have also been altered slightly due to mixing of vortex air into the ex-vortex region since a number of minor warmings had already occurred as early as August. We therefore constructed cannonical relations from MIPAS measurements on 24 July, 2004 from only three orbits available to us before September, 2002. These relations are constructed as shown in Fig. 6.14. The [NO_y]-[N_2O] correlation for the three orbits in July is shown in the top left panel of Figure 10. The Atmospheric Trace Molecule Spectroscopy Experiment (ATMOS) ex-vortex and Fall-95 vortex [*Muscari et al.*, 2003] relations are overlaid. *Muscari et al.* [2003] derived the NO_y estimates, used to construct the Fall-95 vortex correlation, from measurements of HNO_3 by ground-based millimeter-wave spectrometer (GBMS) at the South Pole; NO and NO_2 by the Halogen Occultation Experiment (HALOE; data version 19) aboard UARS; NO_2 by the Polar Ozone and Aerosol Measurement II instrument (POAM II; data version 6) aboard the French SPOT-3 polar orbiting satellite; and calculations of minor NO_y constituents such as N_2O_5, $ClONO_2$ and HO_2NO_2 from a photochemical box model. They obtained N_2O, used for the correlation, from measurements by GBMS. The peak in NO_y VMR in ATMOS ex-vortex correlation occurred at 50 ppbv of N_2O in contrast to 73 ppbv of MIPAS July measurement and 90 ppbv of Fall-95 vortex relation. Moreover, the peak NO_y values decreased from 21 ppbv in Fall-95 vortex relations to 18 ppbv in MIPAS measurement and 16 ppbv in ATMOS ex-vortex relation. *Muscari et al.* [2003] found that a difference of 3.0 ppbv between their fall NO_y and ATMOS ex-vortex relation at most levels. They also found that the ATMOS ex-vortex curve measured in mid-spring shows close agreement with their polynomial fit for early summer period of 1993. On the basis of the observed agreement, they argued that ATMOS ex-vortex curve represents probably the transition period in the polar stratosphere, during which the [NO_y]:[N_2O] correlation evolves continuously from the breakup of the vortex in spring to its reformation during the following fall. The additional source of discrepancy between Fall-95 vortex relation and ATMOS ex-vortex could be the descent of mesospheric NO_x inside the vortex. MIPAS July correlation curve as well as correlations during the periods in September/October (see Figs. 6.15-6.18) reenforce their hypothesis showing a shift from July to October towards lower NO_y and N_2O. However, there is a difference between austral spring MIPAS ex-vortex curve and mid-spring ATMOS ex-vortex curve.

We apply two approaches described in Chapter 1 to distinguish mixing induced changes in NO_y from denitrification. The ex-vortex relations between [CH_4]:[N_2O] and [CFC-11]:[N_2O] are shown in the top right and bottom left panel of Fig. 6.14. In the bottom right panel, NO_y versus artificial reference tracer constructed from CH_4, N_2O and CFC-11 as described in *Esler and Waugh* [2002] is shown. The artificial reference tracer formed from these tracers is given by

$$[x]_{ppbv} = 0.0232[CH_4]_{ppbv} - 0.0102[CFC-11]_{pptv} - 0.1142[N_2O]_{ppbv} + 2.5549$$

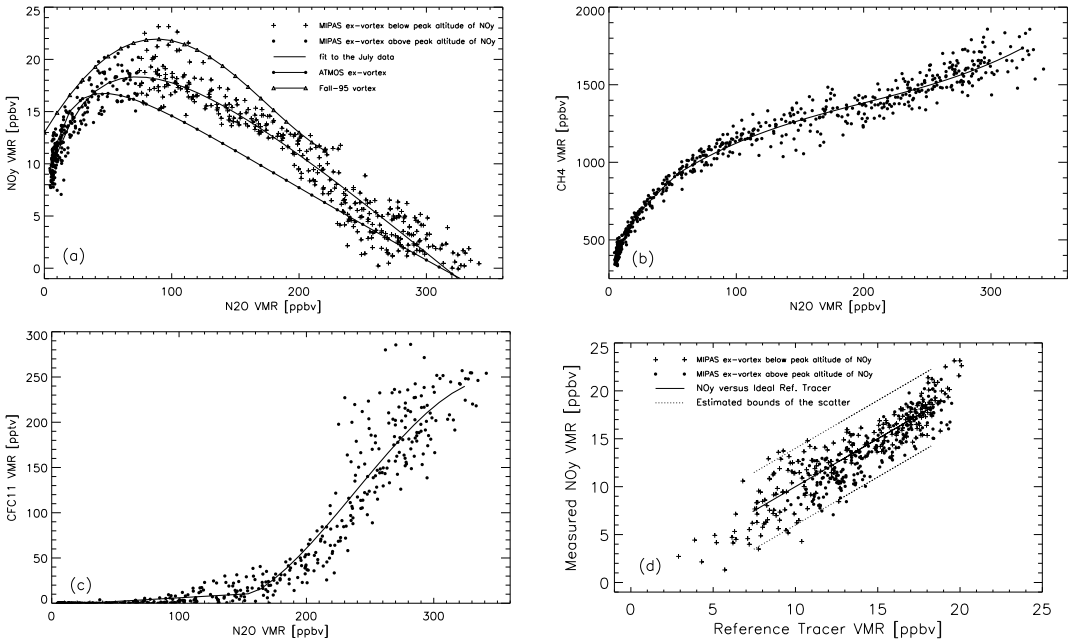

Figure 6.14: MIPAS (a). [NO_y]:[N_2O], (b). [CH_4]:[N_2O], (c). [CFC-11]:[N_2O] and (d). NO_y versus artificial tracer relationships. ATMOS ex-vortex mid-spring and Fall-95 Antarctic vortex correlation curves are overlaid in panel a.

over a range of 6 - 300 ppbv N_2O VMR. If mixing of airmass containing N_2O outside this range at the beginning of the winter with airmass in this range later in the spring occurs then it is unlikely to account for it as mixing and hence can be an accounted source of uncertainity in the estimated denitrification. In panel (a) of Figs. 6.15-6.18, [$CH4_4$]:[N_2O] reference July data, correlation curve, vortex and ex-vortex data, and linear fit to vortex data are plotted for the four periods. As noted by *Glatthor et al.* [2004], the high bias in N_2O in the September data set does not affect the correlation in the important range of 0-250 ppbv N_2O where mixing could significantly influence quantitative determination of denitrification. A straight line can easily be drawn through the vortex data for the four periods over nearly the whole range smaller than 250 ppbv which indicates that a number of single mixing events and/or continuous mixing throughout the winter have taken place during the winter. The use of these lines, however, can significantly overestimate mixing-induced changes in NO_y abundances. The artificial reference tracer method, in contrast, is valid equally for all mixing scenarios.

In panel (c) of Figs. 6.15-6.18, NO_y versus the reference tracer is shown. The data points representing ex-vortex measurements are well contained within the bound allowed by the scatter (approximately 1.7σ, 1σ represents absolute mean of the deviation from ideal straight line) in the reference tracer determined from July measurements. Much of the data points, measured in vortex airmass having 73-250 ppbv of N_2O and NO_y smaller than 5 ppbv shown in panel (b) in Fig. 6.15 for the early presplit period, lie below the bound of mixing scatter in panel (c), i.e these represent denitrified airmass. Denitrification is also observed for airmasses containing N_2O smaller than 70 ppbv (see open circles). The NO_y anomaly accountable to denitrification is determined in a straight forward manner by subtracting expected NO_y according to artificial reference tracer from measured NO_y. The mean denitrification and total NO_y anomaly for the early presplit period are

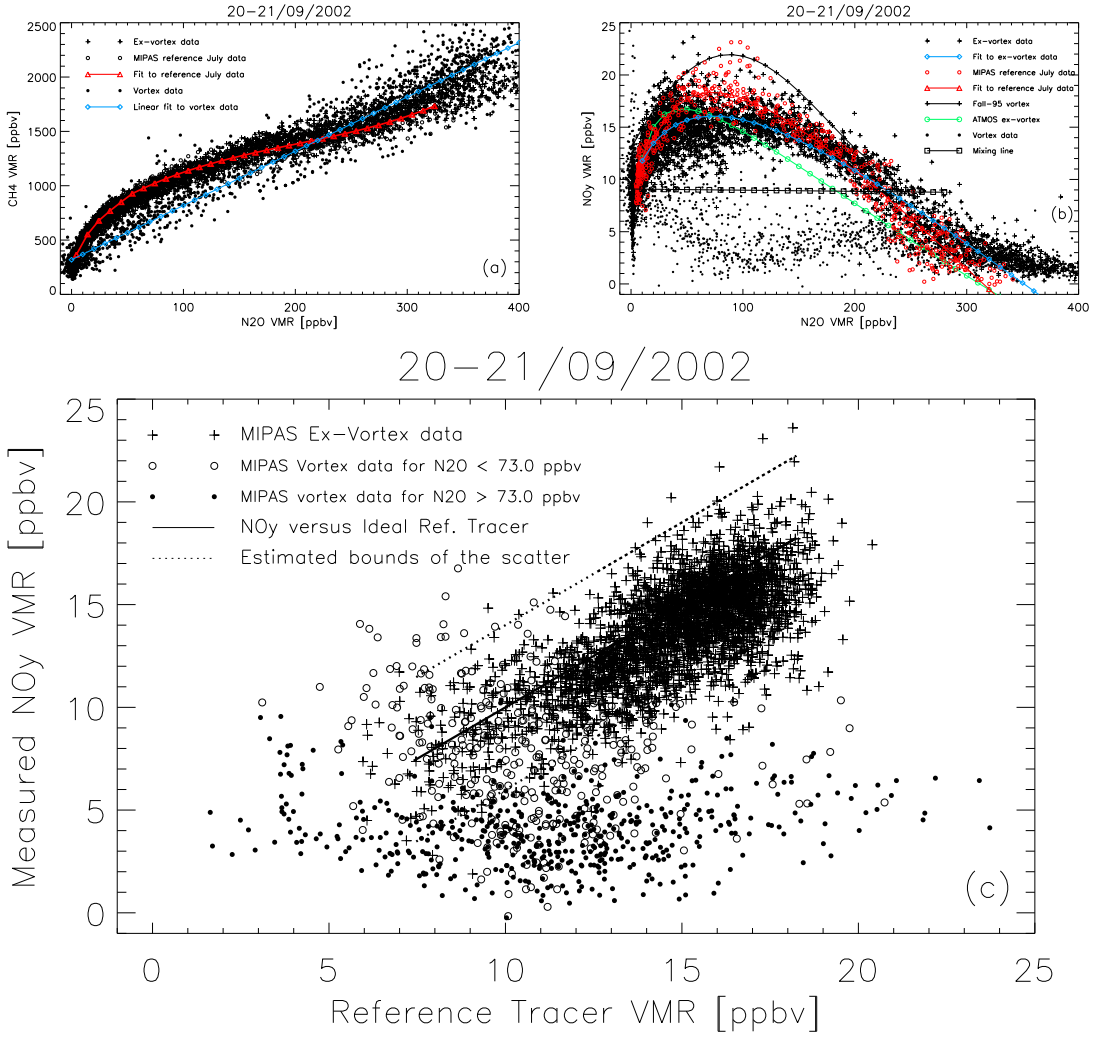

Figure 6.15: MIPAS (a). $[CH_4]$:$[N_2O]$, (b). $[NO_y]$:$[N_2O]$, and (c). NO_y versus artificial tracer relationships built from July data for the early presplit period. Vortex scatter points above the altitude of peak NO_y VMR are shown by open circles and those below these levels are shown by filled circles. Note that most of the data shown by open circles are contained within the bounds of mixing scatter.

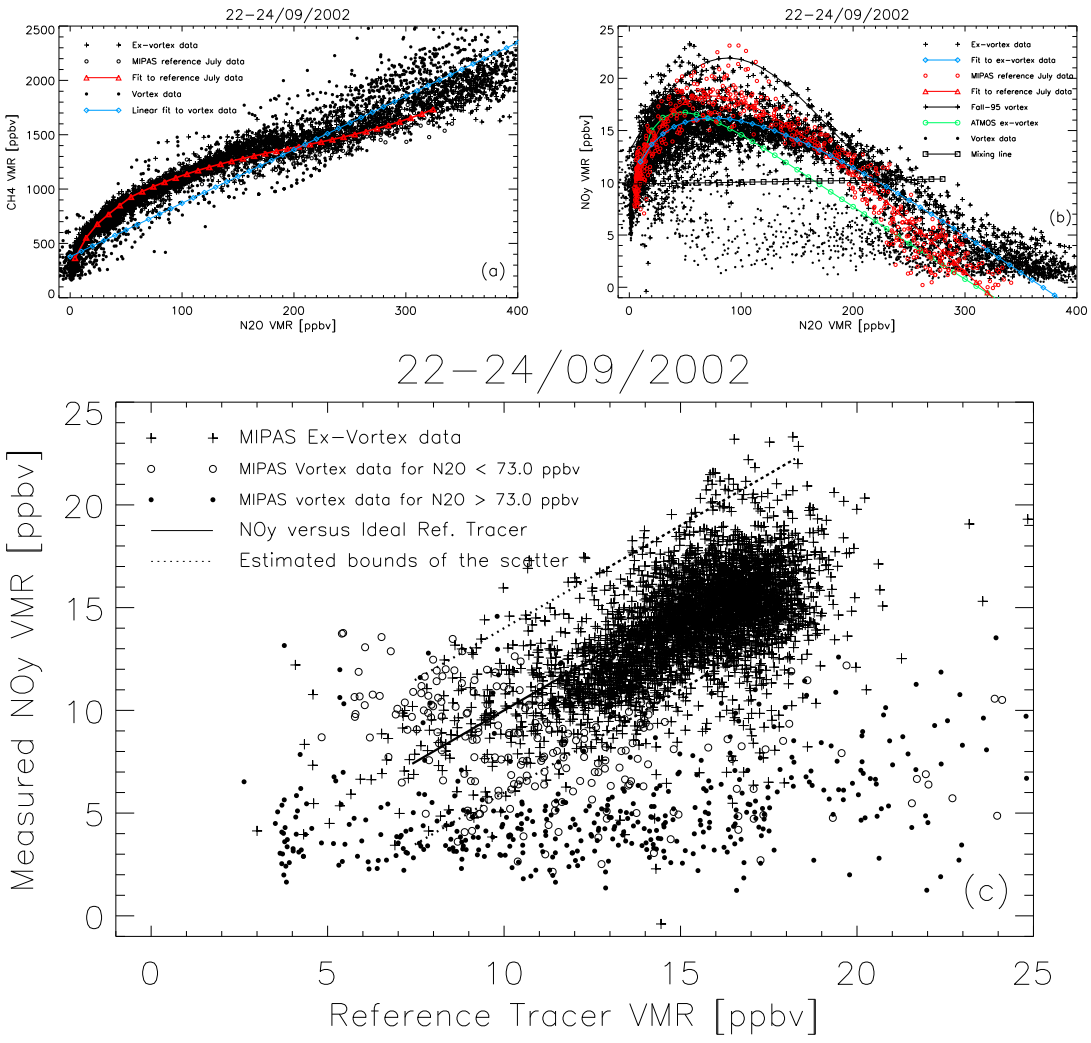

Figure 6.16: The same as Fig. 6.15, but for the presplit period.

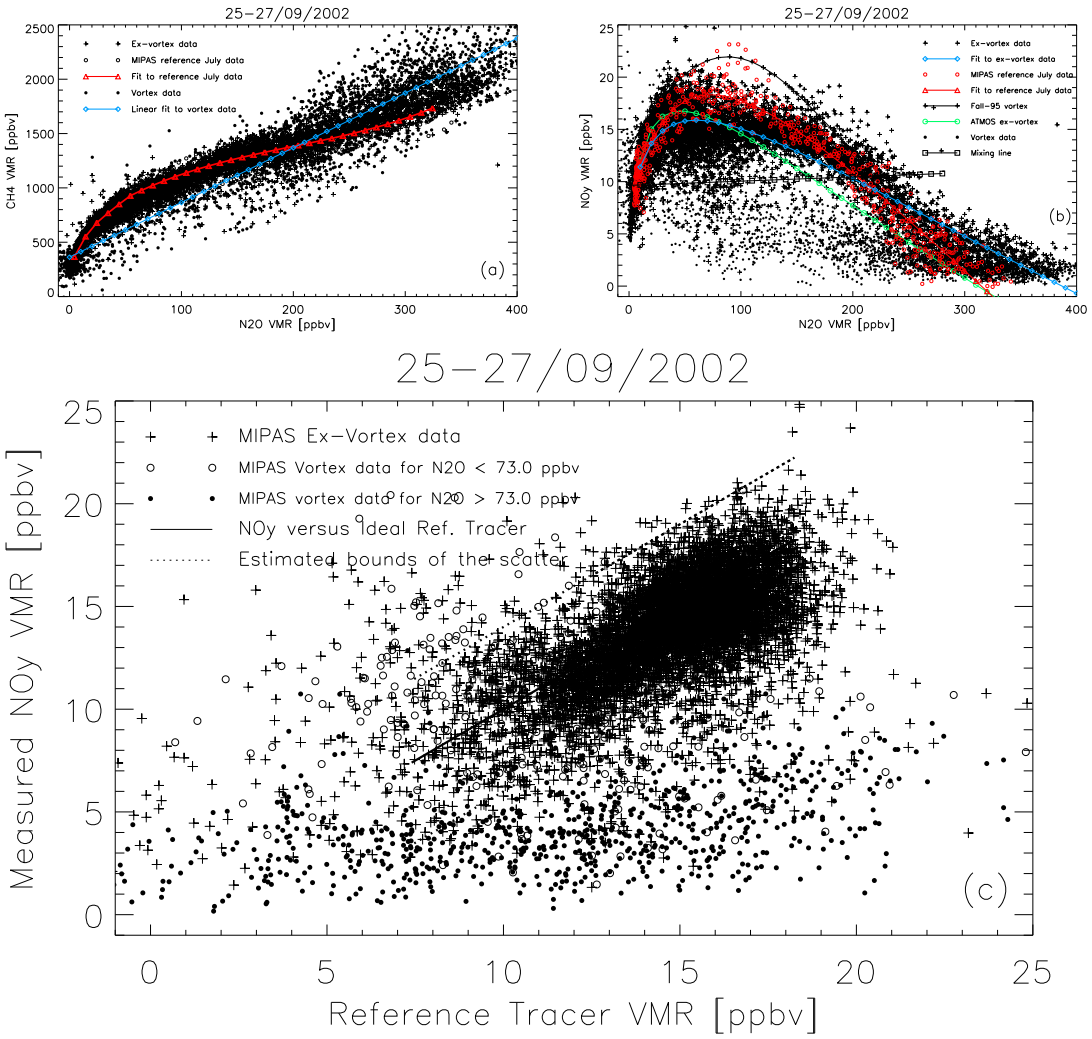

Figure 6.17: The same as Fig. 6.15, but for the split period.

given in panel (a) of Fig. 6.19. The error bar represents the standard deviation of the mean, i.e $\frac{\sigma}{n}$. The maximum NO_y deficit of 12.5 ppbv occurred near 475 K of which denitrification accounted for approximately 9.0 ppbv. On the other hand, the denitrification estimated from the mixing line method is about 6.0 ppbv and thus lower by 30% than that estimated by the artificial reference tracer method.

The NO_y deficit above altitude of 73 ppbv N_2O (peak altitude of NO_y in the reference data) are accounted mostly by mixing as shown by data points labelled by open circle in panel (c) of Fig. 6.16 for the presplit period. The mean deficit and denitrification inside the vortex are shown in panel (b) of Fig. 6.19. The mean deficit on 475 K level is 11.3 ppbv of which about 9.0 ppbv is dentrification-induced changes. The split period correlation of $[NO_y]$:$[N_2O]$ vortex data in panel (b) of Fig. 6.17 showed large scatter. The ex-vortex data exhibited similar behaviour. Consequently, the number of data points in the ex-vortex which lies below the bound of mixing scatter have appreciably increased. The mean NO_y deficit on 475 K (panel (c) of Fig. 6.19) is 12.5 ppbv and denitrification contributed 7.5 ppbv of this value. A reduction by about 1.5 ppbv in denitrification from the pre-

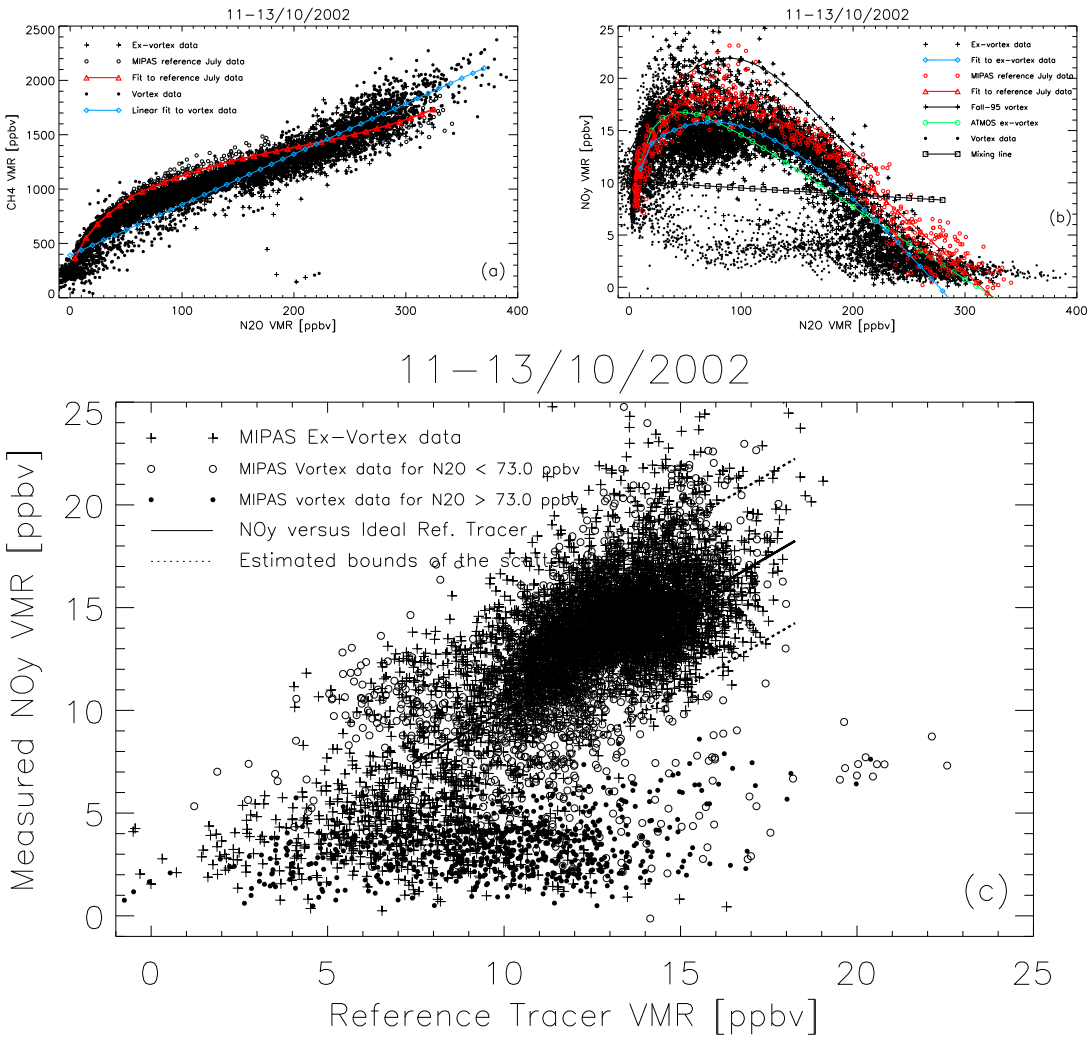

Figure 6.18: The same as Fig. 6.15, but for the postsplit period.

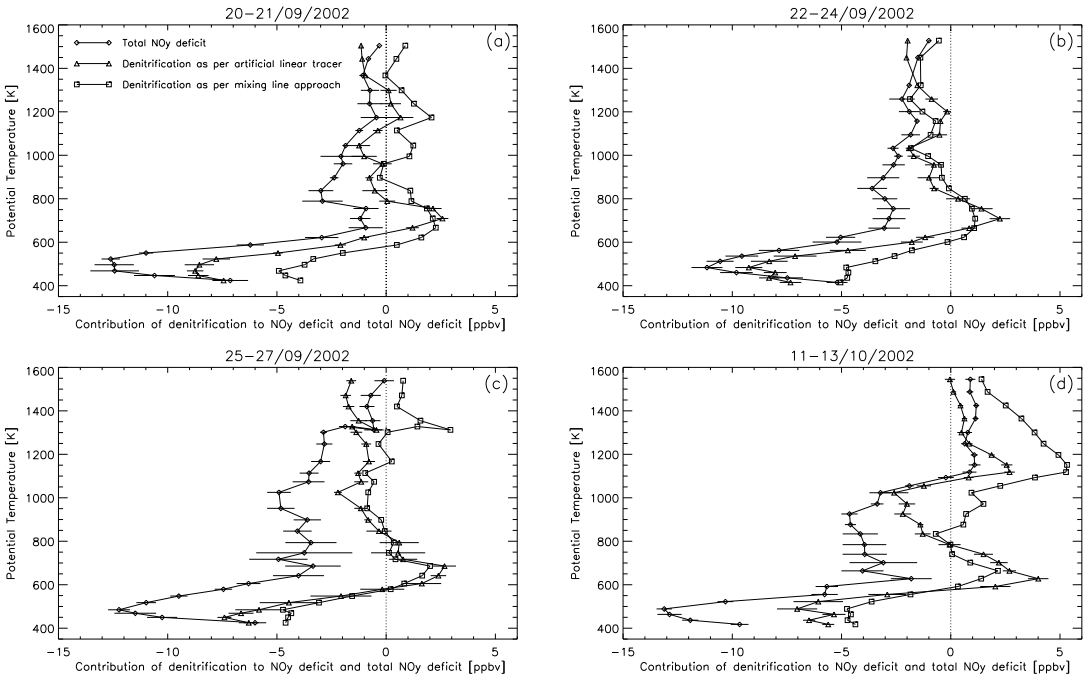

Figure 6.19: Vertical distribution of the NO_y deficit and contribution of the denitrification as estimated by the two different methods (indicated by the legend in panel (a)). The error bar is the standard deviation of the mean while the scatter in the data is much higher. The theta range covers the range of N_2O between 6-300 ppbv in which the artificial reference tracer is constructed. Data outside this range is not considered since the reference tracer method can not capture mixing outside the range of data used for its definition.

ceeding periods is slightly higher than the standard deviation of the mean. On the other hand, the mixing line approach gives estimates of about 5.0 ppbv denitrification-induced and the remaining to mixing-induced deficits for both presplit and split periods.

The postsplit ex-vortex as well as vortex data points showed less scatter in comparison to the measurements in September in all three panels of Fig. 6.18. The mean estimated denitrification accounted for 7.0 ppbv of 13.0 ppbv mean deficit (see panel (d) of Fig. 6.19). The ex-vortex data are well contained within the bounds of mixing scatter. The remaining deficit in vortex NO_y at 475 K, accountable to mixing, increased from approximately 3.0 ppbv during presplit to 5.0 and 6.0 ppbv during the split and postsplit periods. A reduction of NO_y deficit above 1000 K in postsplit period is due to mixinig of NO_x across weak vortex barrier (panel (d) of Fig. 6.19). The estimated denitrification from mixing line is 5.5 ppbv during the postsplit period which is lower than the linear reference tracer estimates of 7.0 ppbv.

Chapter 7

Conclusion

The highlight on the history of remote sensing and factors that contribute to its evolution to current state is briefly introduced. The importance of IR spectroscopy and one of the techniques in the IR spectroscopy, Fourier Transform Infrared Spectroscopy (FTIR) using Michelson Interformeter are described. The retrieval algorithm used to derive temperature and composition of the atmosphere from limb radiances measured by MIPAS is tested for consistency with the conceptually different Hessian method. The diagnostics of the retrieved VMR using the most difficult components of NO_y, N_2O_5 as an example, are given. The impact of major warming on stratospheric N_2O_5 chemistry is discussed. Moreover, the analysis of stratospheric nitrogen species and source gases derived from limb radiances measured by MIPAS during the major stratospheric warming of Antarctic polar vortex has shown that the instrument is vital for capturing important information useful to reenforce as well as improve our current understanding of the role of chemistry and dynamics on NO_y partitioning and budget in the stratosphere. In line with, the findings in this thesis are summarized as follows.

We have compared the conventional Gauss-Newton-type retrieval algorithm with conceptually different and recently improved Hessian approach for testing the consistency of results. The derived profiles and uncertainities using the two methods are practically identical in the original state vector coordinate system. Due to interlevel correlations, the agreement in the uncertainities in the original state vector coordinate system is partly lost in a space in which the elements of transformed state vector are independent. After orthogonal coordinate transformation in which an independent quantity $\mathbf{z}$ is defined, noticeable differences on the accuracy of the uncertainities in $\mathbf{z}$ are observed. The significant discrepancies between the uncertainities estimated by the two methods are shown to be related with elements of parameter vector $\mathbf{z}$ which are dominatly controlled by flattest eigenvector directions. The improved Hessian method determines the uncertainities in these shallowest directions with better accuracy as confirmed by good agreement of variation of computed χ^2 around the minimum of $\mathbf{z}$ with ideal χ^2. The performance of the Hessian method is also found to be better in resolving structures related to the shallowest directions as revealed by better vertical resolutions for both H_2O and $ClONO_2$. The main causes for these differences are the contribution of nonlinearity in the Hessian approach and analytical approximation of derivative of the forward model with respect to VMR in the Gauss-Newton algorithm. The results of comparison of the two methods can only serve to appreciate the level of accuarcy and consistency of the variant of the Gauss-Newton algorithm used to retrieve the NO_y constituent species and

long-lived species since the differences are minor to affect results and conclusion of the study on the impact of the sudden major warming of SH polar vortex on NO_y budget and partitioning reported in the thesis in the original state vector space. Moreover, the disadvantage of the Hessian approach over the traditional nonlinear optimization such as Gauss-Newton is its excessive computation time since successive approximation for the right step size in each eigenvector direction is done separately in subspace of each parameter. This hinders its applicability to operational processing of atmospheric parameters. However, when the accurate estimate of error matrix and when testing of scientific retrieval algorithm such as the one used to generate the data set in this study are required, the Hessian method is worthy to use. In addition, when the size of retrieval parameters is small, such as for example retrieval of instrumental parameters (e.g. instrumental line shape, residual spectral shift etc.), it can be applied with less computation time.

N_2O_5 was retrieved for the first time from MIPAS/ENVISAT limb emission radiances on a global scale since ISAMS and CLAES measurements in 1992. The spectral background continuum is shown to be uniform for the selected spectral regions for the retrieval of N_2O_5. Thus, constraining the background continuum in the ν_{12} band to that in the external microwindows avoids erronous propagation of continuum-like N_2O_5 signal to background continuum or vice versa. The approach proposed in this thesis is robust enough to isolate background continuum and N_2O_5 signatures at least for application to an atmosphere with low aerosol loading. The regularization parameter selected on the basis of some test retrievals has been found to be valid for most cases as confirmed from consistency of over 1400 profiles retrieved for the period September/October 2002 in the Southern hemisphere with the observed dynamics and chemistry. This work verifies that the methodology that overcomes the problem of distinguishing the rather flat N_2O_5 spectral signature from background radiances is suitable and it has been identified and tested for consistency with dynamical and chemical processes.

The main characteristic features such as diurnal variation, the link to the chemistry that governs its partitioning within the NO_y family and its decline in mid-October due to increased day length are observed. The retrieved N_2O_5 VMR from high resolution atmospheric limb emission spectra measured by MIPAS during the major warming over Antarctica in September 2002 exhibits expected dynamical features such as a clear boundary between inside vortex and outside vortex air, movement of the vortex boundary from September to October, and day-night asymmetry due to photolysis of N_2O_5. Moreover, the enhanced N_2O_5 VMR at high latitudes is found to result from a combination of transport of NO_x rich air through the hot pool yielding a relatively large amount of NO_3 in transit together with the highly temperature sensitive N_2O_5 formation chemistry.

NO_y partitioning inside the vortex is found to be less driven by isentropic mixing processes during the course of the vortex split in the lower stratosphere as seen from inter-periodical variation. However, transport in the context of displacement of massive airmasses, e.g. vortex air to lower latitudes and low or midlatitude airmasses to high latitudes have affected NO_y partitioning. Some of the chemical reactions that govern NO_y partitioning are temperature sensitive. The enhancement in N_2O_5 during the split of the vortex at high latitudes, during which there was major mass transport from and to polar regions, was initiated due to its temperature sensitive formation from NO_2 and availability of NO_2 and O_3 rich midlatitude air. In parallel, the vortex airmass transport to lower latitudes (as low as 30^o) enhanced photochemical production of NO_x from HNO_3 inside the vortex. The important role of transport in preconditioning onset or cessation of photochemical reactions was also demonstrated by the buildup of HNO_3, at the same levels where HNO_3 was depleted during the split of vortex, in October after the vortex recentred itself on the pole. On

the other hand, the increase in NO_x inside the vortex at altitude between 30-40 km from September to October is mostly related with transport of midlatitude NO_x rich air. Small fraction of the enhancement in NO_x in October resulted from lengthening of day which inhibit N_2O_5 conversion.

The reference [NO_y]:[N_2O] correlation curve determined from MIPAS July data seems to represent the transition period (late winter) in the polar stratosphere, during which the [NO_y]:[N_2O] correlation evolves continuously from the formation of the vortex during the preceeding fall (Fall-93 relation) to its breakup in spring (ATMOS ex-vortex relation). The evolution of the MIPAS ex-vortex correlation curve from July to the September/October period of this study is also in agreement with hypothesis forwarded by *Muscari et al.* [2003]. At the linear end of the correlation curve due to high bias in N_2O in September, no conclusion can be drawn on the evolution of the correlation curve.

The mean NO_y deficit has been established using the values estimated from the observed N_2O values employing the [NO_y]:[N_2O] relationship determined from ex-vortex profiles. A possible quasi-isentropic mixing event scenario is established over a wide range of theta levels from correlations of the two inert gases CH_4 and N_2O for each period under study to distinguish denitrification induced changes in NO_y from that due to a descent followed by quasi-horizontal mixing. The estimates of denitrification induced deficit from this approach is compared to that derived from a linear artificial reference tracer approach and turned out to be lower than the latter by 30% for presplit periods (20-24 September). This difference is reduced to approximately 20% during the split and postsplit periods.

The mean NO_y deficit at 475 K remained on average at 12.5 ppbv throughout the period. However, the fractions of the deficit accountable to descent followed by mixing and denitrification have shown a different behaviour in the period before the split and after the split of vortex according to the reference tracer method. Mixing-induced changes accounted only for nearly 25% of the deficit before the split of the vortex and it increased to nearly 40-45% during and in the postsplit period in October. As a result, contribution of denitrification to the NO_y deficit has fallen from 75% to 55-60%. In contrast, the mixing line approach gives approximately 55-60% of deficit as due to mixing before and during the split period and 62% of deficit as due to mixing in the postsplit period which shows a high bias for mixing-induced changes due to a wider range of theta levels used to construct the mixing line. The evolution in time of the changes from artificial reference tracer method shows better consistency with altitude-equivalent latitude cross-sections of N_2O, NO_y and its components (e.g. excess NO_y above 1000 K in October compared to expected values due to horizontal mass influx into the vortex).

The permanent removal of NO_y from lower stratosphere embedded in polar stratospheric clouds accounted for the major part of the NO_y deficit. The decrease in denitrification during and after the split while the total deficit remained at its presplit value is an indication of a possible renitrification compensated by further descent and mixing.

The NO_y partitioning and budget observed during the unusual major warmings of the Antarctic stratosphere, though atypical for the Southern Hemisphere, are within scope of current understanding of stratospheric chemistry.

Bibliography

Barath, F. T., et al. (1993), The Upper Atmosphere Research Satellite microwave limb sounder instrument, *J. Geophys. Res.*, *98*(D6), 10,751–10,762.

Bates, D. M., and D. G. Watts (1980), *Nonlinear Regression and Its Application*, 357 pp. pp., Wiley, New York.

Brasseur, G., and S. Solomon (1986), *Aeronomy of the Middle Atmosphere*, second ed., Atmospheric Science Library, D. Reidel Publishing Company, Dordrecht, Holland.

Bühler, O., and P. H. Haynes (1999), Constraints on the mean mass transport across potential vorticity contours, *J. Atmos. Sci.*, *56*(7), 942–947.

Cantrell, C. A., J. A. Davidson, A. H. McDaniel, R. E. Shetter, and J. G. Calvert (1988), Infrared absorption cross sections for N_2O_5, *Chem. Phys. Lett.*, *148*, 358–363.

Chen et. al, P. (1994), Quasi-horizontal transport and mixing in the antarctic stratosphere, *J. Geophys. Res.*, *99*, 16,851–16,866.

Echle, G., T. von Clarmann, and H. Oelhaf (1998), Optical and microphysical parameters of the Mt. Pinatubo aerosol as determined from MIPAS–B mid–IR limb emission spectra, *J. Geophys. Res.*, *103*(D15), 19,193–19,211.

Echle, G., et al. (2000), Optimized spectral microwindows for data analysis of the Michelson Interferometer for Passive Atmospheric Sounding on the Environmental Satellite, *Appl. Opt.*, *39*(30), 5531–5540.

Endemann, M., and H. Fischer (1993), Envisat's high–resolution limb sounder: MIPAS, *ESA bulletin*, *76*, 47–52.

Esler, J. G., and D. W. Waugh (2002), A method for estimating the extent of denitrification of arctic polar vortex air from tracer-tracer scatter plots, *J. Geophys. Res.*, *107(D13), doi:10.1029/2001JD001071*.

European Space Agency (2000), *Envisat, MIPAS An instrument for atmospheric chemistry and climate research*, ESA Publications Division, ESTEC, P. O. Box 299, 2200 AG Noordwijk, The Netherlands, SP-1229.

Fahey, D. W., S. Solomon, S. R. Kawa, M. Loewenstein, J. R. Podolske, S. E. Strahan, and K. R. Chan (1990), A diagnostic for denitrification in the winter polar stratospheres, *Nature*, *345*, 698–702.

Farman, J. C., B. G. Gardiner, and J. D. Shanklin (1985), Large losses of total ozone in Antarctica reveal seasonal ClO_x/NO_x interaction, *Nature*, *315*, 207–210.

Fischer, H., and H. Oelhaf (1996), Remote sensing of vertical profiles of atmospheric trace constituents with MIPAS limb-emission spectrometers, *Appl. Opt.*, *35*(16), 2787–2796.

Friedl-Vallon, F., G. Maucher, A. Kleinert, A. Lengel, C. Keim, H. Oelhaf, H. Fischer, M. Seefeldner, and O. Trieschmann (2004), Design and characterisation of the ballon–borne Michelson Interferometer for Passive Atmospheric Sounding (MIPAS–B2), *Appl. Opt.*, *43*(16), 3335–3355.

Funke, B., et al. (2003), Non–LTE retrieval of NO, NO_2, and CO from MIPAS–ENVISAT, in *11^{th} International Workshop on Atmospheric Science from Space using Fourier Transform Spectrometry, Bad Wildbad, Germany, Oct. 8–10, 2003*, Forschungszentrum Karlsruhe, Institut für Meteorologie und Klimaforschung.

Funke et. al, B. (2004), Retrieval of stratospheric NO_x from 5.3 and 6.2 μ m non-lte emissions measured by mipas on envisat, *submitted to J. Geophys. Res.*

Gao, R. S., et al. (1999), A comparison of observations and model simulations of NO_x/NO_y in the lower stratosphere, *Geophys. Res. Lett.*, *26*(8), 1153–1156.

Glatthor, N., et al. (2004), Mixing processes during the Antarctic vortex split in September/October 2002 as inferred from source gas and ozone distributions from MIPAS/ENVISAT, *J. Atmos. Sci., Special issue on Antarctic Vortex 2002, accepted 7 January 2004*.

Goldman et. al, A. (1998), HNO_3 line parameters: 1996 hitran update and new results, *J. Quant. Spectrosc. Radiat. Transfer*, *60*, 851–861.

Höpfner, M., et al. (2004), First spaceborne observations of Antarctic stratospheric $ClONO_2$ recovery: Austral spring 2002, *J. Geophys. Res.*, *109*(D11), D11308, doi:10.1029/2004JD004609.

Jacobson, M. Z. (1999), *Fundamental of Atmospheric Modeling*, Cambridge University Press.

Jucks, K. W., R. Rodrigues, R. Le Doucen, C. Claveau, W. A. Traub, and J.-M. Hartmann (1999), Model, software, and database for computation of line–mixing effects in infrared Q branches of atmospheric CO_2: II. Minor and asymmetric isotopomers, *J. Quant. Spectrosc. Radiat. Transfer*, *63*(1), 31–48.

King, P., I. R. McKinnon, J. G. Mathieson, and I. R. Wilson (1976), Upper limit to stratospheric N_2O_5 abundance, *J. Atmos. Sci.*, *33*, 1657–1659.

Kondo, Y., et al. (1999), NO_y–N_2O correlation observed inside the Arctic vortex in February 1997: Dynamical and chemical effects, *J. Geophys. Res.*, *104*(D7), 8215–8224.

Kumer, J. B., S. R. Kawa, A. E. Roche, J. L. Mergenthaler, S. E. Smith, F. W. Taylor, P. S. Connell, and A. R. Douglass (1997), UARS first global N_2O_5 data sets: Application to a stratospheric warming event in January 1992, *J. Geophys. Res.*, *102*(D3), 3575–3582.

Levenberg, K. (1944), A method for the solution of certain non–linear problems in least squares, *Quart. Appl. Math.*, *2*, 164–168.

López-Puertas, M., and F. W. Taylor (2001), *Non-LTE radiative transfer in the Atmosphere*, World Scientific Pub., Singapore.

Manney, G. L., R. W. Zurek, A. O'Neill, and R. Swinbank (1994), On the motion of air through the stratospheric polar vortex, *J. Atmos. Sci.*, *51*(20), 2973–2994.

Marquardt, D. W. (1963), An algorithm for least–squares estimation of nonlinear parameters, *J. Soc. Indust. Appl. Math.*, *11*(2), 431–441.

Michelsen, H. A., G. L. Manney, M. R. Gunson, and R. Zander (1998), Correlations of stratospheric abundances of NO_y, O_3, N_2O, and CH_4 derived from ATMOS measuremets, *J. Geophys. Res.*, *103*(D21), 28,347–28,359.

Muscari, G., R. L. de Zafra, and S. Smyshlyaev (2003), Evolution of the NO_y–N_2O correlation in the Antarctic stratosphere during 1993 and 1995, *J. Geophys. Res.*, *108*(D14), 4428, doi: 10.1029/2002JD002871.

Nash, E. R., P. A. Newmann, J. E. Rosenfield, and M. R. Schoeberl (1996), An objective determination of the polar vortex using Ertel's potential vorticity, *J. Geophys. Res.*, *101*, 9471–9478.

Newnham, D., J. Ballard, and M. Page (1993), Infrared absorbance cross-sections for dinitrogen pentoxide vapour, *J. Quant. Spectrosc. Radiat. Transfer*, *50*(6), 571–577.

Perrin, A., J.-M. Flaud, A. Goldman, C. Camy-Peyret, W. J. Lafferty, P. Arcas, and C. P. Rinsland (1998), NO_2 and SO_2 line parameters: 1996 HITRAN update and new results, *J. Quant. Spectrosc. Radiat. Transfer*, *60*(5), 839–850.

Pumplin, J., D. R. Stump, and W. K. Tung (2001), Multivariate fitting and the error matrix in global analysis of data, *Phys. Rev. D*, *65*, doi:10.1103/PhysRevD.65.014011.

Rex, M., et al. (1999), Subsidence, mixing, and denitrification of Arctic polar vortex air measured during POLARIS, *J. Geophys. Res.*, *104*(D21), 26,611–26,623.

Rinsland, C. P., et al. (1999), Polar stratospheric descent of NO_y and CO and Arctic denitrification during winter 1992–1993, *J. Geophys. Res.*, *104*(D1), 1847–1861.

Rodgers, C. D. (1976), Retrieval of atmospheric temperature and composition from remote measurements of thermal radiation, *Rev. Geophys. Space Phys.*, *14*(4), 609–624.

Rodgers, C. D. (1990), Characterization and error analysis of profiles retrieved from remote sounding measurements, *J. Geophys. Res.*, *95*(D5), 5587–5595.

Rodgers, C. D. (2000), *Inverse Methods for Atmospheric Sounding: Theory and Practice, Series on Atmospheric, Oceanic and Planetary Physics, F. W. Taylor, ed.*, vol. 2, World Scientific.

Rodgers, C. D., and B. J. Connor (2003), Intercomparison of remote sounding instruments, *J. Geophys. Res.*, *108*(D3), 4116, doi:10.1029/2002JD002299.

Roscoe, H. K. (1982), Tentative observation of stratospheric N_2O_5, *Geophys. Res. Lett.*, *9*, 901–902.

Roscoe, H. K. (1991), Review and revision of measurements of stratospheric N_2O_5, *J. Geophys. Res.*, *96*(D6), 10,879–10,884.

Rosenlof et. al, K. H. (1997), Hemispheric asymmetries in water vapor and inferences about transport in the lower stratosphere, *J. Geophys. Res.*, *102*, 13,213–13,234.

Rothman, L. S., et al. (1998), The HITRAN molecular spectroscopic database and HAWKS (HITRAN atmospheric workstation): 1996 edition, *J. Quant. Spectrosc. Radiat. Transfer*, *60*(5), 665–710.

Russell III, J. M., et al. (1993), The halogen occultation experiment, *J. Geophys. Res.*, *98*, 10,777–10,797.

Santee, M. L., G. L. Manney, L. Froidevaux, W. G. Read, and J. W. Waters (1999), Six years of UARS Micowave Limb Sounder HNO_3 observations: Seasonal, interhemispheric, and interannual variations in the lower stratosphere, *J. Geophys. Res.*, *104*(D7), 8225–8246.

Santee, M. L., G. L. Manney, N. J. Livesey, and W. G. Read (2004), Three-dimensional structure and evolution of stratospheric HNO_3 based on UARS Microwave Limb Sounder measurements, *J. Geophys. Res.*, *109*, D15306, doi:10.1029/2004JD004578.

Smith, S. E., et al. (1996), Dinitrogen pentoxide measurements from the improved stratospheric and mesospheric sounder: Validation of preliminary results, *J. Geophys. Res.*, *101*(D6), 9897–9906.

Steck, T. (2002), Methods for determining regularization for atmospheric retrieval problems, *Appl. Opt.*, *41*(9), 1788–1797.

Stiller, G. P. (Ed.) (2000), *The Karlsruhe Optimized and Precise Radiative Transfer Algorithm (KOPRA), Wissenschaftliche Berichte*, vol. FZKA 6487, Forschungszentrum Karlsruhe.

Tao, X., and A. Tuck (1994), On the distribution of cold air near the vortex edge in the lower stratosphere, *J. Geophys. Res.*, *99*, 3431–3450.

Toon, G. C. (1987), Detection of stratospheric nitrogen species, *Nature*, *330*, 427.

Toon, G. C., C. B. Farmer, and R. H. Norton (1986), Detection of stratospheric N_2O_5 by infrared remote sounding, *Nature*, *319*, 570–571.

Toon, G. C., C. B. Farmer, L. L. Lowes, P. W. Schaper, J.-F. Blavier, and R. H. Norton (1989), Infrared aircraft measurements of stratospheric composition over Antarctica during September 1987, *J. Geophys. Res.*, *94*, 16,571–16,596.

Varotsos, C. (2004), The extraordinary events of major, sudden stratospheric warming, the diminutive Antarctic ozone hole, and its split in 2002, *Environ. Sci. and Pollut. Res.*, doi: 10.1065/espr2004.05.205.

Visconti, G. (2001), *Fundamentals of Physics and Chemistry of the Atmosphere*, Springer-Verlag.

von Clarmann, T., and G. Echle (1998), Selection of optimized microwindows for atmospheric spectroscopy, *Appl. Opt.*, *37*(33), 7661–7669.

von Clarmann, T., et al. (2003a), A blind test retrieval experiment for infrared limb emission spectrometry, *J. Geophys. Res.*, *108*(D23), 4746, doi:10.1029/2003JD003835.

von Clarmann, T., et al. (2003b), Retrieval of temperature and tangent altitude pointing from limb emission spectra recorded from space by the Michelson Interferometer for Passive Atmospheric Sounding (MIPAS), *J. Geophys. Res.*, *108*(D23), 4736, doi:10.1029/2003JD003602.

Wetzel, G., H. Fischer, and H. Oelhaf (1995), Remote sensing of trace gases in the midinfrared spectral region from a nadir view, *Appl. Oppt.*, *34*(3), 467–479.

Wetzel, G., et al. (2002), NO_y partitioning and budget and its correlation with N_2O in the Arctic vortex and in summer midlatitudes in 1997, *J. Geophys. Res.*, *107*(D16), 4280, doi: 10.1029/2001JD000916.

List of Figures

1.1 A simple scheme of the most gas phase reactions for the stratospheric chemistry. The ellipses include the nitrogen, chlorine and hydrogen families (taken from *Visconti* [2001]). 3

2.1 Limb viewing geometry. 9

3.1 Retrieved profiles and their linear estimates for H_2O according to Hessian (top left) and Gauss-Newton methods (bottom left). The top right and bottom right panels represent the difference between the retrieval and linear estimate for the respective methods. 22

3.2 The bottom left and right panels represent the random errors estimated using the two algorithms and their difference respectively. 22

3.3 Left: Eigenvalue of the inverse error matrix for H_2O. Right: The contributions of each eigenvector direction (along the horizontal axis) for a unit change in χ^2 along each state parameter $\mathbf{z_i}$ (at altitudes i along the vertical axis) for H_2O retrievals. . 23

3.4 Left: The distribution of $\Delta\chi^2$ as a function of a departure of profile from minimum in $\mathbf{z}$-space for H_2O for altitudes of 6 and 11 kms. Right: The departure of χ^2 from ideal quadratic form indicated by the same symbols in the left panel for Hessian and Gauss-Newton. 24

3.5 Left: The distribution of $\Delta\chi^2$ as a function of a departure of profile from minimum in natural coordinate for H_2O for altitudes of 27.5 and 52.5 kms. Right: The departure of χ^2 from ideal quadratic form indicated by the same symbols in the left panel for Hessian and Gauss-Newton. 25

3.6 The vertical resolutions of H_2O retrievals form the two methods as noted in the legend and their differences. 25

3.7 As in Fig. 3.1 but for $ClONO_2$ profiles and their departure from linear estimates. . 26

3.8 As in Fig. 3.2 but for $ClONO_2$ random noise error and difference in these values from the two methods. 27

3.9 As in Fig. 3.3 but for $ClONO_2$ retrievals based on the two methods. 27

3.10 Left: The distribution of $\Delta\chi^2$ as a function of a departure of profile from minimum in **z**-space for $ClONO_2$ for altitudes of 10 and 25 kms. Right: The departure of χ^2 from ideal quadratic form indicated by the same symbols in the left panel for Hessian and Gauss-Newton. 28

3.11 Left: The distribution of $\Delta\chi^2$ as a function of a departure of profile from minimum in **z**-space for $ClONO_2$ for altitudes of 37.5 and 50 kms. Right: The departure of χ^2 from ideal quadratic form indicated by the same symbols in the left panel for Hessian and Gauss-Newton. 29

3.12 The vertical resolutions of $ClONO_2$ retrievals form the two methods as noted in the legend and their differences. 30

4.1 The broadband background continuum simulated for two sulphate aerosol species containing H_2SO_4 of sizes 0.04 μm and 0.68 μm for midlatitude and equatorial model atmospheres. The difference of the two microwindows in ν_{12} band of N_2O_5 from the external microwindows is hardly seen in the left panel. The right panel shows the differences which is slightly visible below 5 km and in the altitude ranges centered on 20 km and 25 km for midlatitude and equatorial atmospheres respectively. 34

4.2 Daytime N_2O_5 profiles (solid lines) as retrieved from measurements taken when the satellite is in orbit 02994 for geolocation inside (left) and outside (right) of the southern polar vortex on September 26, 2002. The dotted line is the a priori. The error bars represent noise induced errors. 35

4.3 The relative random error and vertical resolution (top) and the averaging kernel(A) (bottom) corresponding to the profile outside the vortex 36

4.4 The measured and calculated spectra in all three spectral intervals for tangent altitude of 29 km. The right column represents the residual spectra (fitted spectra subtracted from measured spectra). The spectra correspond to the retrieved profile shown in Fig. 4.2 (right). 38

5.1 MIPAS/ENVISAT N_2O_5 (right panel) and HNO_3 (left panel) profiles in September compared with MIPAS-B2 profiles (red for Northern flight and orange for the southern flight). MIPAS/ENVISAT profiles as well as satellite tracks are indicated by green and blue colors. 41

5.2 MIPAS/ENVISAT N_2O_5 (right panel) and HNO_3 (left panel) profiles in March compared with MIPAS-B2 profiles. 42

5.3 MIPAS/ENVISAT NO_y (right panel) and HNO_3 (left panel) profiles in December compared with MkIV profiles (red). 42

5.4 MIPAS/ENVISAT NO_y (right panel) and HNO_3 (left panel) profiles in April compared with MkIV profiles (red). 43

5.5 Example of MIPAS/ENVISAT profile comparison with SIOUX profiles. Left: The dive part of SIOUX NO_y compared with coincident MIPAS/ENVISAT measurement from scan 04849_20020202T201814Z. Right: The same scan compared to the ascent part of SIOUX measurements. 43

5.6 MIPAS/ENVISAT-SIOUX average fractional difference profile comparison. The dive part (left) and ascent part (right) along with the number of data points used for the calculation of average and standard deviation of the average fractional difference. 44

5.7 MIPAS/ENVISAT averaging kernels (left: information comes from measurements down to 7 km) and (right: information comes from measurements only above 15 km). 45

5.8 HNO_3 on 585 K level to facilitate comparison with MLS HNO_3 Climatology. The zonal mean is calculated from data binned in to 4^o equivalent latitude. 46

6.1 N_2O as a function of equivalent latitudes. The vortex edge is overlaid by white solid line extending along the altitude axis and a wide vortex edge region is assumed to lie within 5 degree equivalent latitude width from the edge in either sides. White lines indicate potential temperature levels of 400 (solid), 475, 550, 625, 850 K (dash-dot-dot). 49

6.2 NO_y as a function of equivalent latitudes. The vortex edge is overlaid by white solid line extending along the altitude axis and a wide vortex edge region is assumed to lie within 5 degree equivalent latitude width from the edge in either sides. White lines indicate potential temperature levels of 400 (solid), 475, 550, 625, 850 K (dash-dot-dot). 50

6.3 The evolution vortex position and size as seen from NO_y VMR, geographic latitudes and equivalent latitudes at a potential temperature of 400 K (top), 475 K (middle) and 550 K (bottom) for the periods indicated at the top of each panel. The dotted horizontal lines represent the vortex edge barrier on the day and night sides of the vortex. 53

6.4 the same as Fig. 6.3 at a potential temperature of 625 and 850 K. 54

6.5 VMR along the orbit track on September 21, 22, 26 and October 13. The first row represents conditions during the presplit vortex while the second row denotes that of a split and postsplit of the vortex. Left of 90^o is the daytime (descending) and right of 90^o is the nighttime (ascending) part of the orbit. White lines indicate potential temperature levels of 625 (solid), 700, 850, 1000, 1200 K (dash-dot-dot). 55

6.6 N_2O_5 distributions on 850 K level of potential temperature. The measurements during 20-22 September, 2002 represent presplit of the vortex while that during 26 September and 13 October, 2002 represent split and postsplit periods in this order. The underlying contour lines show potential vorticity. Symbols enclosed by boxes mark the beginning of each orbit on the dayside. 56

6.7 The solar zenith angle dependence of N_2O_5 VMR as a function of equivalent latitudes at a potential temperature of 850 K (left) and 1000 K (right). The dotted vertical and horizontal lines represent the vortex edge and SZA=90^o respectively. The vortex edge is determined according to *Nash et al.* [1996] using METO analysis data and averaged over the number of days in the respective periods. 57

6.8 The solar zenith angle dependence of N_2O_5 VMR for inside vortex (left panel) and equivalent latitude bin of 35-40^o S (middle panel) at 850 K theta level extracted from the data shown in Figure 7. The right panel shows the observed VMR as a function of time since sunrise (SR) and sunset (SS) for data shown in the middle panel. The black, red, blue and green triangles represent the 20-21, 22-24, 25-27 September and 11-13 October periods respectively. 58

6.9 Vertical profiles of N_2O_5 VMR averaged over 4 degree equivalent latitude for early presplit, presplit, split and postsplit of the vortex. The vortex edge is overlaid by white solid line extending along the altitude axis and a wide vortex edge region is assumed to lie within 5 degree equivalent latitude width from the edge in either sides. White lines indicate potential temperature levels of 400 (solid), 475, 550, 625, 850 K (dash-dot-dot). 59

6.10 MIPAS temperature distribution at 850 K theta level for 20, 22, and 26 September measurements. The underlying contour lines show potential vorticity. 61

6.11 The same as Fig. 6.2 but showing daytime and nighttime NO_y partitioning in the stratosphere for individual components. 62

6.12 the same as Fig. 6.11 but showing daytime and nighttime NO_y fraction. 63

6.13 Vortex NO_y partitioning at potential temperature of 625 and 850 K. The ratio of individual NO_y components to total NO_y is ploted on the left side to separate dynamical from chemical effects. Green, black, blue and red lines represent HNO_3, NO_x, $ClONO_2$ and $2N_2O_5$ respectively. 64

6.14 MIPAS (a). [NO_y]:[N_2O], (b). [CH_4]:[N_2O], (c). [CFC-11]:[N_2O] and (d). NO_y versus artificial tracer relationships. ATMOS ex-vortex mid-spring and Fall-95 Antarctic vortex correlation curves are overlaid in panel a. 67

6.15 MIPAS (a). [CH_4]:[N_2O], (b). [NO_y]:[N_2O], and (c). NO_y versus artificial tracer relationships built from July data for the early presplit period. Vortex scatter points above the altitude of peak NO_y VMR are shown by open circles and those below these levels are shown by filled circles. Note that most of the data shown by open circles are contained within the bounds of mixing scatter. 68

6.16 The same as Fig. 6.15, but for the presplit period. 69

6.17 The same as Fig. 6.15, but for the split period. 70

6.18 The same as Fig. 6.15, but for the postsplit period. 71

6.19 Vertical distribution of the NO_y deficit and contribution of the denitrification as estimated by the two different methods (indicated by the legend in panel (a)). The error bar is the standard deviation of the mean while the scatter in the data is much higher. The theta range covers the range of N_2O between 6-300 ppbv in which the artificial reference tracer is constructed. Data outside this range is not considered since the reference tracer method can not capture mixing outside the range of data used for its definition. 72

List of Tables

4.1 The estimated total error, random error due to spectral noise, the total systematic error, systematic error due to interfering gases, temperature, spectroscopic data (due to uncertainity in band intensity), pointing information, residual spectral shift, gain caliberation, instrumental line shape and non-LTE for typical profiles of daytime midlatitude (top) and nighttime polar vortex (bottom) for selected altitudes for measurements on September 26, 2002. The errors are given in absolute unit [pptv] and relative unit [%] (number in bracket). The species that are assumed to interfere in retrieval spectral regions of N_2O_5 are CO_2, O_3, SO_2, NO_2, HNO_3, HOCl, H_2O_2, C_2H_2, COF_2, F14, and $ClONO_2$. 37

6.1 Occapation matrix used for joint retrieval of HNO_3 and O_3. The columns represent from left to right: the microwindow number, the microwindow and the height at which it is used (label "T" indicates the microwindow is used at the given height begining with 5 km (left corner of the column) and 56 km (right corner of the column). 48

6.2 The estimated total error, random error due to spectral noise, the total systematic error, systematic error due to interfering gases, temperature, spectroscopic data (due to uncertainity in band intensity and half line width), line of sight (LOS), residual spectral shift, gain caliberation, instrumental line shape and forward model for typical profiles of nighttime midlatitude (top) and nighttime polar vortex (bottom) for selected altitudes for measurements on September 26, 2002. The errors are given in absolute unit [pptv] and relative unit [%] (number in bracket). The species that are assumed to interfere in the microwindows selected for HNO_3 retrieval are H_2O, CO_2, O_3, NO_2, N_2O, CH_4, C_2H_6, CFC-11, CFC-12, ClO, OCS and NH_3. 51

6.3 The same as Table 6.2, but for NO_y. 52